Dissertation of China Institute of Atomic Energy

Improvements of the HERMES Transverse Polarized Hydrogen Target and Calculations of the Sextupole Magnet

Author: WANG Siguang

Supervisors: Prof. ZHOU Shuhua

Prof. YE Yunxiu

Dr. Paolo LENISA

Printed Date: August of 2004

摘要

HERMES(**HER**A **ME**asurement of **S**pin)实验装置坐落在DESY的HERA储存环东部直线部分. 利用27.5GeV的极化正电子/电子轰击内置极化气体靶, 通过深度非弹研究核子的自旋结构, 探讨核子自旋的来源, 探索"核子自旋危机"的物理机制. 这类实验的关键技术之一就是要有一个高性能的极化靶. HERMES靶作为内置气体靶, 具有无本底杂质、高极化度和极化方向可迅速翻转（毫秒级）等特点。

本人在HERMES工作期间，负责极化氢靶的维护和运行。提出并完成了对极化靶的改进工作, 最大限度地减小了束流引发的共振退极(共振时极化度减小2% $\sim$ 3%), 提高了HERMES实验极化数据的质量。

HERMES当前运行模式为纵向极化电子束打横向极化的气体氢靶。该极化气体靶通过ABS(**A**tomic **B**eam **S**ource) 持续向靶室注入处于特定自旋态的氢原子获得。首先利用H_2O制造氢气，利用高频电磁波驱动，将氢气分离成氢原子气体。通过温度100K的喷嘴及准直口，注入装有六极磁体的真空腔。利用处于不同自旋态的原子在有梯度的磁场中，通过有效磁矩与外磁场之间的作用力的不同，将核外电子自旋为正的原子会聚，而核外电子自旋为负的原子被发散开。发散的原子将被ABS的真空系统抽出。会聚的束流中的原子在经过高频转换器HFT（**H**igh **F**requency **T**ransition）时，处于特定超精细态的原子就会发生共振，使得自旋态改变，得到核自旋Pz为正的极化靶($|1\rangle$ 和$|4\rangle$态)和Pz为负($|2\rangle$和$|3\rangle$态)的极化靶。

为了保持高极化度，靶室置于与束流垂直、强度约为279mT（$1mT = 10Gs$）的磁场中。同时在与ABS相对的、靶的另一侧，利用TGA(**T**arget **G**as **A**nalyzer)通过取样管道测量采样气体中处于单质原子态的气体所占比例（部分处于分子态）。利用BRP(**B**reit-**R**abi **P**olarimeter)测量采样气体中处于$|1\rangle$、$|2\rangle$、$|3\rangle$和$|4\rangle$各态的原子相对比例，从而给出极化度。ABS、靶室、TGA和BRP之间的相对位置如图1所示。

本论文主要讲述以下几项工作：

1 <u>提出2种方法通过实验直接测量修正函数$G(T)$。</u>

利用TGA测量HERMES极化原子气体靶中原子所占的比例时，有一个非常重要的参数κ必须预先提供。该参量用来描述TGA对于原子和分子的相对灵敏程度。κ的测量原理为:保持在单位时间内总的原子数目(处于原子单态与分子态的总和)注入量不变的情况下，通过改变靶室的温度影响两个原子在靶室内壁上复合成一个分子的几率来改变靶室中原子与分子数目的比例，根据TGA对于原子信号Sa和分子信号Sm之间的变化斜率计算出κ值。由于温度的改变会影响到与靶室相连的各管道的导气率，在计算κ时，需引入修正函数$G(T)$。至2003年，$G(T)$只有理论值。本人分别于2003年4月及9月提出两种测量$G(T)$的实验方法，其测量结果已经用

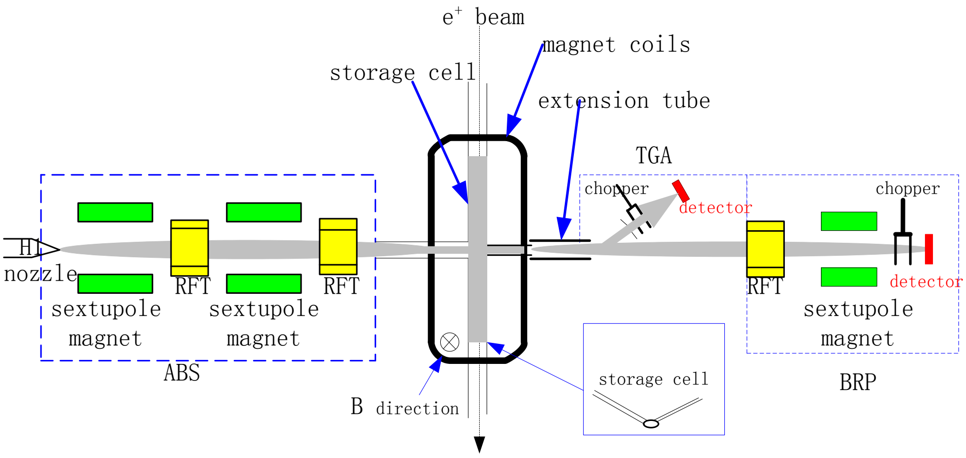

Figure 1: ABS、靶室、TGA和BRP之间的相对位置示意图

于κ刻度数据的处理。这两种方法分别为：1) 利用UGFS(**U**npolarized **G**as **F**eed **S**ystem)向靶室注入稳定H_2气流，用与刻度同样的方法改变靶室的温度，同时利用TGA测量Sm。由于H_2分子不存在类似于H单质原子复合的问题，所以可得到Sm随温度的相对变化，即$G(T)^{UGFS}$修正函数。2) 对于新安装的靶，如果靶室内壁Drifilm镀膜的质量比较好，利用ABS进行κ刻度时，即使温度降得很低，原子复合成分子的几率变化也不大。即不同温度时，靶室中原子占主要成份，分子成份很小，无法进行κ刻度。利用初始值，可以给出总的原子数随温度的相对变化，即$G(T)^{ABS}$修正函数。理论值$G(T)^{THEO}$ 及实验值$G(T)^{UGFS}$和$G(T)^{ABS}$结果见图2。参考1997年10月因HERA束流脱靶而意外获得的不需温度修正的$\kappa = 0.572 \pm 0.003$及利用

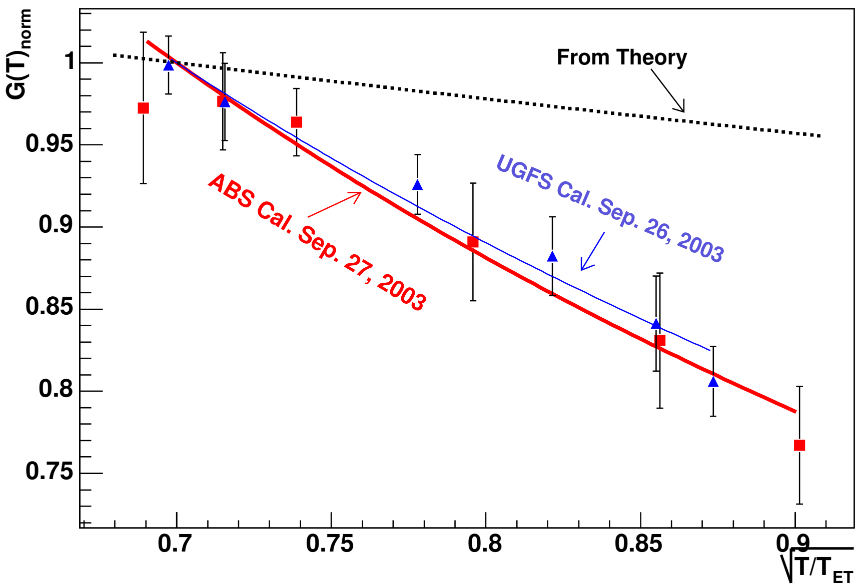

Figure 2: 理论值$G(T)^{THEO}$ 及实验值$G(T)^{UGFS}$和$G(T)^{ABS}$.

不同$G(T)$修正对2004年4月4日κ刻度数据处理结果：

- 用$G(T)^{UGFS}$ 修正S_a和S_m信号所得κ值:(测量日期2004年4月10日)$\kappa = 0.73 \pm 0.15$
- 用$G(T)^{ABS}$(测量时间为2003年9月27日. 但在2003年10月初，TGA被调节)修正S_a和S_m信号后所得κ值: $\kappa = 0.82 \pm 0.15$
- 理论$G(T)^{THEO}$修正S_a和S_m信号后所得κ值:($\kappa = 1.1 \times 10^8 \pm 4.4 \times 10^8$)
- 不修正(G(T)=1)所得κ值:$\kappa = 4 \times 10^8 \pm 9 \times 10^8$.

鉴于1997年10月所得的κ比较可靠，对于2004年4月4日κ刻度，利用$G(T)^{UGFS}$和$G(T)^{ABS}$所给出的结果优于$G(T)^{THEO}$或不修正给出的结果．$G(T)^{UGFS}$和$G(T)^{ABS}$所给出的结果与1997年10月结果之间的偏离源于多次安装后几何位置不完全一致．经$G(T)^{UGFS}$修正所给κ值与$G(T)^{ABS}$修正所给值之间的差别在于：测量$G(T)^{ABS}$后，TGA光学系统的几何有所改变；而测量$G(T)^{UGFS}$时的几何与2004年4月4日κ刻度时几何条件一致，故本次测量$G(T)^{UGFS}$修正所给出的κ结果最为可靠．由图2所给出的曲线可知，当新靶安装后，如果几何TGA保持不变，利用ABS及UGFS测出修正函数$G(T)$的方法所给出的结果是一致的。

2 发现并解释一磁感应强度随磁体铁心温度的升高而降低的现象。

在测量HERMES的极化靶电磁铁的磁场分布时，发现磁感应强度B随测量时间的增加而降低，同时发现磁体的铁磁材料及支撑框架的温度逐渐升高。该现象可解释为：随温度的升高，铁磁物质中磁畴的排列受热运动影响所至。一组监测数据显示，电磁体线圈中加载545A电流后，固定测量点处（约339mT）磁感应强度在8个小时内下降0.45mT, 见图3。2002年极化度数据表明,磁感应强度不稳而引发的共振退极的确引发了靶极化度的降低.

3 建立全自动磁场稳定系统获得高稳定磁场

对于当前HERMES极化靶，由HERA储存环中e^+束流所激发的脉冲电磁场可以引发氢极化气体靶的共振退极，且在工作点附近，满足共振条件的相邻两共振点所对应的外磁场之间相差仅0.37mT。对于在靶室处沿束流方向的外磁场的平整度约0.05mT的外磁场，其磁感应强度随磁体铁心温度的升高而降低的现象必然能使共振条件得到满足。为抑制和消除共振的发生，建立了一套负反馈系统，通过实时监测磁场，调节附加线圈中的电流，可将磁场相对稳定在所需要值的±0.004mT内，见图4。该系统建立后有效地抑制了靶极化度的共振退极(当束流强度为41mA时，测量显示无磁场稳定系统发生共振时极化度减小幅度大于3%)。

4 首次通过实验给出由HERA束流引发的HERMES横向极化靶的σ共振图

在外磁场强度满足共振条件时，HERA束流所激发的磁场可以引发HERMES极化气体靶共振退极。利用全自动磁场稳定系统获得高稳定磁场进行精细扫描，获得了第一个关于该极化靶的σ共振图,如图5。通过该图，可以得到尽可能避免共振退极发生的最优的外磁场值，以保持该极化气体靶处于最大的极化。

5 利用MAFIA计算超导六极磁体的磁场分布

通过精细建模，利用MAFIA计算意大利Ferrara大学HERMES组测试的超导六极磁体的磁场分布。该计算结果与测量值在误差范围内符合。

6 寻求安装在靶室两侧的线圈中需要加载的最优化的电流值

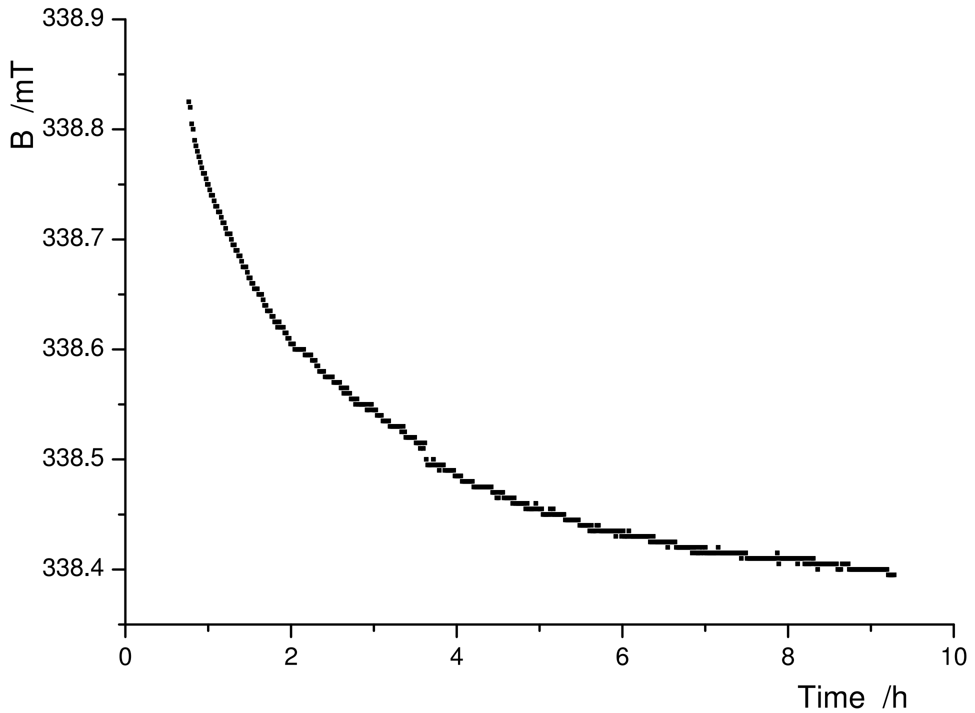

Figure 3: 磁场强度随时间变化曲线

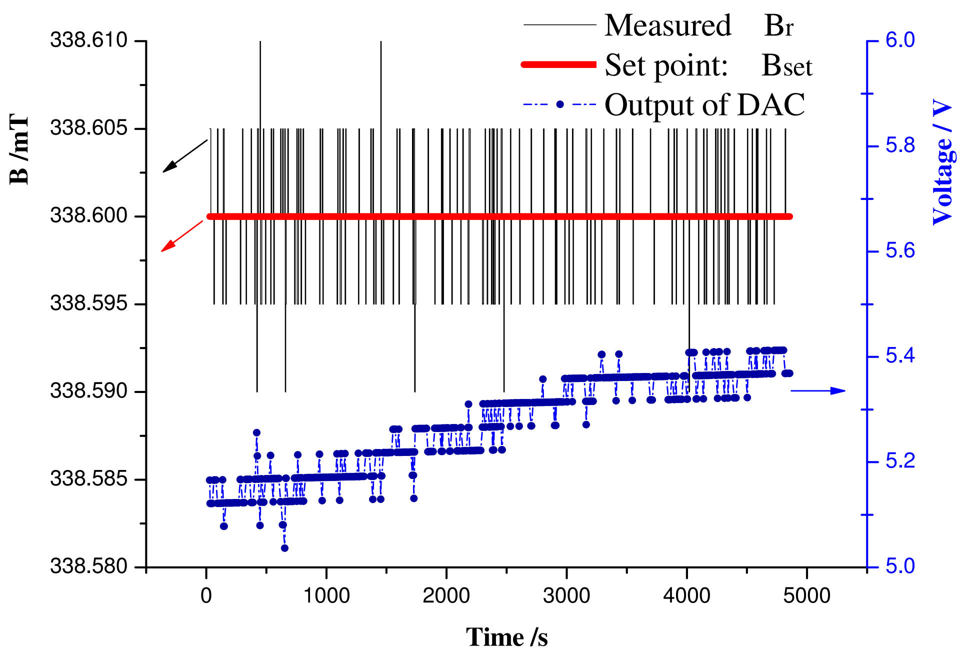

Figure 4: 全自动稳定系统将磁场稳定在所需值的0.004mT内

为了得到更为平整的磁场，Ferrara组在靶室两侧安装了一对辅助线圈。为了给出工作电流，利用MAFIA计算出加载不同电流后的磁场分布，并且参考所测量的外磁场的磁场分布，确定出最优化电流值。

7 将靶组所有的刻度分析程序从PAW移植到ROOT平台

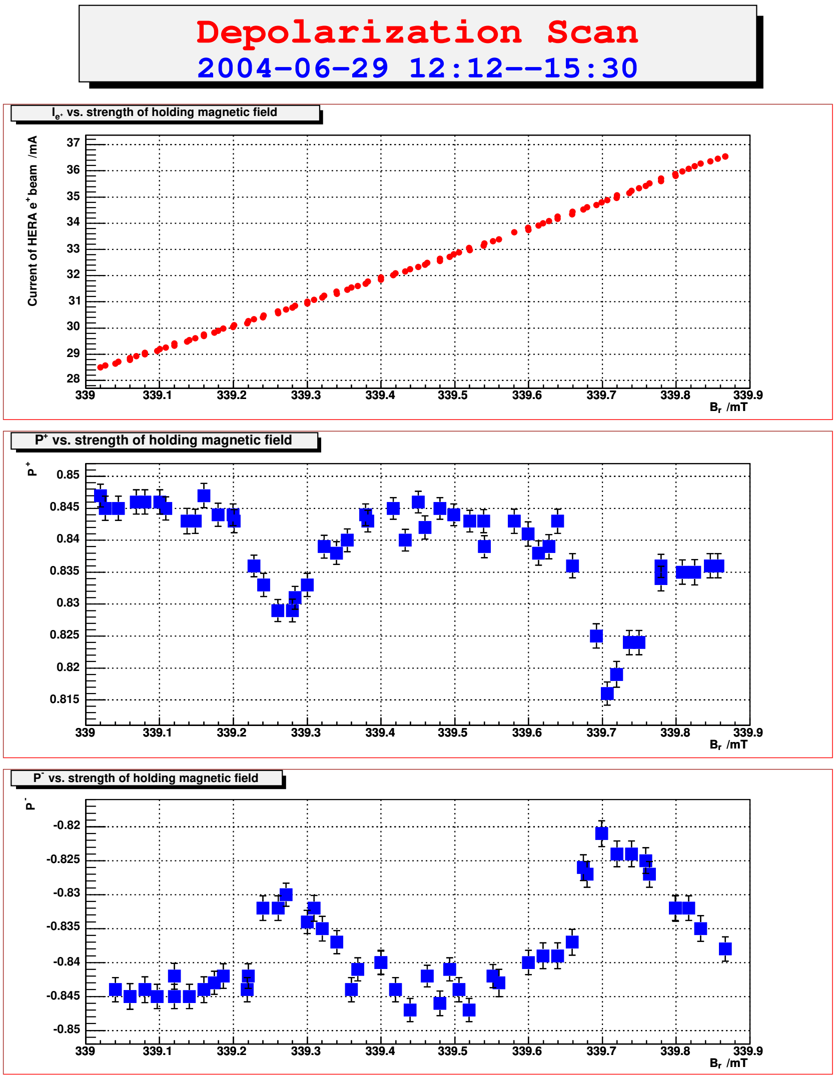

Figure 5: 进行磁场扫描所得σ共振峰

为了便于维护和操作，将靶组的所有的刻度程序从原来的PAW程序全部改为ROOT程序。

8 利用ANASYS研究气体喷出喷嘴后的物理特性

模拟气体喷出不同形状的喷嘴后其速度(如图6)，温度和密度的分布。为以后更优化的ABS的模拟设计工作做准备。

关键词：极化气体靶 极化度 六极磁体 磁感应强度

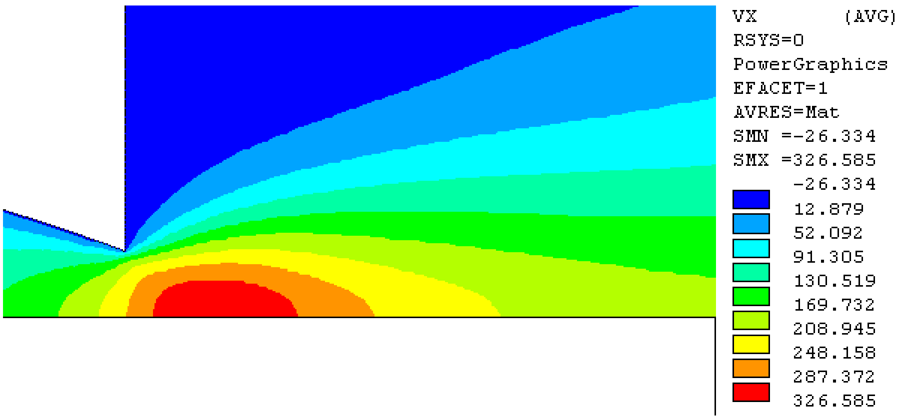

Figure 6: 空气喷出形如HERMES靶中喷嘴后的轴向速度(速度的水平分量)分布

Abstract

The HERMES (**HER**A **ME**asurement of **S**pin) experiment is located in the eastern straight section of the HERA storage ring at DESY, Hamburg-Germany. It is designed to study the spin structure of the nucleon by deep inelastic scattering of the polarized electrons/positrons provided by the HERA storage ring at 27.5 GeV impinging on the nucleons of an internal polarized gas target.

During the period of my presence in Hamburg, I've been involved in the group responsible for the maintenance and operation of the polarized gas target.

In this thesis, after an introduction to the physical motivations and to the hardware setup, my contributions will be presented. One of them is about two new proposed methods to measure the temperature correction function $G(T)$. An important parameter, denoted as κ, for the determination of the atomic fraction, α, (i.e. the fraction of atoms present in the target cell), is the relative detection efficiency for atoms and molecules in the quadrupole mass spectrometer of the Target Gas Analyzer (TGA). The method adopted for the determination of the κ parameter is based on the variation of the relative amount of atoms and molecules in the cell, by keeping the total flux of the source constant. This can be accomplished by making use of the temperature dependence of the surface recombination process in the target cell. As the variation of the temperature causes also a variation of conductances of the cell, the sample tube and the extension tube, the temperature dependence of these conductances has to be taken into account by introducing a temperature correction function $G(T)$. The proposed methods for the determination of the correction function $G(T)$ have been tested. Another one is about finding and explaining the dependence of the magnetic holding field of the target with the temperature of the magnet yoke. During the mapping of the transverse magnetic field of the HERMES target, a gradual decrease of the measured field has been observed while the current in the coil is constant. Subsequently, the temperature of the yoke on the magnet has been then monitored at the same time, and shows a similar behavior (but increase) as that of the measured field. This demonstrates a clear correlation between the two observables. My explanation for such phenomena is that the arrangements of magnetic domains inside the ferromagnet of the yoke and pole are disturbed more seriously while the temperature is higher. The magnetic field has been monitored to decrease by $0.45\,mT$ within 8 hours at the measuring point (339 mT) of the target. This could not be tolerated for the optimal performance of the target and has to be corrected. So a feedback control system to stabilize the magnetic holding field of the target by means of a couple of additional coils is established. The feedback system has been implemented during the 2003 shutdown together with a couple of coils to automatically measure the field and drive the current in the coils to keep it stable. The magnetic field of the target has been stabilized in this way within $\pm 0.004\,mT$, which allows us to operate the target in the optimal condition. The compensation of the drift of the holding field allowed to avoid the particular conditions in which some resonances induced by the electron beam becomes active in the target, thus inhibits possible depolarization, whose amplitude can be greater than 3% at resonance region according to experimental data. With this system, a plot of firstly measured beam induced σ-transitions in a transversely polarized target for the optimized value of the holding magnetic field is obtained, taking the advantage of the high stability of the holding field reached with the control system and the possibility of performing very fine field scan. Some calculation results of the magnetic field distribution of a super-conducting sextupole magnet trained by the Ferrara-HERMES group with MAFIA are also presented. The result agrees well with a measurement of the magnetic field performed at CERN. The results can be used as an input for the track simulation of atoms passing through the sextupole system. For the best performance of the HERMES target, optimization studies of the current in cell-coils, which are to optimize the field uniformity in the storage cell volume have also been made. The fields produced by the coils with different current intensities have been simulated by MAFIA, when operated together with the target holding field. In order to improve the efficiency in the target maintenances, all the codes related to the different calibrations of the target have been transformed from PAW to ROOT platform. For a more optimized ABS (Atomic Beam Source), distributions of velocity, temperature and density of the gas jetted out from nozzles in different shapes have been simulated with ANSYS.

Keywords: Polarized Gas Target   Polarization Degree   Sextupole Magnet   Flux Density of Magnetic Field

Contents

Chapter 1

Introduction

This chapter will introduce the physics motivation of HERMES (**HER**A **ME**asurement of **S**pin) and the main instruments on its spectrometer.

1.1 What is HERMES

HERMES, located in the eastern straight section of the HERA (**H**adron **E**lektron **R**ing **A**nlage) storage ring, is one of the four experiments at the DESY (**D**eutsches **E**lektronen-**SY**nchrotron) laboratory in Hamburg, Germany. See figure 1.1.

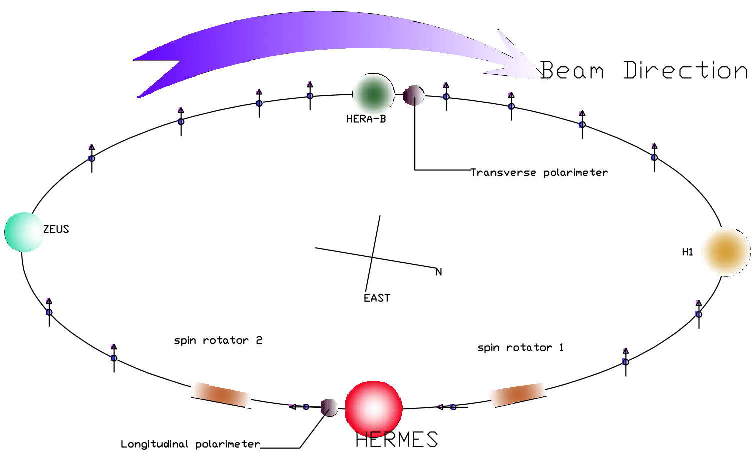

Figure 1.1: Location of HERMES in the storage ring of DESY. The two spin rotators located upstream and down stream of the HERMES experiment with two beam polarimeters

The first data-taking run started in 1995, and ended in September of 2000. HERMES run 2 started in 2001 and will last up to the end of 2006[HmsWb].

The HERMES only uses the polarized lepton beam while ZEUS and H1, are colliding-beam experiments and HERA-B uses only the proton beam. The high current longitudinally polarized positron/electron beam of HERA with beam energy 27.5 GeV bombards polarized or unpolarized gas targets internal to the storage ring in the HERMES experiment. At such beam energy, many processes, called polarized **D**eep-**I**nelastic **S**cattering (DIS), will happen. And the polarized DIS can be described with following process:

$$\overrightarrow{e} + \overrightarrow{N} = e^{'} + X \tag{1.1}$$

where longitudinally polarized electrons $\overrightarrow{e}$ are scattered off a longitudinally/transversely polarized nucleon $\overrightarrow{N}$(proton, deuterium), which breaks into a hadronic final state X with an invariant mass W, which is much larger than the nucleon mass M.

The longitudinally polarized beam is produced based on he Sokolov-Ternov mechanism [Sok64]. The HERA beam is characterized by a self polarization, perpendicular to its momentum, which is turned to longitudinal at the HERMES interaction point by the employment of two spin rotators, shown in figure 1.1. The first spin rotator rotates the spins into the beam direction and the second one turns them back to the vertical direction before the beam enters the arc.

1.2 Physics Motivation of HERMES

While the proton and the neutron are made up of quarks and gluons, the spin of the proton or the neutron is difficult to reconcile with the spins of quark and gluon components. For more than a decade, physicists have struggled to solve this puzzle.

In 1988, CERN's European Muon Collaboration (EMC) experiment stunned the world of physics with the announcement that some of the nucleon's spin was missing. More than a decade later, physicists are still trying to account for the missing spin and the spotlight has moved to the HERMES experiment at Hamburg's DESY laboratory.

The closer you look, the more you see. That may sound like a common sense maxim, but when it comes to nucleons it takes on an interesting twist. In a simple quark-parton model, a nucleon is made up of three quarks and it is the spins of these quarks that are supposed to give the nucleon its spin. That simple notion was disproved when the first experiments with polarized deep-inelastic lepton scattering at SLAC[Alg76, Alg78] and then CERN[Ash88, Ash89] which gave rise to what was quickly dubbed the nucleon spin crisis, announcing that quarks could account for only around 20% of a nucleon's spin at most[Cer41].

The EMC result led to several experiments taking a much closer look at what goes on inside nucleons. The three quarks that give a nucleon its identity-the valence quarks-are just the beginning of the story. They swim in a "sea" of virtual quarks and antiquarks that are constantly popping in and out of the vacuum. Moreover, gluons flit about inside nucleons, holding the quarks together. All of these can contribute to a nucleon's spin, and their constant movement generates an intrinsic angular momentum of the nucleon as a whole.

A succession of experiments to pin down the effect ensued at CERN (the NMC and SMC collaborations using muon beams) and at SLAC (with electron beams), and by the late 1990s the spin crisis had transformed into a puzzle: that of finding out how the nucleon's spin was distributed among its various contributing factors. The CERN and SLAC experiments had confirmed, with greatly improved precision, the original EMC finding that quarks alone could not be responsible for the nucleon's spin. The next task was to measure the contributions of the individual quark flavours and of gluons. The baton passed to HERMES.

In the history, deep inelastic electron scattering gave the first indication of point-like constituents in the nucleon and this played a crucial role in the development of QCD. A lot of works have been done with electron, muon, and neutrino interactions for over three decades to explore structure functions in DIS, which provide information about the momentum distributions of quarks and gluons in the nucleon.

In addition to confirming the essential description of DIS in terms of the fundamental theory QCD, those works have led to a series of surprising discoveries in their revelation of the properties of the parton distributions of the nucleon. Before QCD was introduced, this pattern actually began when the failure of the momentum sum rule indicated the existence of a substantial uncharged component to the parton distributions: the gluons.

Another early success is the verification of the spin-$\frac{1}{2}$ nature of the quarks. Since the DIS has yielded such unexpected results: (a) The effect from nuclear binding on structure functions, (b) the failure of the Gottfried sum rule, and (c) the failure of the Ellis-Jaffe sum rule for the spin-dependent structure function g_1 of the proton. Because those extremely important results were all obtained by performing more precise and detailed measurements of DIS, it is very clear that precise deep inelastic scattering measurements have led to both significant tests of fundamental theory and surprising discoveries about the structure of the nucleon.

HERMES is a powerful tool to study spin-dependent effects in electron scattering from the nucleon and few-nucleon systems. It had provided precise experimental data to test QCD and played one of the most important roles on the understanding of nucleon structure. The work deployed in HERMES is the following[Tec93]:

1.2.1 Measurements of g_1 and Sum Rules

The internal spin structure of a nucleon can be studied in DIS of longitudinally polarized charged leptons from a polarized nucleon target through the measurement of two leading twist structure functions: $g_1(x)$ and $g_2(x)$[Kut83]. The x is Bjorken scaling and its definition will be given in the coming paragraph.

The difference between the two cross sections for opposite target polarizations can give the spin dependent part of the deep inelastic cross sections

$$\begin{aligned}\frac{d^3(\sigma(\alpha)-\sigma(\alpha+\pi))}{dxdyd\phi} = \frac{e^4}{4\pi^2Q^2}\Bigg[\cos\alpha\left(\left[1-\frac{y}{2}-\frac{y^2}{4}\gamma^2\right]g_1(x,Q^2)-\frac{y}{2}\gamma^2 g_2(x,Q^2)\right)\\ -\sin\alpha\cos\phi\sqrt{\gamma^2\left(1-y-\frac{y^2}{4}\gamma^2\right)}\left(\frac{y}{2}g_1(x,Q^2)+g_2(x,Q^2)\right)\Bigg]\end{aligned} \tag{1.2}$$

where α is the angle between the beam momentum vector $\overrightarrow{K}$ and the target polarization vector

$\overrightarrow{P}$ as shown in figure 1.2. ϕ as the angle between the polarization plan formed by the $\overrightarrow{K}$ and $\overrightarrow{P}$ and the lepton scattering plane formed by $\overrightarrow{K}$ and $\overrightarrow{K'}$, which is the scattered lepton momentum vector $\overrightarrow{K'}$. In kinematics system, with the energy of E and E' for the incoming and the scattered lepton and the nucleon mass, M, considering the negative square of the invariant mass Q^2 of the virtual photon, the Bjorken scaling variables are defined as $x = Q^2/2M\nu$ and $y = \nu/E$, here the $\nu = E - E'$ and M is the nucleon mass. x can be interpreted as the fraction of the nucleon momentum carried by the struck quark. The γ defined as $\gamma = \sqrt{Q^2}/\nu$.

The two structure functions $g_1(x, Q^2)$ and $g_2(x, Q^2)$ can be extracted from two measurements: one measurement for the longitudinal asymmetry $A_{\|}$ with longitudinal polarized target ($\alpha = 0$) and the other for the transverse asymmetry $A_{\perp}$ with transverse polarized target.

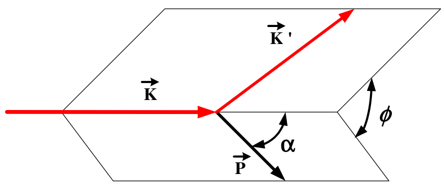

Figure 1.2: Definition of angles α and ϕ in DIS

Theoretically, g_1 can be clearly interpreted in the framework of the parton model as:

$$g_1(x, Q^2) = \frac{1}{2} \sum_f e_f^2 \left[q_f^+(x, Q^2) - q_f^-(x, Q^2) \right] \tag{1.3}$$

where $q_f^+(x, Q^2)$ and $q_f^-(x, Q^2)$ are the polarized quark distributions for each flavor f of quark and anti-quark describing the probabilities to find a quark in a infinite momentum frame with momentum fraction x and a helicity which is the same as (+) or opposite to (-) that of the parent nucleon with positive helicity. e_f is the quark charge in units of $|e|$.

The g_1 sum rules for both the proton and neutron are the particular interesting topics to research:

$$I_1^{p,n} \equiv \int_0^1 g_1^{p,n}(x) dx \tag{1.4}$$

Before the HERMES was proposed to be established, the g_1 sum rule for proton was measured [Ash89] to be:

$$I_1^p = 0.126 \pm 0.010(Sta.) \pm 0.015(Sys.) \tag{1.5}$$

which is more than two standard deviations from theoretical predication[Ell74]: $I_1^p = 0.175 \pm 0.018$ (including the QCD corrections).

The famous Bjorken Sum Rule[Bjo66] connects the integral over x of the difference of $g_1^p(x, Q^2)$ and $g_1^n(x, Q^2)$ with the ratio of the axial vector to vector coupling constants measured in Gamow-Teller nucleon beta decay, $\frac{g_A}{gV}$. In the scaling limit and taking into account of

QCD radiative corrections, the Bjorken Sum Rule can be written as[Kod79, Kod80]:

$$\int_0^1 [g_1^p(x) - g_1^n(x)]dx = \frac{1}{6}\frac{g_A}{g_V}\left(1 - \frac{\alpha_s}{\pi}\right) \tag{1.6}$$

After assuming the validity of the Bjorken Sum Rule in equation (1.6) and the proton sum rule I_1^p measured by EMC/SLAC, the neutron sum rule I_1^n can be obtained through experimental data.

High quality experimental data play a crucial role for determining the $I_1^{p,n}$. Taking the advantage that the HERMES target is a pure gas target without background material and the signs of the polarization can be rapidly inversed, the systematic error of $I_1^{p,n}$ measured by HERMES is smaller than other experiments such as SMC or E143, see figure 1.3.

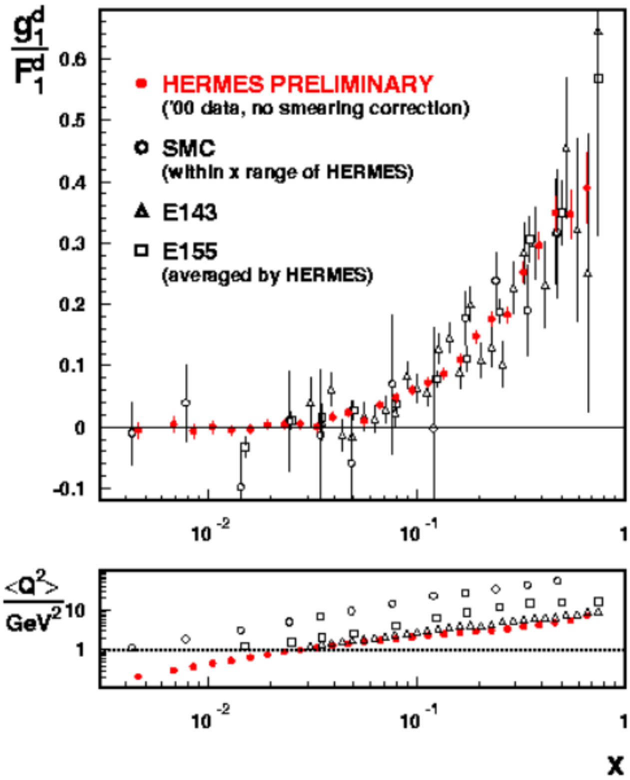

Figure 1.3: Comparing among the $\frac{g_1^d}{F_1^d}$ results measured by HERMES[HER02], SMC[Ade99], E143[Abe98] and E155[Ant99].

1.2.2 Measurement of $g_2^{p,n}$

Much attention has been focused on spin-dependent structure function $g_2(x, Q^2)$ at the beginning of 1990s. The knowledge of g_2^{x,Q^2} is necessary for an unambiguous determination of $g_1(x, Q^2)$ from the cross section described in equation (1.2). And it also can provide a test for the Wandzura-Wilczek relation[Wan77, Shu82]. Another important issue for $g_2(x, Q^2)$ result is to answer the question about the validity of the Burkhardt-Cottingham Sum rule (BCSR)[Bur76]:

$$\int_0^1 g_2(x, Q^2)dx = 0 \tag{1.7}$$

For the measurement of g_2^p, a transversely polarized target in addition to a polarized beam is required. Before HERMES, there is no previous measurements of g_2^p and g_2^n. Since the polarized target is a gas target, the orientation of polarization can be changed by altering the direction of holding magnet field.

1.2.3 New Structure Functions from Tensor Spin Observables

In the case of the deuteron, which is a spin-1 target, There are new spin-dependent structure functions beyond spin-$\frac{1}{2}$ named as $b(x)$[Hoo89, Jaf89a] and $\Delta(x)$[Jaf89b]. $b(x)$ can be measured with unpolarized electron beam scattering from a polarized deuterium with the target spin parallel to the direction of the incident electron beam and arranged in each of its $m_I = +1, 0, 1$ sub-states. While $\Delta(x)$ can be measured with an unpolarized electron beam scattering from a polarized deuterium target with the polarization direction perpendicular to the direction of the incident electron beam, and by study the ϕ distribution of the scattered electron. Both of them are from nuclear binding effects and can be taken as tools to obtain new information on nuclear binding effects at the parton level. HERMES is unique to study these structure functions.

1.2.4 Semi-Inclusive Hadron Asymmetry Measurements

There were two interesting semi-inclusive hadron asymmetry measurements:

Measurements for Probing Flavor Dependence

HERMES can provide useful data for semi-inclusive hadron asymmetries. Measurements of spin asymmetries for semi-inclusive hadron production give crucial information about the flavor dependence of quark helicity distributions in the nucleon. The experimental data can also be utilized to sort out the different contributions of the valence and the sea contributions to the quark polarization.

Take the advantage of absence of dilution, HERMES can provide excellent data with semi-inclusive measuring asymmetries.

Measurements for Probing Chiral-Odd Observables

The asymmetry in spin-dependent pion electro-production from a transversely polarized nucleon in the current fragmentation region can be written as:

$$A(x, z) = A_k(Q^2)\frac{\sum_a e_a^2 \left[h_1^a(x)\hat{e}^a(z) + \hat{f}_1^a(z)xg_T^a(x)\right]}{\sum_a e_a^2 f_1^a(x)\hat{f}_1^a(z)} \tag{1.8}$$

where $A_k(Q^2)$ is a kinematic factor, a indicates quark flavor, $g_T(x) = g_1(x) + g_2(x)$, $\hat{f}_1^a$ is the quark fragmentation function obtained from unpolarized semi-inclusive scattering and $\hat{e}_1^a(z)$ is a new chiral-odd fragmentation function. $g_T(x)$ can be determined from the HERMES inclusive spin-dependent measurements. The $h(x)$, which is the leading twist chiral-old spin-dependent structure function and is one of three distributions (the others are $F_1(x)$) and $g_1(x)$) to characterize the state of quarks in the nucleon in leading-order high-energy processes, is connected with the asymmetry $A(x, z)$

1.2.5 Achievements of HERMES

HERMES uses the polarized (spin-oriented) positron or electron beam of DESY's HERA collider incident on a polarized gas-jet target. This, coupled with the HERMES detector's powerful particle identification capability, has allowed the collaboration to measure precisely the contributions to nucleon spin of each valence quark flavour. HERMES' results are in perfect agreement with earlier results and show that the "up" valence quarks spin the same way as the nucleon as a whole, while the "down" valence quarks spin the opposite way, see figure 1.4. HERMES

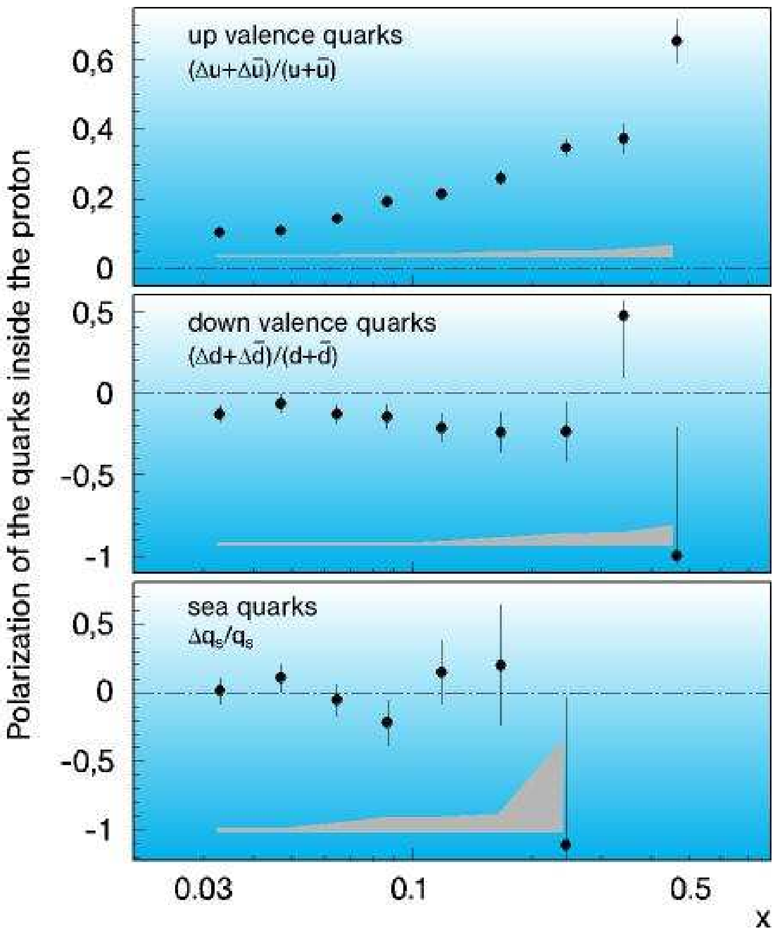

Figure 1.4: Polarization of u(up) quarks, d(down) quarks and sea quarks as a function of x, the momentum fraction of quarks inside the proton. The spins of the up quarks are preferentially aligned with the proton spins, while the down quarks' spins are preferentially opposed. The see quarks hardly contribute to the proton's spin[HER99, DES02].

has also published a first estimate of the gluon contribution to a nucleon's spin. HERA's lepton probes do not see electrically neutral gluons directly, so this is a difficult measurement to make.

HERMES has achieved it by exploiting the process of photon-gluon fusion. When an electron scatters from a quark in a nucleon, it does so through the exchange of a virtual photon, and this photon can interact with gluons as they dissociate into quark-antiquark pairs.

In HERMES' first phase of running, from 1995 to 2000, the experiment showed that gluons do indeed contribute to a nucleon's spin, spinning in the same direction as the nucleon.

For the hardware of the HERMES, one of the most import components is the Spectrometer. It's used to track and identify both the scattered lepton and the produced hadrons.

1.3 HERMES Spectrometer

The setup of the HERMES experiment is shown in figure 1.5. This spectrometer, furnished with a Ring Image Čerenkov counter (RICH) detector, is able to distinguish among pions, kaons and protons, thus allows the semi-inclusive analysis[Dav02]. To detect the particles over a large kinematical range, the spectrometer was designed with a maximum angle acceptance of $40 \sim 140$ mrad in vertical and ± 170 mrad in horizontal direction and can detect the scattered positron down to 0.4 GeV[Ack98]. The spectrometer can be divided into four parts according to their functions:

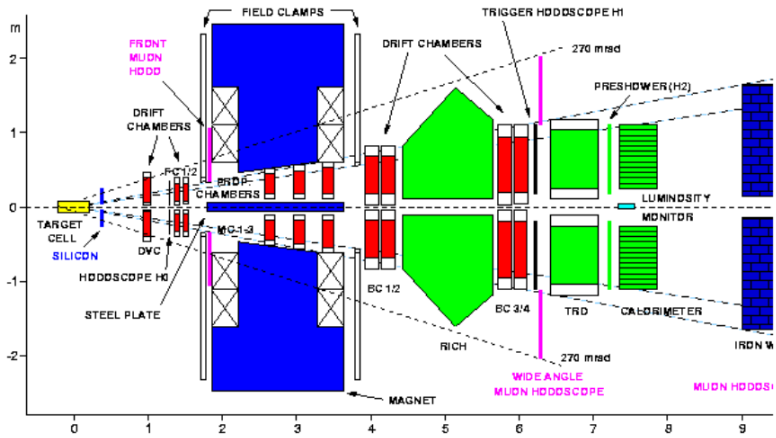

Figure 1.5: Schematic side view of the HERMES experiment. The target section is on the left while the spectrometer on the right side. The HERA beam passes through the target and the spectrometer from left to right.

1.3.1 Instruments for Tracking

The tracks of particles are useful in determining the momenta during the data analysis. To measure the tracks, a dipole magnet is installed to deflect charged particles according to their momenta. To minimize the distortions of the positron beam by the strong field, an iron septum plate is mounted in the horizontal plane housing two beam tubes (one is for the positron beam, the other is a proton tube which is parallel to the positron tube, The direction of the proton beam is opposite to the position beam). Field clamps are installed to cover the front and back opening of the magnet to lower the stray fields in detector regions. Before and after the magnet, there are position sensitive detectors.

The coordinate system used is as follows: the z-axis is the beam direction, the y-axis points upwards, and x-axis is horizontal. The wires and planes in chambers are oriented either in the vertical to measure the x, or titled 30° right (defined as U plane) and left (defined as V plane).

Tracking detectors Before Magnet

The tracking detectors before the magnet consist of[Rit01]:

VC1, VC2 : The Vertex Chambers[Blo99] are located after our target chamber, and are installed in a micro-strip gas chambers (MSGC). The gas composition is DME/Ne(50/50). For the two modules (VC1 and VC2), each has three planes to measure u-, v-, x-direction respectively. Each plane is a $300\mu m$ glass substrate covered with $7\mu m$ wide aluminum anode strips. The space between two strips is $193\mu m$. The resolution/plane (σ) is $65\mu m$. These chambers were not used during the period from 1999-2000.

DVC : The Drift Vertex Chambers are immediately following the VC1 and VC2. They were installed in 1996 and were kept being used since the next year. They have a larger geometrical acceptance than the other detectors, extending from ±35 mrad to ±270 mrad and covering ±200 mrad horizontally, mainly to increase the efficiency for the detection of events from charmed particle decays. The width of the drift cell is $6mm$. The total number of wires is 1088. The non-flammable gas mixture is the same as for all the other drift chambers: $Ar/CO_2/CF_4$(90/5/5), the spatial resolution per plane (σ) is 220 μm.

FC1 and FC2 : The Front Chambers[Bra01] are immediately in front of the magnet are two drift chambers. Each module of chambers has 6 planes of sense/potential wires, two for each direction (x, x', u, u', v, v') interleaved with cathode foils (aluminized mylar). Here, the x', u' and v' indicate the drift chamber planes that staggered by half the width of the drift cell with respect to the corresponding x, u and v planes. The distance between each adjacent planes is half a cell size (3.5mm). The measured resolution per plane is $225\mu m$.

Dipole Magnet Zone

The upper part of the dipole magnet zone is shown in figure 1.6. The magnet chambers $MC1 \sim MC3$[And01] are multi-wire proportional chambers with a spacing of the readout wires of $2mm$ yielding a resolution of $577\mu m$. The chambers are located in the gap of the magnet and were originally intended to help resolve multiple tracks in case of high multiplicity events and to improve track reconstruction matching front and back tracks and to resolve ambiguities. The total number of channels is 11008, and the gas mixture used is $Ar/Co_2/CF_4$ (65/30/5).

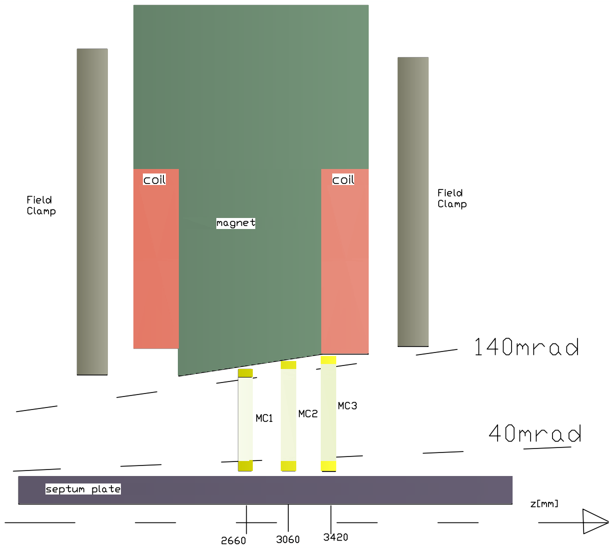

Figure 1.6: Schematic side view of the upper magnet region with magnet chambers in HERMES spectrometer. Space between the dashed lines indicates the acceptance.

Chambers behind the Magnet

There are four drift chambers BC1/2 and BC3/4 as shown in figure 1.5 behind the magnet. These chambers are similar to the FC's. The first two chambers, BC1 and BC2, are placed in front of the Čerenkov detector near the magnet. The other two, BC3 and BC4, are placed behind the Čerenkov detector. The active area for the first sets is $1880 \times 520mm$ while that for the second sets is $2890 \times 710mm$. The average resolutions of the planes inside BC1 and BC2 (BC3 and BC4) are around 275 μm (300 μm). And the values in the middle of the drift cells can reach 210 μm (250 μm).

The momentum resolution of the HERMES spectrometer is in the range from 0.7 to 1.25% and the angular resolution is better than 0.6 mrad over the measured kinematic range.

1.3.2 Particle Identification Detectors

Besides measuring and tracking the particles, to identify the interesting particles is another desirable task for the HERMES experiment. There are four Particle Identification Detectors (PID):

Čerenkov Detector

The detector collects the signals of the Čerenkov radiation caused by charged particles passing a medium with a velocity greater than the speed of light in the medium. The Čerenkov detector in HERMES is a threshold counter with the threshold for different particles in terms of the $\beta_{thr} \equiv \frac{1}{n}$ where n is refractive index of the medium.

The gas filled in the chamber was N_2 in 1995 or a mixture of N_2 and C_4F_{10} in 1996/97 with one atmospheric pressure. The threshold of pion is around 5.5 GeV, and the kaon threshold is 19 GeV while the proton threshold is 38 GeV with N_2 as the radiator. When the material of radiator was replaced by N_2/C_4F_{10}(70/30), the thresholds decreased as 4.0 GeV, for instance. Since 1998, this detector has been replaced by RICH which with clear silica aerogel[Asc00] (refractive index $n = 1.03$, $\gamma_{thresh} = \frac{1}{\sqrt{1-\frac{1}{n^2}}} \approx 4.2$) in front of the detector as radiator and C_4F_{10} (n=1.0005, $\gamma_{thresh} \approx 32$) in the rest volume.

Transition Radiation Detector

The Transition Radiation Detector (TRD) is based on the principle that relativistic particles cause transition radiation when they cross a boundary of two materials with different dielectric indexes. The total energy in X-Ray region emitted by a high-energy particle when it passes through a vacuum-material boundary equals:

$$W = \frac{e^2}{3c}\omega_p\gamma \tag{1.9}$$

where $\gamma = \frac{1}{\sqrt{1-\beta^2}}$. ω_p is the frequency of plasma inside the material, and defined as $\omega_p^2 \equiv \frac{4\pi n_e e^2}{m_e}$. n_e is the density of electrons inside the material with unit $counts/cm^3$. The maximum energy of the X-ray equals $\frac{\hbar}{2}\omega_p\gamma$. The X-ray is in forward direction with the maximum angle around $\frac{1}{\gamma}$[Tan82]. For the HERMES TRD, the typical energy of the X-ray is $2 \sim 15$ keV for particles with $\gamma > 1000$. The positrons with energies above 3 GeV cause much more transitions ($\gamma > 5000$) than that from pions whose $\gamma < 250$ in HERMES experiment. The TRD has 6 modules and each containing a radiator and a detector. The radiator is composed of plastic fibers of about $17 \sim 20\mu m$ in diameter surrounded by Xe/CH_4 (90:10) gas. The X-ray detector is a planar wire chamber with Xe gas[1]. The distance between the vertical wires is $5mm$ in x direction and the distance between two cathode planes is 25mm in the beam (z-) direction. The positron-pion rejection factor of such configuration with six consecutive models is better than 1:100[Ack98].

Hodoscopes

The scintillator hodoscopes H_0, H_1 and H_2 combine with the calorimeter to form the first level trigger. H_0 is mounted in front of the magnet while H_1 is mounted in front of the TRD, and H_2 in front of calorimeter.

[1]Increasing the absorption factor with high z materials

Both of H_1 and H_2 have 42 pieces of scintillators. The H_2 has an additional 11 mm lead sheet in front of the scintillator array as a pre-shower counter. It works based on that positron showers originating from the lead are detected by collecting the scintillation light with photomultipliers mounted to one end of each scintillator slab whereas hadrons do not produce such intensive showers. It can discriminate between electrons and hadrons with a pion rejection factor of ~ 10 and has 90% for electron detection[Rit01].

H_0 was installed in 1996. It consists of a single sheet of scintillator and acts as a trigger eliminator to reduce the background triggers caused by showers generated by the proton beam.

Lead Glass Calorimeter

The calorimeter[Ava98], which can be applied to suppress pions by a factor greater than 10 at first level trigger for scattered electrons and greater than 100 in the off-line analysis for scattered electrons based on measuring the energy deposited in two adjacent columns. It measures the energy of electrons and photons from radiative process, Deeply Virtual Compton Scattering or π^0 and η decays. Radiation resistant F101 lead-glass[Ava96] blocks with a front area of 9×9 cm^2, and a length of 50 cm (about 18 radiation lengths) are stacked in two 42×10 arrays. Each block of the glass is equipped with a photo-multiplier tube at the back. The spatial resolution is about 0.7 cm.

1.3.3 Trigger

For this higher energy experiment, the trigger system must be applied during data taking to select the interesting events and reject the background events. At least four conditions must be met when an event is accepted:

1. The signal in the pre-shower detector has to be above a pre-set value.
2. The signal from the calorimeter corresponding to a deposition of at least greater than the pre-set value, for example: 1.4Gev.
3. The signal in $H1$ has to be coincident with the above two signals.
4. All the signals must be coincident with the bunch crossing time given by the HERA RF signal.

Beside those basic triggers, there are several other triggers to identify different possible hadronic final states. The maximum trigger rate that can be handled by the HERMES data-acquisition (DAQ) system can be at most 500Hz while keeping the dead time less than 10%.

1.3.4 Luminosity Monitor

To analyze the data taken in different time periods and with different spin state of the gas target, the luminosity for each state has to be taken into account. The monitor[Due90, Ben94, Ben98, Wei98] is installed 7.2 m downstream from the center of the target cell. It consists of two small calorimeters. Each one is made of 12 $NaBi(WO_4)$ crystals with the size $22 \times\ 22 \times 200\ mm^2$ in a 3×4 array. Photo-multiplier is added at the back of each block. The measurement is based on three processes:

$e^- + e^- \rightarrow e^- + e^-$ Named Mϕller scattering. When the HERA runs with e^- beam, the electron in beam is scattered off by the target gas electrons.

$e^+ + e^- \rightarrow e^- + e^-$ Called Bhabha Scattering. In case HERA runs with positrons.

$e^+ + e^- \rightarrow \gamma + \gamma$. Positron electron annihilation. When HERA runs with positrons beams.

The two scattered particles from each process are coincidentally measured by the calorimeter. The number of the events is proportional to the electron density of the target and the beam current that can be exactly measured. So the relative changes of the density can be monitored with the system after taking into account the temperature of the target cell and the beam current: The count-rate in the luminosity monitor R_L can be given as:

$$R_L = \varepsilon_L \sigma_w \frac{I_{beam}}{e} \langle n_e \rangle (2L) \tag{1.10}$$

where ε_L is the average total efficiency of the detector including the contribution from the acceptance of detector geometry, the response function for different particles with different energies and the absorb factor due to the materials along the trace from interaction points to the detector. I_{beam} is the HERA beam current. e is the charge of the electron and $2L$ the total length of the target cell. $\langle n_e \rangle$ is the average density of the electrons. $\sigma_w \equiv \frac{\sigma_{M\phi} w_{M\phi} + \sigma_{Bh} w_{Bh} + \sigma_{An} w_{An}}{w_{M\phi} + w_{Bh} + w_{An}}$ is the total weighted average cross section for the three detectable processes, $\sigma_{M\phi}$ is the cross section for $M\phi ller$ scattering process, $w_{M\phi}$ is the weight according to the probability of the $M\phi ller$ scattering process channel, the "Bh" label for the Bhabha scattering and "An" for positron electron annihilation process. Both ε_L and σ_w can be obtained by Monte Carlo simulation methods.

Then the average nucleus[2] volume density $\langle\, n\, \rangle$ can be written as:

$$\langle n \rangle = \langle n_e \rangle = \left(\frac{e}{2L \varepsilon_L \sigma_w} \right) \frac{R_L}{I_{beam}} \propto \frac{R_L}{I_{beam}} \tag{1.11}$$

Because the target density is proportional to $1/\sqrt{T_{cell}}$, one can define the normalized quantity[3]

$$\langle n \rangle_{norm} = \langle n \rangle \sqrt{\frac{T_{cell}}{100}} \propto \sqrt{\frac{T_{cell}}{100}} \cdot \frac{R_L}{I_{beam}} \tag{1.12}$$

With the luminosity monitor, the information about the stability of the ABS can be obtained.

[2]The number of electrons in the target gas equals the number of nuclei for the hydrogen case.

[3]The reference value, $T_{cell} = 100$ K, is the set point of the storage cell temperature during the HERMES running.

1.4 Internal Gas Target

HERMES target is an internal beam gas target. According to the polarization direction against the HEAR electron beam, there are two kinds of polarized hydrogen/deuterium gas targets: longitudinal and transverse. The polarization directions are kept by external magnetic field applied to the region of the gas cell. Since 1996, HERMES has been employing the longitudinal gas target, whose spin orientation was on the same direction as the beam momentum till the end of 2000 and switched into transverse target by changing the magnetic fields from parallel to perpendicular to the beam direction. The polarized gas, ^3He or Hydrogen, are produced by an ABS (**A**tomic **B**eam **S**ource). To analyze the gas characters of the polarized target, TGA (**T**arget **G**as **A**nalyzer), which can measure the ratio between atoms and molecules, and BRP (**B**reit-**R**abi **P**olarimeter) are installed to measure the polarization by determining the populations in different spin states of atoms. The relative positions and skeleton maps of ABS, Target Cell, TGA and BRP are shown in figure 1.7

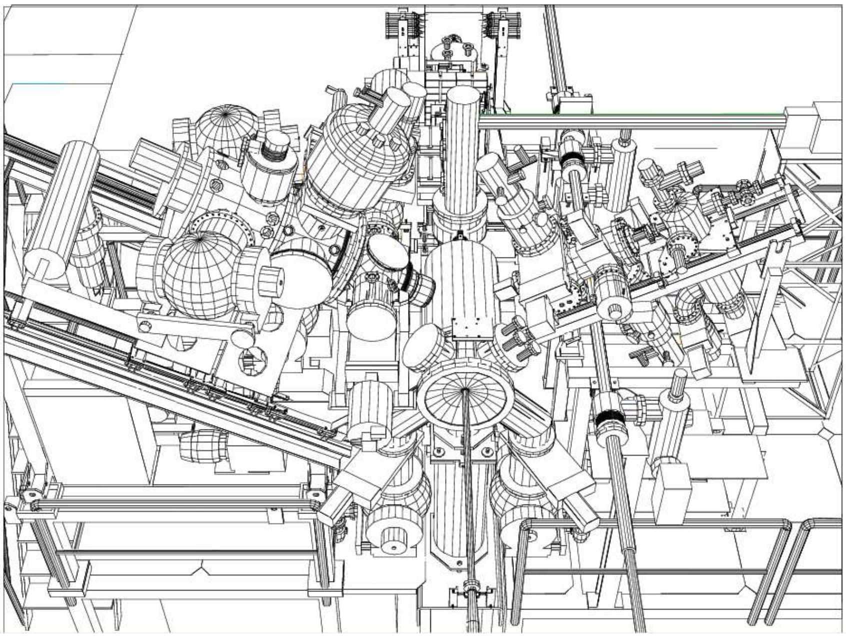

Figure 1.7: Overview of the internal target at HERMES. The viewpoint is at the downstream looking to the upstream along the positron beam line of HERA. The ABS supported by platform (left), the target chamber (center, above the pump stations), the TGA (Right side of target chamber) and BRP (right of TGA) [Kol98]

Besides polarized gas system, there is an UGFS (**U**npolarized **G**as **F**eed **S**ystem), which can be used to inject unpolarized gas to meet the demand of HERMES unpolarized physical program. Several gas, such as H_2, D_2, N_2, ^3He, ^4He, Ne and Kr have been injected through this system in the past several years.

Thanks to the development of storage rings for polarized particles, gas targets become useful. Comparing with solid-state targets for spin experiment, gas targets have significant advantage. They are free of dilution ($f = 1$) and the spin direction can be inversed within milliseconds. Exchanging the spin direction periodically can reduce the systematic errors substantially. The polarization of HERMES target is greater than 0.8. The density of such internal target can be two orders of magnitude higher comparing with a free jet target. This internal technique has been applied or planed to use in several other experiments[Gil93, Dez95, Zap96, Buu00, Ala00, Bar01] since it was first developed in the early '80s[Hae80].

The gas target in HERMES has special disadvantages besides the advantages mentioned above: the polarization of the target can be reduced by the beam bunch induced resonance and the polarization degree is different at different parts of the target cell due to the different wall collisions history and exchange collisions between atoms.

To reduce the resonance induced by the HERA beam, we established a magnetic field stabilizing system which can stabilize the field at the measuring point around $339.100mT$ within $0.05mT$. That is one of my main works that will be presented in this thesis.

For explaining the work, the detailed construction of the target system will be given in next chapter.

Chapter 2

Setup of HERMES Target System

This target started running in 1996. The schematic view of the system is shown in figure 2.1. It's consisted of Atomic Beam Source (ABS), Unpolarized Gas Feed System (UGFS), Storage Cell, Target Magnet, Target Gas Analyzer (TGA) and Breit-Rabi Polarimeter (BRP). In this chapter, I will introduce them along the track of atoms all the way from the source until they have been measured by the BRP.

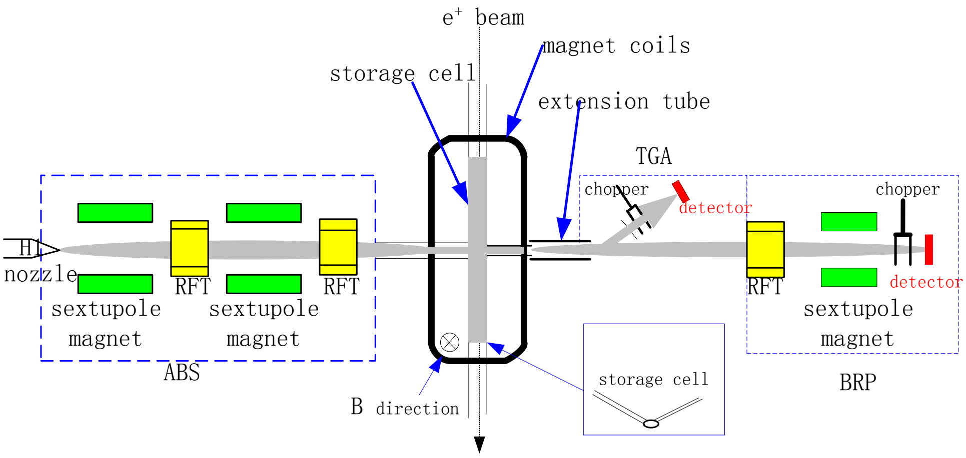

Figure 2.1: A schematic view of the HERMES polarized target. An Atomic Beam Source (ABS) produces polarized jet of atomic hydrogen or deuterium and injects the gas into the cell, while in the other side opposite the ABS is a Target Gas Analyzer (TGA) and a Breit-Rabi Polarimeter (BRP), which are monitoring the target status including the ratio between the number of atoms and molecules (TGA), and the atomic polarization (BRP). A strong magnetic field is applied at the storage cell zone to provide an axis for gas atoms and preventing spin relaxation by effectively decoupling the magnetic moments of electrons and nucleons. The direction of the magnetic field is perpendicular to the HERA beam for the transverse gas target (After 2001) and along the HERA beam for the longitudinal polarized target (Before the end of 2000).

2.1 Atomic Beam Source

For the configuration of the ABS, N. Nass has prepared a detail draw (see figure 2.2). The dissociator breaks the force between two atoms inside H_2 or D_2 molecule. Then the atoms are jetted out through a cooled nozzle (around 100K) and into dissociator chamber, passing a skimmer and then a collimator. The atomic beam is formed before entering the acceptance of a sextupole magnet system. Due to the force from the sextupole magnet is different for different spin states of hydrogen (or deuterium) atoms, the atoms with electron spin $+\frac{1}{2}$ will be focused into the beam axis (the same axis with the magnet) and those with spin $-\frac{1}{2}$ will be diverged off the axis. With different combination among High Frequency Transitions (HFT), different polarization states inside the target storage cell can be obtained. The functions of each component of ABS are presented in figure 2.2.

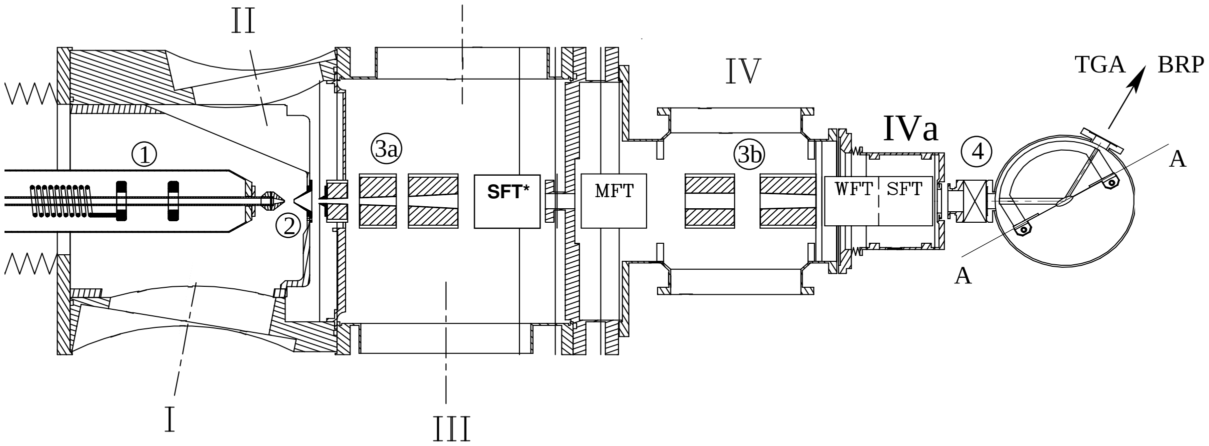

Figure 2.2: The Configuration of HERMES ABS (from downstream of the electron beam) with the radio frequency dissociator (1) and the skimmer (2) for beam formation. Two sets of sextupole magnets (3a, 3b) are located along the beam axis in chamber III and IV. There are the high frequency transitions (MFT, SFT*, WFT and SFT) in both chambers. The axis of the ABS is tilted by 30° downwards with respect to the horizontal plane (A-A). The valve (4) connects the ABS to the target chamber. The electron beam crosses the center of the storage cell perpendicular to the ABS-beam axis. The numbers I - IV denote the pumping stages[Abs02]. The MFT between the sextupole magnets is set as WFT during the Hydrogen running. SFT/WFT are used separately but never to the same time. The geometries of these elements are summarized in table A.1, and the specialities for the pump system are listed in table A.2 of append A.

2.1.1 Radio-Frequency Dissociator

The function of the radio-frequency dissociator (RFD) is to produce the gas (hydrogen or deuterium) in atomic state from molecular state. It consists of a LC-circuit as the only power source to drive the electron impacting the cold plasma inside a water-cooled Pyrex glass tube. The resonance frequency for current RFD is 13.56MHz and RF-power 300W.

After being produced, the atoms of hydrogen (or deuterium) have some probability to recombine into molecules. There are two kinds of recombination: volume recombination and surface catalytic processes recombination. For the volume recombination, much attention should be paid to avoid high-density zone before the gas injected into storage cell in the ABS designing. As for the surface recombination, measurements indicate that the amplitude of recombination coefficient on the surface of the glass tube covered with water vapor is two orders less than that on a bass glass surface. To cover a layer of ice on the surface, small amount of oxygen ($0.1 \sim 0.3$vol%[Kor90]) is added during injecting the gas into the dissociator from the hydrogen generator. For the ABS of HERMES, the average flow rate of oxygen is $0.1\,cm^3/s$ while that for hydrogen is $80\,cm^3/s$.

After the hydrogen (or deuterium) atoms are generated from molecules of H_2 gas by a radio-frequency dissociator, they will jet out from the nozzle. Due to the big difference in pressure and temperature between the zones inside and outside the nozzle, the atoms will be accelerated at the moment before jetting out of the nozzle. To decrease the speed of the atoms for increasing the diverging and focusing ability of the sextupole magnet, a high-power cooling system based on 120W closed-cycle helium is applied to the head of the nozzle. The temperature of the nozzle can be adjusted within the range from $50K$ to room temperature. The water vapor from the dissociator turns into ice at the HERMES working point, 100K. When the inner surface covered by a thin ice layer, it will help preventing the recombination. Unfortunately, when the ice layer gets thicker, the nozzle can be blocked. Once the pressure of dissociate entry is greater than certain value, for instance: 1.4 mbar, we have to warm up the nozzle temperature into room temperature to remove the obstructing ice layer. This trouble will happen every 3 to 5 days during the normal running of HERMES.

The degree of dissociation is defined by:

$$\alpha = \frac{I_a}{I_a + 2I_m}$$

Where I_a and I_m are the intensities of the atomic and molecular fractions respectively. Measurements show the $\alpha \approx 80\%$ (H) and 75% (D) after the nozzle[Koc99].

Besides the RFD, our ABS has been equipped with a microwave dissociator (MWD) since 2000. A plasma source was produced by 2.45GHz wave to discharge D_2 molecules in an air-cooled Pyrex glass tube. The typical throughput using MWD, $Q_{D_2} = 1 - 2mbar \cdot l/s$, is greater than $Q = 1 - 1.5mbar \cdot l/s$ using RFD. The power of microwave is about 600W with $\alpha > 80\%$[Koc99].

2.1.2 Sextupole System

Permanent magnets are used in this sextupole system. To let the deflected atoms escape from the system and lower the residual gas pressure, three sections are divided in the first sextupole magnet (3a) and two sections in the last one (3b). Each section consists of 24 segments permanent magnets enclosed in stainless steel can to avoid chemical destruction by atomic hydrogen. One section of the sextupole magnet is shown in figure 2.4. The magnetization directions for each segment in cross section are shown in figure 2.4.

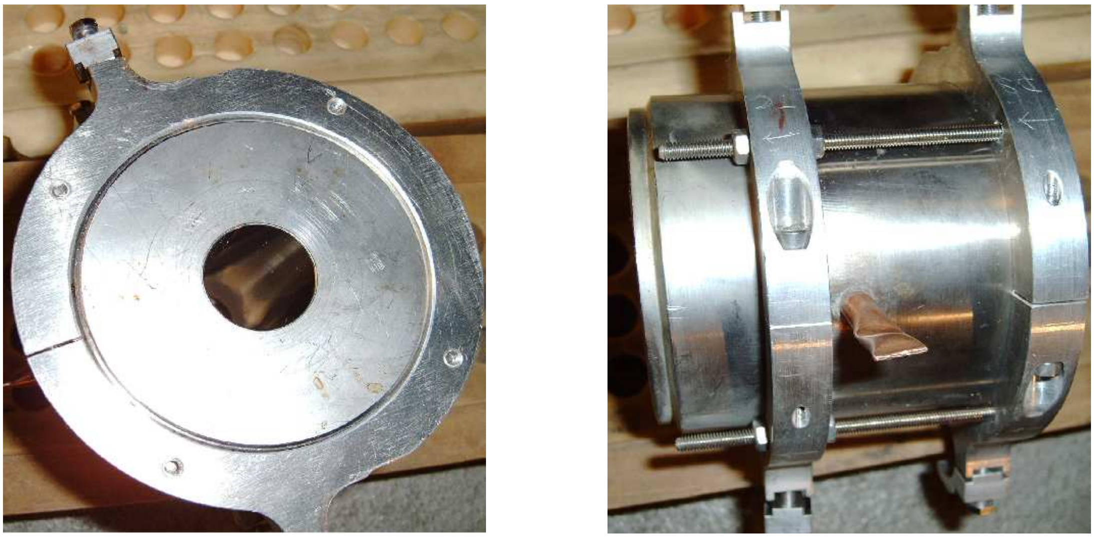

Figure 2.3: Photos of a sextupole permanent magnet in ABS. It is installed at the end of the magnet system near the target chamber. It consists of 24 segments of Vacodym (Magnet based on Nd-Fe-B) enclosed in vacuum tight stainless steal can to prevent chemical destruction by atomic hydrogen.

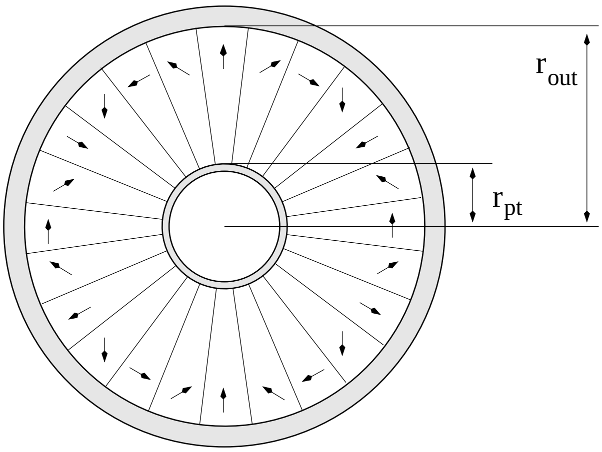

Figure 2.4:
Cross section view of a permanent sextupole magnet used in the ABS. The arrows indicate the magnetization directions of each segment. The maximum pole-tip field is 1.5T.

2.1.3 High Frequency Unit

The function of the High Frequency Unit (HFT) installed in the ABS is to exchange the spin states of atoms to get the needed polarization beam with the help of sextupole magnet system.

The HFT consisting of a resonator cavity and a strong magnet field is called Strong Field Transition (SFT) while the one consisting of a high frequency coil and a weak field called as

Weak Field Unit (WFT) or a medium field named as Medium Field Unit (MFT). The structure of the SFT, MFT and WFT (The only difference is the strength of the magnet fields for the last two) are shown in figure 2.5.

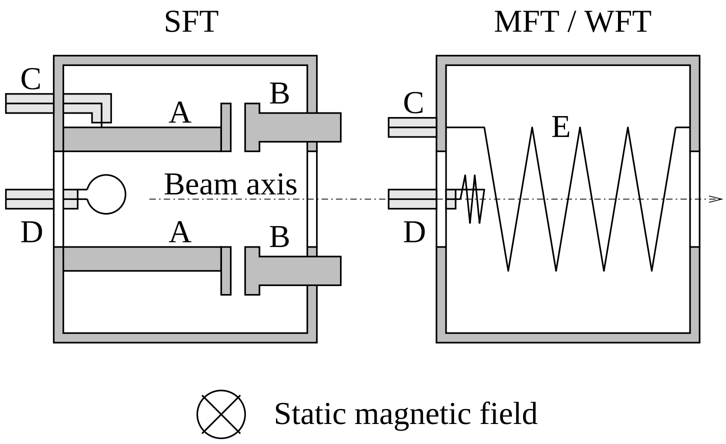

Figure 2.5:
Schematic view of SFT, MFT/WFT units: (A) the resonator rods; (B) the adjustable capacitor; (C) the coaxial RF power input; (D) the pick-up loop; (E) the RF coil. Adjusting the static magnetic field can exchange the right unit as MFT or WFT

There is a magnet field whose strength and gradient along the atomic beam path can be adjusted in each HFT. Two units are used to produce the field: a pair of Helmholtz coils supplies a statistic field while special coils create a spatial gradient field. Due to the gradient changes along the beam path in one direction: the strength of the magnet field continue increasing or decreasing within the spacial region where the HF wave exists, only one resonance can happen during the whole period for a atom passing through the transition considering the frequency of HF wave has been fixed.

For hydrogen and deuterium, the setting of microwave frequency in each unit is different. In case of hydrogen, the MFT (set as 90 MHz), the WFT (set as 14 MHz) and the SFT (the one near the storage cell, set as 1430 MHz) are required. Whereas for deuterium, setting at 25 MHz for the MFT , 7 MHz for the WFT and 370 MHz for the SFT. There is a SFT* between the two sets of sextupole magnets for the calibration in both cases. The statistic field and gradient field are set by scanning the current while monitoring the count rate of BRP.

Different hyperfine states (HFS), see figure 3.1 and figure 3.3 in chapter 3, can be obtained by using various combinations of these high frequency transitions. The detailed combinations and corresponding states for the gas injected into the storage cell are listed in table 2.1.

2.2 Target Storage Cell

The configuration of HERMES storage cell is shown in figure 2.6. The storage cell is made from 75 μm thin pure aluminum sheets. The cell is 400 mm long and the cross section has an elliptical shape with size 29 $\times$ 9.8 mm (long axis/width and short axis/high) for the larger cell and 21 $\times$ 8.9 mm for the small cell. To minimize the surface recombination caused by wall collisions[Bau00, Bau02d], a layer of Drifilm is coated on the inner surface of the cell. The chemical structure of Drifilm is shown in figure 2.7. During the injecting HERA beam, some

Table 2.1: Hyperfine states injected into the target cell produced with various combinations of high frequency transitions. The electron (P_e), nuclear (P_z) and tensor (P_{zz} for Deuterium) polarization of the beam is obtained under ideal condition. The "C" at the last column is for calibration and "D" for the data taking

	HFS injected into the cell	HF Transitions between 6-pole	in IVa (fig. 2.2)	P_e	P_z	P_{zz}	Used for
H	$\|1\rangle$ $\|2\rangle$	-	-	+1	0	-	C
	$\|1\rangle$ $\|4\rangle$	-	SFT 2-4	0	+1	-	D
	$\|2\rangle$ $\|3\rangle$	-	WFT 1-3	0	-1	-	D
	$\|1\rangle$	SFT2-4/MFT 2-3	-	+1	+1	-	C
	$\|2\rangle$	WFT1-3/MFT 1-3	-	+1	-1	-	C
	$\|3\rangle$	SFT2-4/MFT 2-3	WFT 1-3	-1	-1	-	C
	$\|4\rangle$	MFT 1-3	SFT 2-4	-1	+1	-	C
	none	WFT1-3,SFT2-4	-	-	-	-	C
D	$\|1\rangle$ $\|2\rangle$ $\|3\rangle$	-	-	+1	0	0	C
	$\|1\rangle$ $\|6\rangle$	SFT* 3-5	SFT 2-6	0	+1	+1	D
	$\|3\rangle$ $\|4\rangle$	SFT* 2-5	WFT 1-4	0	-1	+1	D
	$\|3\rangle$ $\|6\rangle$	MFT 1-4	SFT 2-6	0	0	+1	D
	$\|2\rangle$ $\|5\rangle$	MFT 1-4	SFT 3-5	0	0	-2	D
	$\|1\rangle$	SFT* 2-6, MFT 3-4	-	+1	+1	+1	C
	$\|2\rangle$	SFT* 2-6, WFT 1-4	-	+1	0	-2	C
	$\|3\rangle$	SFT* 3-5, WFT 1-4	-	+1	-1	+1	C
	$\|4\rangle$	SFT* 2-6, MFT 3-4	WFT 1-4	-1	-1	+1	C
	$\|5\rangle$	SFT* 3-5, WFT 1-4	SFT 3-5	-1	0	-2	C
	$\|6\rangle$	SFT* 2-6, WFT 1-4	SFT 2-6	-1	+1	+1	C

part of the coating may be destroyed by electron or synchrotron radiation. Thanks to the small amount of oxygen injected in the dissociator, the inner surface of the cell will be gradually covered by a thin ice layer under the working temperature, 100 K. The ice coverage can compensate the loss of the Drifilm surface.

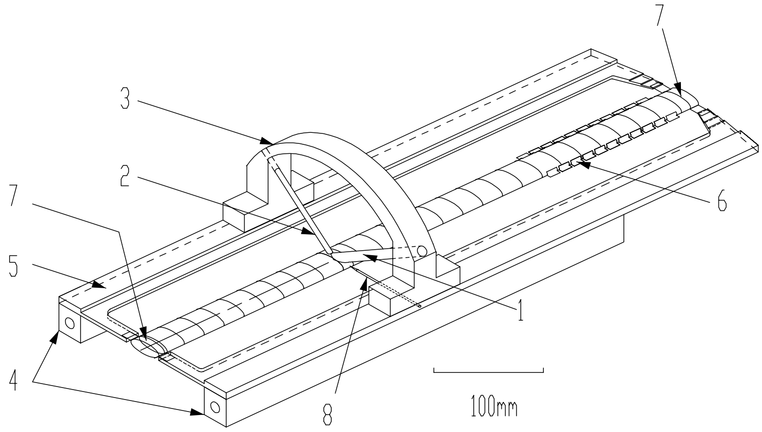

Figure 2.6:
The HERMES target cell. 1) H/D injection tube; 2) Sample tube; 3) Support arch; 4)Cryogenic-cooling and support rails; 5) Support plates; 6) Cell extension with pumping apertures; 7) Cell end support collars; 8)Unpolarized gas feed capillary.

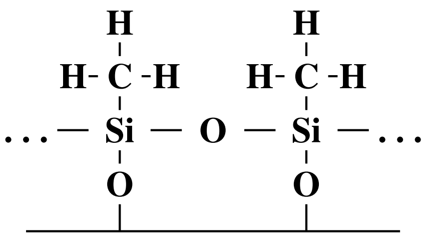

Figure 2.7:
Chemical structure of Drifilm on the inner surface of target storage cell[Cam86, Ste94, Ste95]. Since the Drifilm coating is hydrophobic, adhesion of water drops can be used to test the quality of a coating.

The cell temperature is controlled by an automatic balance system: A gaseous helium cooling system is mounted on the cell support structure while a heater resistor placed inside the helium line. The current of the heater is adjusted while the temperature of the storage cell is monitored. The target thickness and the polarization of the gas inside the cell must be taken into account when choosing the optimization temperature of the cell. The target thickness increases as $1/\sqrt{T}$ with the cell temperature whereas measurement shows extra lower temperature will decrease the polarization. Current setting is 100 K for hydrogen and 60 K for deuterium.

The storage cell is electrically connected as one part of the HERA beam pipe by two wake field suppressors, which are made of copper and designed to guide the electromagnetic high frequency field of the bunched HERA electron beam.

Polarized atoms are injected into the cell by ABS through a 100 mm long and 10 mm diameter tube. The atoms inside the cell can flow through a 100 mm long and 5 mm diameter sample tube into a 10 mm extension tube or directly flow through the cell's ends into a chamber outside the cell. Both the injection tube and sample tube are 30° respecting to the horizontal plane. The chamber is kept under high vacuum around 2×10^{-9} mbar after both tubes are closed for 40 minutes. At the normal running, the vacuum of the chamber is around 1.5×10^{-7} mbar. Two molecular turbo pumps with a total speed of 4400 l/s[Dav02] are running to keep the vacuum of the chamber.

The target cell is immersed in a static magnetic field. The field provides a spin axis and decreases the speed of depolarization.

2.3 Transverse Target Magnet

From 1996 until 2000, the HERMES hydrogen/deuterium gas target is longitudinally polarized respecting to the HERA beam. The direction of the target magnetic field at the cell zone is parallel to the beam.

In July 2001, after the one-year shutdown for updating the HERA luminosity, a transverse target magnet was installed. The field direction of the magnet is perpendicular to the HERA positron beam. The cross section view of the magnet is shown in figure 2.8. This magnet can provide a magnetic field around 0.3 T in the region of the storage cell. The magnetic filed strength was chosen according to the experience accumulated with the longitudinal polarized target of hydrogen, to maintain the polarization degree about 85% a field as strong as 0.3 T is very necessary. The proton polarization as a function of the holding field in case of hydrogen with transverse magnet is shown in figure 2.9.

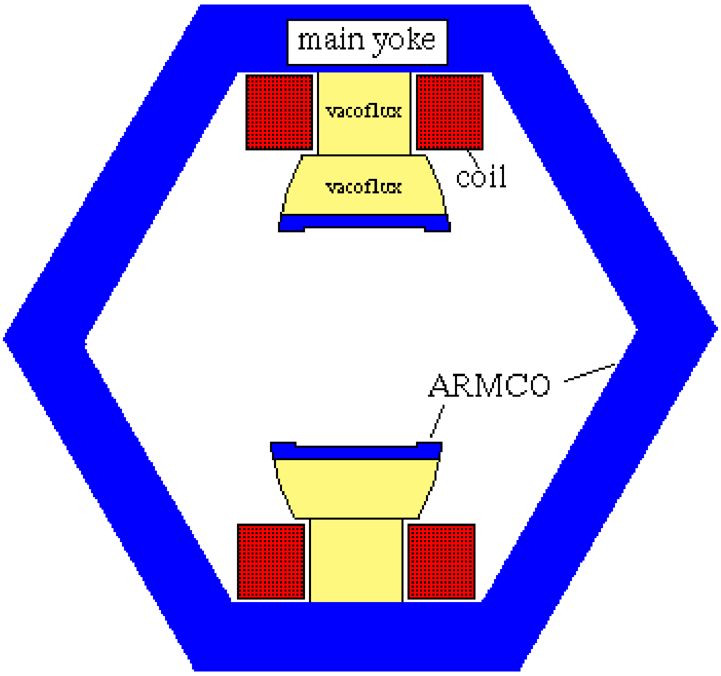

Figure 2.8:
The view of the transverse magnet used in the transverse polarized target of HERMES. The main yoke supports the poles with the coil windings. Two different types of iron were used to manufacture the magnet: iron ARMCO used for the main yoke and the pole tips, VACOFLUX 50, which is an alloy containing 49% Cobalt, 49% Iron, 2% Vanadium and small parts of Nickel, used for the pole[Mar02].

Because the holding field will deflect the HERA positron beam, the strength of the field cannot be too high. The radius of curvature ρ for a charged particle with electric charge e moving in a uniform field can be given by[Cer94]:

$$\frac{1}{\rho}\,[\mathrm{m}^{-1}] = \frac{eB}{P} = 0.2998\frac{B\,[\mathrm{T}]}{P\,[\mathrm{GeV/c}]} \tag{2.1}$$

where B is the field strength and P is the particle's momentum.

For compensating the deflection from the transverse magnet, two correction dipole coils are installed in the upstream and downstream of the HERMES target. During designing, both the synchrotron radiation[Eld47] and beam displacement inside the cell have been taken into account[Dav02].

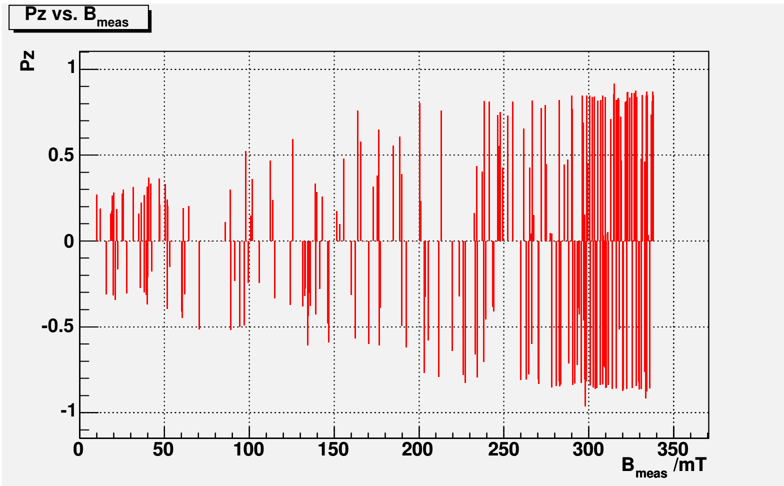

Figure 2.9: The polarization of atoms measured by BRP plotted as a function of the holding field in case of hydrogen with transverse magnetic field. The B_{meas} is the measured value with hall probe. For the measured field equals 339 mT corresponding to the field near the storage cell about ~ 297 mT.

2.4 Unpolarized Gas Feed System (UGFS)

The UGFS is used to inject the unpolarized gas into the storage cell to perform unpolarized physics program of the HERMES experiment. The density of the gas inside the cell can be adjusted by a thermo-valve. Besides the unpolarized physical research, the system can also be used to directly inject the gas into the target gas chamber to perform rest gas calibration[Ye03].

2.5 Target Gas Analyzer (TGA)

The Target Gas Analyzer (TGA) measures the atomic and molecular contents of the gas coming from the storage cell through the sample tube and extension tube. It consists of a chopper, two baffles and a quadrupole mass spectrometer (QMS) with a crossing beam ionizer and a channeltron to detect the ionized atoms and molecules. The schematic view are shown in figure 2.10.

The TGA shares the same vacuum system of the BRP sextupole chamber. Two cryo pumps and a titanium sublimation pump keep the vacuum. The pressure is around 4×10^{-9} mbar in the TGA chamber for the general running after backed with temperatures up to 180 °C. In order not to block the sampled beam into BRP, the TGA is mounted with 7° respecting to the axis of extension tube.

During measurement, the pulses of the channeltron are counted and stored with a multichannel time resolving counter on a digital signal processor (DSP) board. A trigger signal produced by the chopper, which rotates with 5.5 Hz periodically shutting the sampled beam, is used for the synchronization of bin numbers and chopper status. Frequency variation of the chopper can be corrected with the software of DSP. Figure 2.11 shows a spectrum about the count-rates

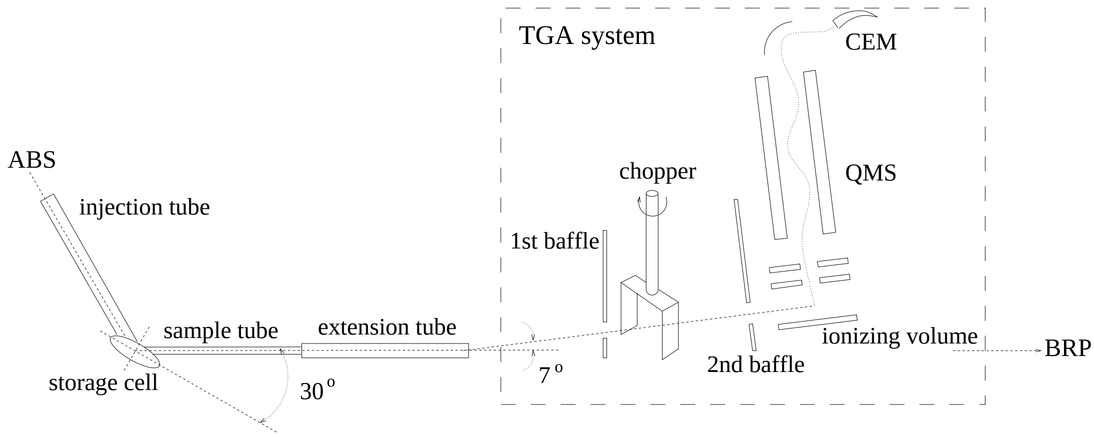

Figure 2.10: Schematic view of the TGA. The gas of atoms and molecules are detected by the channeltron after being ionized. The baffles ensure that the atoms entering the ionizer volume cannot hit the inner ionizer walls and recombine or a virtual molecular beam signal will be produced. The chopper is used for background subtraction.

taken with hydrogen. It is from a time resolving counter (TRC), who has 2048 bins with the bin length equals to 175 μs. The beam rates can be obtained from the difference of the count-rates between the chopper open and close period. The statistics can be given at the same time during analyzing the time spectrum[Bau96].

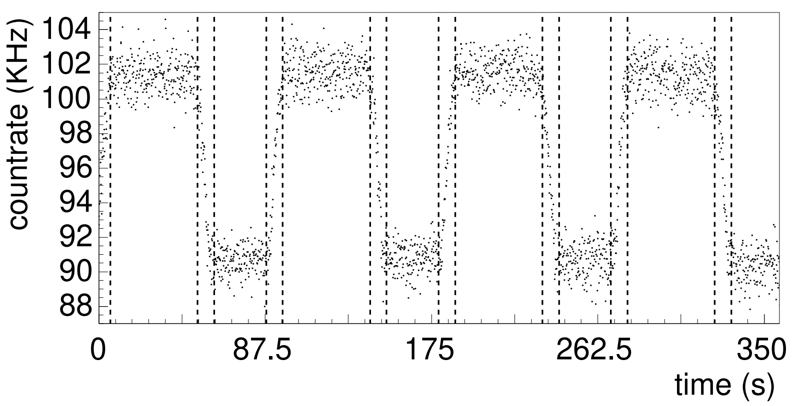

Figure 2.11:
Time spectrum of atomic count-rates in the TGA. The vertical lines indicate the bin numbers corresponding to the limits between the chopper positions open, undefined (transition from open and closed) and closed[Dav02].

The count rates of TGA have to be limited under 1 MHz to avoid the dead time correction. This can be applicable by adjusting the emission current of the cross beam ionizer, which is used to ionize the gas with 70 eV electrons before QMS. The relationship between count rates and the intensity of emission current can be taken as linear, see figure 2.12.

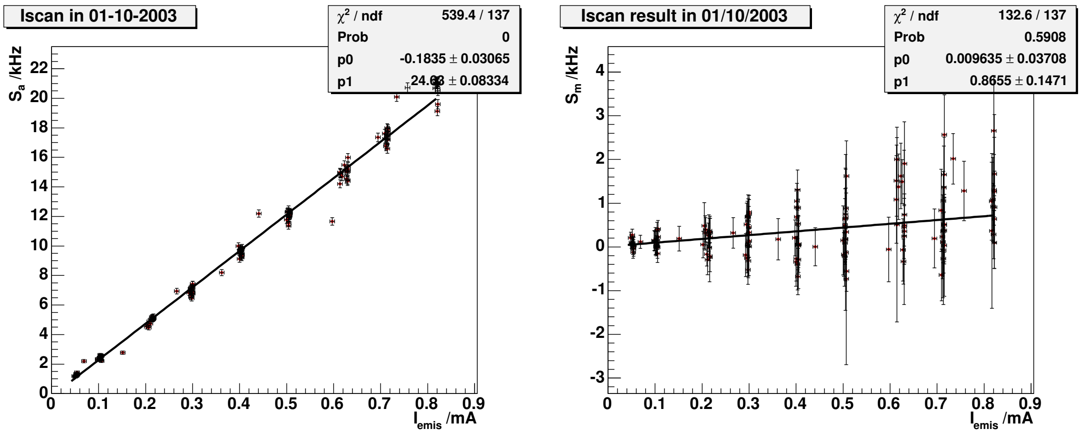

Figure 2.12: Signal of atoms and molecules of hydrogen changes with emission current of TGA. S_a is the signal corresponding to atoms while S_m for molecules of hydrogen. The error bars for the S_m are much bigger than Sa due to the flux of molecules is lower.

2.6 Breit-Rabi Polarimeter (BRP)

The Breit-Rabi Polarimeter is used to provide the polarization degree of the sampled gas by measuring the relative populations n_i of the hyperfine states of hydrogen (or deuterium) atoms contained in the sample beam[Bau02b].

The structure of the BRP is shown in figure 2.13. Two adiabatic high frequency transition (HFT) units are mounted just before the a sextupole system (with two magnets). The HFT units and the sextupole system are located in the sextupole chamber while a chopper and a detector are installed in the detector chamber as shown in figure 2.14. The detector consists of a cross beam ionizer, a quadrupole mass spectrometer (QMS) and a channeltron for single ion detection. The residual pressure inside the sextupole chamber is around 2×10^{-9} mbar and the pressure inside the detector chamber around 2.5×10^{-10}. Two cryo pumps are used for the sextupole chamber while a titanium sublimation pump and ion getter pump are used to keep the ultra high vacuum in the detector chamber. In order to keep the pressure low while regenerating the cryo pumps, both chambers are connected with turbo pumps which are connected with separated fore-pump pump systems.

The SFT and MFT units can turn the atoms into different spin states while the sextuple system filters the sample beam by focusing atoms with $m_s = +\frac{1}{2}$ into the axis direction and deflecting the atoms with $m_s = -\frac{1}{2}$ away from the axis. A beam blocker with 9 mm diameter is placed in front of the first sextuple for decreasing the background. The chopper in front of the detector plays the same role as the one in TGA. The beam shutter just after the extension tube exit is used to measure the contribution of atomic hydrogen coming from the dissociation

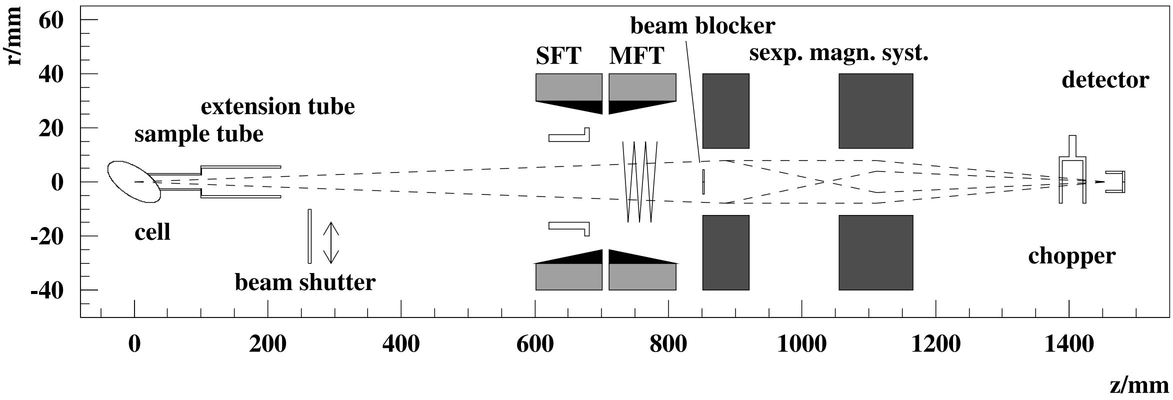

Figure 2.13: Schematic of the BRP setup . The light gray elements are the transition units. The dark gray elements are the sextupole magnets.

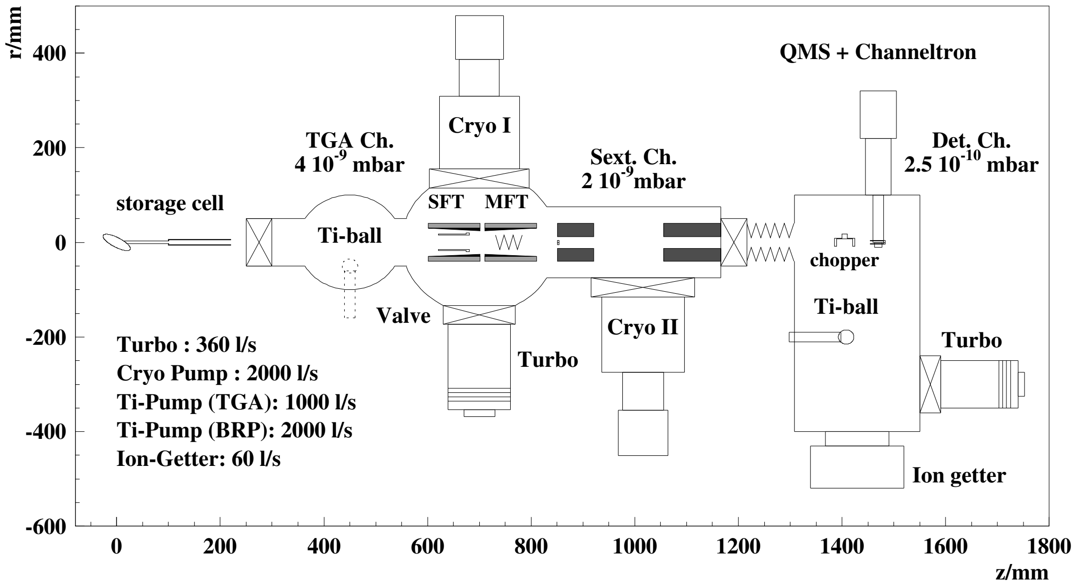

Figure 2.14: Schematic view of the TGA/BRP vacuum system.

of H_2O and H_2 present in the vacuum chambers walls[Dav02].

2.6.1 Polarization Measurement with BRP

During the cell temperature is stable, the atomic signals for different states detected by the BRP are related with the intensity of sampled beam and the transmission probabilities of the HFT and sextupole magnet. The strength of signal S_i for transition units setting i can be expressed as

$$S_i = c \sum_a \left(\sum_b \sigma_b T^i_{ab} \right) I_a \tag{2.2}$$

the I_a is the sampled beam intensity in hyperfine state $|a\rangle$. T^i_{ab} is the exchanging probability between state $|a\rangle$ and $|b\rangle$ in transition units setting i. σ_b is the probability for a atom in state $|b\rangle$ passing through the sextupole system. c is a constant.

For the normal running, using a measured matrix M_{ia} instead of the $\sum_b \sigma_b T^i_{ab}$ for HFT setting i, equation (2.2) can be written as:

$$S_i = c\sum_a M_{ia} I_a \tag{2.3}$$

For a given ABS injection state, BRP transitions units are operated in at least four (six) different modes in case of hydrogen (deuterium). With the knowledge of the matrix, a solution can be obtained with:

$$I_a = c^{-1}\sum_i R_{ai} S_i \tag{2.4}$$

where $R = M^{-1}$. After the intensities for the four (six) states for hydrogen (deuterium) are measured, the total intensity I_{tot} can be obtained by the sum over all hyperfine states:

$$I_{tot} = \sum_a I_a \tag{2.5}$$

Then the component n_a for state $|a\rangle$ in the beam can be easily got by the formula:

$$n_a = \frac{I_a}{I_{tot}} \tag{2.6}$$

Then the polarization of the sampled beam can be got with a theoretical equation:

$$(P_e, P_z)^T = M_P^H (n_1, n_2, n_3, n_4)^T \tag{2.7}$$

$$(P_e, P_z, P_{zz})^T = M_P^D (n_1, n_2, n_3, n_4, n_5, n_6)^T \tag{2.8}$$

The matrix of M_P^H and M_P^D are defined as[Bau00]

$$M_P^H = \begin{pmatrix} 1 & \cos 2\theta & -1 & -\cos 2\theta \\ 1 & -\cos 2\theta & -1 & \cos 2\theta \end{pmatrix} \tag{2.9}$$

and

$$M_P^D = \begin{pmatrix} 1 & C_+ & C_- & -1 & -C_- & -C_+ \\ 1 & \sin^2\theta_+ & -\cos^2\theta_- & -1 & -\sin^2\theta_- & \cos^2\theta_+ \\ 1 & -\frac{1}{2}(3C_+ + 1) & \frac{1}{2}(3C_- - 1) & 1 & -\frac{1}{2}(3C_- + 1) & \frac{1}{2}(3C_+ - 1) \end{pmatrix} \tag{2.10}$$

where $C_\pm = \cos 2\theta_\pm$. The definition of θ for hydrogen and $\theta_\pm$ for deuterium are listed in table 2.2.

Table 2.2: Definition of mixing angles θ (hydrogen) and $\theta_{\pm}$ (deuterium). $x = B_z/B_C$, B_C is the critical field equal to $50.7mT$ for hydrogen and $11.7mT$ for deuterium. ϵ is the correction term for energy of the nucleus, given by $\epsilon = \frac{Sg_I\mu_N}{Ig_S\mu_B}$. The values of $g_I\mu_N$ and $g_S\mu_B$ are provided in table B.1

Hydrogen	Deuterium
$\cos\theta = \sqrt{\frac{1}{2}(1+\cos 2\theta)}$	$\cos\theta_{\pm} = \sqrt{\frac{1}{2}(1+\cos 2\theta_{\pm})}$
$\sin\theta = \sqrt{\frac{1}{2}(1-\cos 2\theta)}$	$\sin\theta_{\pm} = \sqrt{\frac{1}{2}(1-\cos 2\theta_{\pm})}$
$\cos 2\theta = \frac{x(1+\epsilon)}{\sqrt{x^2(1+\epsilon)^2+1}}$	$\cos 2\theta_{\pm} = \frac{3x(1+2\epsilon)\pm 1}{\sqrt{(3x(1+2\epsilon)\pm 1)^2+8}}$
$\sin 2\theta = \frac{1}{\sqrt{x^2(1+\epsilon)^2+1}}$	$\sin 2\theta_{\pm} = \frac{\sqrt{8}}{\sqrt{(3x(1+2\epsilon)\pm 1)^2+8}}$

2.6.2 BRP Calibration

From equation (2.3) we know to calculate the polarization of BRP, we must know the matrix M. M includes the efficiencies of the transition units and the transmission probabilities of the sextupole system for different hyperfine states.

The BRP has two transition units: SFT and MFT. For the SFT, two efficiencies are required in case of hydrogen for the transition $|1\rangle \longleftrightarrow |4\rangle$ (ε_{s14}) and transition $|2\rangle \longleftrightarrow |4\rangle$ (ε_{s24}) and five in case of deuterium. For the MFT, due to the space limitation, SFT can affect the field of the MFT much more than MFT on SFT. The efficiencies MFT must be separately described with each setting of SFT. For hydrogen, the MFT can be tuned either as $|1\rangle \longleftrightarrow |3\rangle$ (using ε_{m13r12} and ε_{m13r23} to describe the efficiencies of two sub-steps: $|1\rangle \longleftrightarrow |2\rangle$ and $|2\rangle \longleftrightarrow |3\rangle$) and $|2\rangle \longleftrightarrow |3\rangle$ (using $\varepsilon_{m23r12} \approx 0$ and ε_{m23r23} to describe the efficiencies of two sub-steps: $|1\rangle \longleftrightarrow |2\rangle$ and $|2\rangle \longleftrightarrow |3\rangle$). There are total 8 efficiencies considering the two states of SFT. For deuterium, the number of efficiencies is much more than this. To describe the MFT efficiencies with different states of SFT, we add additional two subscripts $C14$ (for SFT 1-4 static field on) and $C24$ (for SFT 2-4 static field on).

The number of BRP signals related to different transition states N^H_{BRP} is 11 as shown in table 2.3 while the total number of efficiencies N^H_{eff} is 10 for hydrogen. If ABS is changed among $N^H_{ABS} = 7$ injection modes, the total number of signals is $N^H_s = N^H_{BAS} N^H_{BRP}$. With equation (2.3) we can get N^H_s containing $N^H_u = N^H_{eff} + N^H_{ABS} N^H_{hfs}$ unknowns, where $N^H_{hfs} = 4$ is the number of hyperfine states of hydrogen. The degree of freedom can be written as:

$$\begin{aligned} N^H_f &= N^H_s - N^H_u \\ &= \left(N^H_{BRP} - N^H_{hfs}\right) N^H_{ABS} - N^H_{eff} \\ &= (11-4)\,7 - 10 \\ &= 39 \end{aligned} \tag{2.11}$$

So ten of the unknown transition efficiencies for running with hydrogen can be obtained. The same method can be applied to calibrate transition efficiencies for deuterium.

As for the transitions efficiencies passing through the sextupole system mentioned in equation (2.2), considering the atoms with $m_s = -\frac{1}{2}$ are either defocused or stopped by the beam blocker, the transmission probabilities are zero for $|3\rangle$ and $|4\rangle$ of hydrogen. Using the relative values normalized with equation (2.6) to calculate the polarization, we are only required to calculated the $r_{12} = \frac{\sigma_1}{\sigma_2}$ instead of the absolute values of the transmission probabilities. Considering the small difference of the Stern-Gerlach force from sextupole magnet on the atoms in $|1\rangle$ and $|2\rangle$, the r_{12} should be around 1. After extracting transition efficiencies as functions of the parameter r_{12}, the r_{12} can be evaluated by minimizing χ^2 of the calibration results.

With those instruments: ABS injecting interested states into the target cell while the TGA and the BRP monitoring the target state, the high polarized internal gas target is achieved. The parameters of gas contents and polarization are necessary for physical data analysis work. Of

Table 2.3: Possible switching modes of the BRP transition units and corresponding signals for hydrogen running.

BRP-Signal	Name	MFT-RF	MFT-B	SFT-RF	SFT-B
OFF	off	OFF	OFF	OFF	OFF
SFT 1-4	s14	OFF	OFF	ON	1-4
SFT 2-4	s24	OFF	OFF	ON	2-4
MFT 1-3	m13c14	ON	1-3	OFF	1-4
MFT 1-3	m13c24	ON	1-3	OFF	2-4
MFT 2-3	m23c14	ON	2-3	OFF	1-4
MFT 2-3	m23c24	ON	2-3	OFF	2-4
MFT 1-3/SFT 1-4	m13s14	ON	1-3	ON	1-4
MFT 1-3/SFT 2-4	m13s24	ON	1-3	ON	2-4
MFT 2-3/SFT 1-4	m23s14	ON	2-3	ON	1-4
MFT 2-3/SFT 2-4	m23s24	ON	2-3	ON	2-4

course, the higher of the polarization degree the better!

Chapter 3

Improvement in Target Polarization

For the transverse magnet target, the induced magnetic field by the HERA beam will make the polarization degree decreasing. To minimize or avoid the beam induced depolarization, lots of work has been done to try to fix the holding magnet value at the middle of two resonance points and to make the magnetic field more uniform at the storage cell region.

This chapter deals with the resonance transition theory, the method to make the holding field more uniform, and our discovery of the holding magnetic field changing with time after switching on and how to fix it.

For clearly expressing our work, the knowledge of hydrogen and deuterium hyperfine structure is essential to introduce first.

3.1 Hyperfine Structure in External Magnetic Field

When an atom is put in an external magnetic field, some of energy levels will split into several lines in its atomic spectrum. Those lines are called hyperfine structure. Different hyperfine structure states for hydrogen and deuterium are based on different coupling between the electron spin and nucleus spin.

3.1.1 Hyperfine Structure of Hydrogen

In the case that an hydrogen atom in its ground state $1S_{1/2}$, as a result of absent of the orbital angular momentum, and both the proton and electron are particles with spin $\frac{1}{2}$, they can couple as: $\vec{F} = \vec{S} \cdot \vec{I}$, $S = I = \frac{1}{2}$. A singlet state with total spin $F = 0$ and a triplet with $F = 1$ (with magnetic quantum number $m_F = \pm 1, 0$) are formed. To describe the coupling between the spin of the electron $\vec{S}$ and spin of the nucleus $\vec{I}$ and the additional interactions of the magnetic moments with an external magnetic field $\vec{B}$, a Hamilton operator is defined for a static magnetic field along the z direction, $\vec{B} = (0, 0, B_Z)$, as:

$$\mathcal{H} = A_H \vec{I} \cdot \vec{S} + \frac{g_S \mu_B}{\hbar} S_Z B_Z - \frac{g_I \mu_N}{\hbar} I_Z B_Z \tag{3.1}$$

The constant A_H represents the coupling strength between $\vec{S}$ and $\vec{I}$ for hydrogen. The quantity $\mu_B = \frac{e\hbar}{2m_e c}$ ($\mu_N = \frac{e\hbar}{2m_p c}$) is the Bohr (nuclear) magneton, $g_S = 2.0023$ ($g_I^p = 5.5857,$) is the electron (proton) gyro-magnetic factor.

A_H can be approximately calculated with the following formula:

$$A_H = \frac{2}{3} g_S g_p \frac{m_e}{m_p} m_e c^2 \alpha^4 \left(1 + \frac{m_e}{m_p}\right)^{-3} \frac{1}{\hbar^2} \tag{3.2}$$

Physical constants such as the fine structure α, the mass of an electron m_e and a proton m_p, the speed of light c, used in equation (3.2) are listed in B.1.

The presence of an external magnetic field $\vec{B}$ introduces additional couplings: $S_Z B_Z$ forming the second term of equation (3.1) and $I_Z B_Z$ forming the third. $S_Z = I_Z = \pm\frac{\hbar}{2}$. The contribution from the third one can be neglected due to the nuclear magneton $\mu_N = 3.15245 \times 10^{-8} eVT^{-1}$ is three times less than the Bohr magneton $\mu_B = 5.78838 \times 10^{-5} eVT^{-1}$. After neglecting this term and introducing the Larmor frequency of the electron:

$$\omega_S = \frac{g_S \mu_B}{\hbar} B_Z \tag{3.3}$$

The equation (3.1) can be written as

$$\mathcal{H} = A_H \vec{I} \cdot \vec{S} + \omega_S S_Z \tag{3.4}$$

Considering

$$\vec{S} \cdot \vec{I} = I_Z S_Z + \frac{1}{2}(I_+ S_- + I_- S_+) \tag{3.5}$$

where $I_\pm = I_x \pm i I_y$ and $S_\pm = S_x \pm i S_y$, the matrix elements for Hamilton operator 3.4 can be solved on a base of spin angular momentum eigenfunctions:

$$|m_S, m_I\rangle = \left|\pm\tfrac{1}{2}, \pm\tfrac{1}{2}\right\rangle \tag{3.6}$$

where m_s (m_I) is the magnetic quantum number of electron (nucleon) spin. Eigenvalues of the Hamilton operator in equation (3.4) for four possible states are:

$$\begin{aligned} E_1 &= \tfrac{E^H_{HFS}}{4}\big(1 + 2x(1-\varepsilon_H)\big) & E_3 &= \tfrac{E^H_{HFS}}{4}\big(1 - 2x(1-\varepsilon_H)\big) \\ E_2 &= \tfrac{E^H_{HFS}}{4}\big(-1 + 2\sqrt{x^2(1+\varepsilon_H)^2 + 1}\,\big) & E_4 &= \tfrac{E^H_{HFS}}{4}\big(-1 - 2\sqrt{x^2(1+\varepsilon_H)^2 + 1}\,\big) \end{aligned} \tag{3.7}$$

The energy levels of the hydrogen are shown in figure 3.1.

The magnetic field is scaled by B_C^H, which is named as *critical field* and defined in the condition:

$$\hbar\omega_S = A_H \hbar^2 \tag{3.8}$$

as

$$B_C^H = E^H_{HFS} / g_S \mu_B \simeq 50.7 mT \tag{3.9}$$

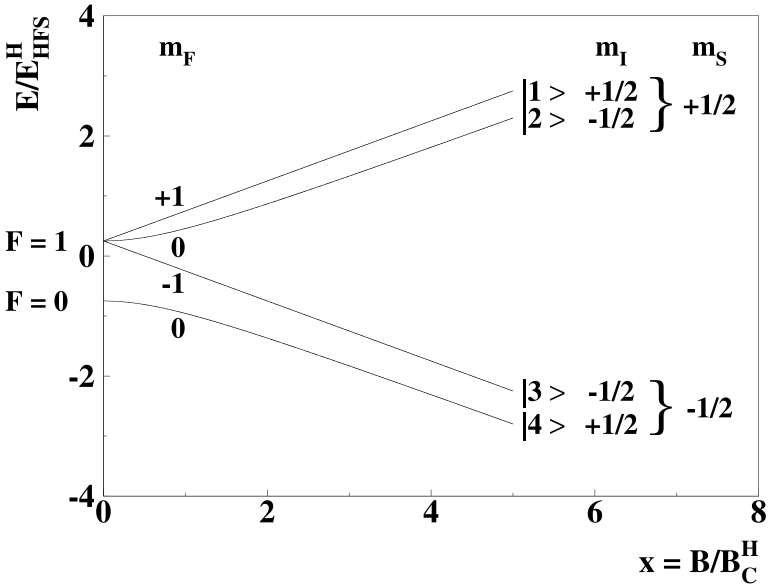

Figure 3.1:
Hyperfine energy levels of the hydrogen change with the magnetic holding field (Breit-Rabi diagram). The energies are for the hyperfine energy E^H_{HFS} and the external magnetic field's values are scaled to the critical field B^H_C.

x in equation (3.7) is defined as the ratio of the external field strength B to the critical field value:

$$x = \frac{B}{B^H_C} \tag{3.10}$$

The hyperfine splitting energy is plotted in the unit:

$$E^H_{HFS} = A_H \hbar^2 \tag{3.11}$$

which is equal to the energy difference between the state $|1\rangle$ and $|2\rangle$, when $x = 1$.

The frequency corresponding to this transition energy was precisely measured as:

$$\nu^H_{HFS} = \frac{A_H \hbar}{2\pi} = 1\ 420\ 405\ 751\ 768(1) Hz \tag{3.12}$$

In different regions of x, the basis used to describe the eigenfunctions are different:

Zeeman region When the external field is very weak, $B \ll B_C$ ($x \ll 1$), the interaction between electron and the external field can be treated as a perturbation. In this case, a basis is given by the eigenstates $|F, m_F\rangle$:

$$\begin{array}{rclcl} |\,1\,\rangle & \simeq & |\,F=1, m_F=+1\,\rangle & = & |\uparrow +\rangle \\ |\,2\,\rangle & \simeq & |\,F=1, m_F=0\,\rangle & = & \frac{1}{\sqrt{2}}(|\uparrow -\rangle + |\downarrow +\rangle) \\ |\,3\,\rangle & \simeq & |\,F=1, m_F=-1\,\rangle & = & |\downarrow -\rangle \\ |\,4\,\rangle & \simeq & |\,F=0, m_F=0\,\rangle & = & \frac{1}{\sqrt{2}}(|\uparrow -\rangle - |\downarrow +\rangle) \end{array} \tag{3.13}$$

where the arrow refers to the electron and the sign to the nuclear spin. The pure states $|\,1\,\rangle$ and $|\,3\,\rangle$ are polarized ($P_e = P_z = \pm 1$), whereas $|\,2\,\rangle$ and $|\,4\,\rangle$ are unpolarized ($P_e = P_z \simeq 0$).

Paschen-Bach limit When $B \gg B_C^H$ ($x \gg 1$). The coupling between nucleon and electron spin can be treated as a perturbation. In this case, a basis for the four states are:

$$
\begin{aligned}
|\,1\,\rangle &= |\uparrow +\rangle & \quad |\,3\,\rangle &= |\downarrow -\rangle \\
|\,2\,\rangle &= |\uparrow -\rangle & \quad |\,4\,\rangle &= |\downarrow +\rangle
\end{aligned}
\tag{3.14}
$$

Others When the external field strength is not so strong that it is in “Paschen-Bach limit” and not so weak that it is in “Zeeman region”, the mixing states $|\,2\,\rangle$ and $|\,4\,\rangle$ at the “Zeeman region” don’t contribute to either Pe or Pz when $m_F = 0$ while in the transition region their contributions grow with the growing field with m_F asymptotically approaches 1 in the “Paschen-Bach limit”. A basis can be used for the four states of the hydrogen in this region:

$$
\begin{aligned}
|\,1\,\rangle &= |\uparrow +\rangle & \quad |\,3\,\rangle &= |\downarrow -\rangle \\
|\,2\,\rangle &= \cos\theta\,|\uparrow -\rangle + \sin\theta\,|\downarrow +\rangle & \quad |\,4\,\rangle &= \sin\theta\,|\uparrow -\rangle - \cos\theta\,|\downarrow +\rangle
\end{aligned}
\tag{3.15}
$$

The θ, so-called *mixing angle*, depends on $x = \frac{B}{B_C}$ and can be derived from the following relations:

$$
\begin{aligned}
\cos\theta &= \sqrt{\tfrac{1}{2}(1+\cos 2\theta)} & \quad \sin\theta &= \sqrt{\tfrac{1}{2}(1-\cos 2\theta)} \\
\cos 2\theta &= \frac{x(1+\varepsilon_H)}{\sqrt{x^2(1+\varepsilon_H)^2+1}} & \quad \sin 2\theta &= \frac{1}{\sqrt{x^2(1+\varepsilon_H)^2+1}}
\end{aligned}
\tag{3.16}
$$

The electrons P_e and nuclei P_z are given in the transition region as:

$$P_e = \sum_{i=1}^{4} n_i \langle\, i\,|\frac{2}{\hbar}S_z\,|\,i\,\rangle = n_1 - n_3 + (n_2 - n_4)\cos 2\theta \tag{3.17}$$

$$P_z = \sum_{i=1}^{4} n_i \langle\, i\,|\frac{2}{\hbar}I_z\,|\,i\,\rangle = n_1 - n_3 - (n_2 - n_4)\cos 2\theta \tag{3.18}$$

where n_i is the relative population of state $|\,i\,\rangle$. Total sum of the n_i equals 1 ($\sum_i n_i = 1$).

The relationships of P_e and P_z in the four states of hydrogen atoms chang with the external field strength are shown in figure 3.2.

3.1.2 Hyperfine Structure of Deuterium

Due to the nuclear spin of the deuteron $I = 1$, the hyperfine splitting of the deuterium atom is very different from that of the hydrogen atom. The total angular momentum of $F = \frac{3}{2}$ ($m_F = \pm\frac{3}{2} \pm \frac{1}{2}$) or $F = \frac{1}{2}$ ($m_F = \pm\frac{1}{2}$) can be achieved by the coupling between the spin of the electron shell and nuclear shell. For the condition that has no external magnet, the state

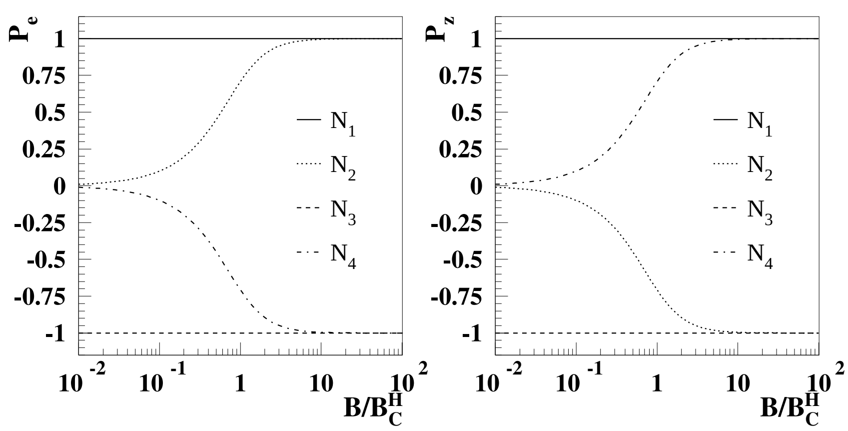

Figure 3.2: The values of electronic (left) and nuclear polarizations of the four hydrogen hyperfine states change with the strength of external magnetic field. The field values use critical field B_C^H as its unit.

$F = \frac{3}{2}$ is four times degenerated while the state $F = \frac{1}{2}$ is twice degenerated. With the external magnet, the states will be broken into six hyperfine energy levels.

The energy levels are the function of the strength of external magnet. The energy eigenvalues of the individual state can be written as:

$$\begin{aligned}
E_1 &= \tfrac{E^D_{HFS}}{3}\left(1 + \tfrac{3}{2}x(1-2\varepsilon_D)\right) \\
E_2 &= \tfrac{E^D_{HFS}}{6}\left(-1 + \sqrt{9x^2(1+2\varepsilon_D)^2 + 6x(1+2\varepsilon_D) + 9}\,\right) \\
E_3 &= \tfrac{E^D_{HFS}}{6}\left(-1 + \sqrt{9x^2(1+2\varepsilon_D)^2 - 6x(1+2\varepsilon_D) + 9}\,\right) \\
E_4 &= \tfrac{E^D_{HFS}}{3}\left(1 - \tfrac{3}{2}x(1-2\varepsilon_D)\right) \\
E_5 &= \tfrac{E^D_{HFS}}{6}\left(-1 - \sqrt{9x^2(1+2\varepsilon_D)^2 - 6x(1+2\varepsilon_D) + 9}\,\right) \\
E_6 &= \tfrac{E^D_{HFS}}{6}\left(-1 - \sqrt{9x^2(1+2\varepsilon_D)^2 + 6x(1+2\varepsilon_D) + 9}\,\right)
\end{aligned} \tag{3.19}$$

where $\varepsilon_D = \frac{g_I \mu_K}{g_S \mu B} = 2.3\dot{1}0^{-4} \ll 1$. $E^D_{HFS} = \frac{3}{2}A_D\hbar^2 = 1.35 \times 10^{-6}eV$ corresponds to frequency $\nu^D_{HFS} = 327.4MHz$. The A_D can be calculated with a equation like equation (3.2) except using g_d (gyro-magnetic factor of deuterium, refer to table B.1) instead of g_p.

The relationship between the energy levels of the deuterium and the strength of the external magnetic field is shown in figure 3.3. While a basis for the deuterium corresponding to eigenvalues in equation (3.19) is written as:

$$\begin{aligned}
|\,1\,\rangle &= |\uparrow +1\,\rangle & |\,4\,\rangle &= |\downarrow -1\,\rangle \\
|\,2\,\rangle &= \cos\theta_+\,|\uparrow 0\,\rangle + \sin\theta_+\,|\downarrow +1\,\rangle & |\,5\,\rangle &= \sin\theta_-\,|\uparrow -1\,\rangle - \cos\theta_-\,|\downarrow 0\,\rangle \\
|\,3\,\rangle &= \cos\theta_-\,|\uparrow -1\,\rangle + \sin\theta_-\,|\downarrow 0\,\rangle & |\,6\,\rangle &= \sin\theta_+\,|\uparrow 0\,\rangle - \cos\theta_+\,|\downarrow +1\,\rangle
\end{aligned} \tag{3.20}$$

The polarization of P_e and P_z is defined as:

$$P_e = \sum_{i=1}^{6} n_i \langle\, i\,|\,\frac{2}{\hbar}S_z\,|\,i\,\rangle = n_1 - n_4 + (n_2 - n_6)\cos 2\theta_+ + (n_3 - n_5)\cos 2\theta_- \tag{3.21}$$

$$P_z = \sum_{i=1}^{6} n_i \langle\, i\,|\,\frac{1}{\hbar}I_z\,|\,i\,\rangle = n_1 + n_6 - n_3 - n_4 + (n_2 - n_6)\sin^2\theta_+ + (n_3 - n_5)\sin^2\theta_-$$

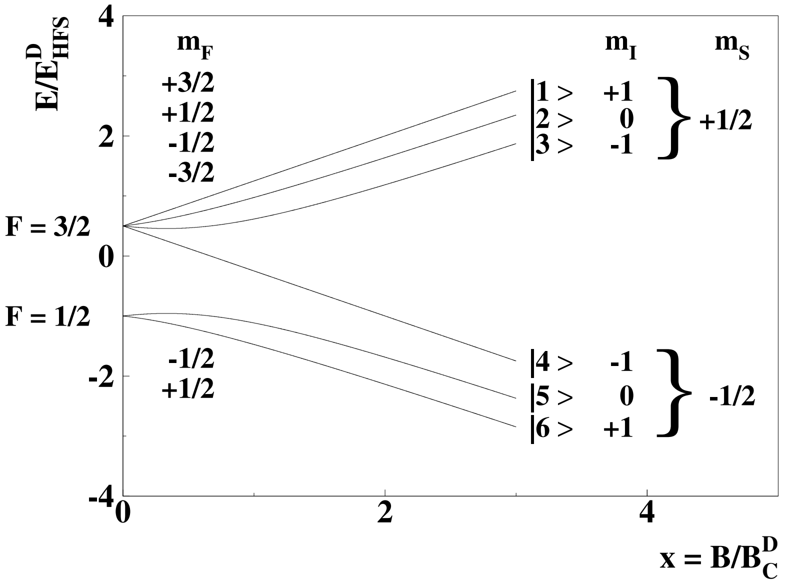

Figure 3.3:
Breit-Rabi diagram of deuterium. The energies are scaled to E^D_{HFS} and external magnetic field's values are scaled to B^D_C

where the mixing angle θ_+ and θ_- can be derived from equation (3.22):

$$\begin{aligned} \cos\theta_\pm &= \sqrt{\tfrac{1}{2}(1+\cos 2\theta_\pm)} & \sin\theta_\pm &= \sqrt{\tfrac{1}{2}(1-\cos 2\theta_\pm)} \\ \cos 2\theta_\pm &= \frac{3x(1+2\varepsilon_D)\pm 1}{\sqrt{(3x(1+2\varepsilon_D)\pm 1)^2+8}} & \sin 2\theta_\pm &= \frac{\sqrt{8}}{\sqrt{(3x(1+2\varepsilon_D)\pm 1)^2+8}} \end{aligned} \tag{3.22}$$

3.2 Hyperfine Transitions

Hyperfine transitions play a central role in the target designing work. First, the high frequency transition (HFT) units as adiabatic transitions are used in the ABS to exchange the hyperfine population of two states in one or several steps to get the polarized target in different polarized states. Secondly, transitions due to the wall or volume collisions will cause depolarization of the gas target. Thirdly, the microwave caused by the HERA beam will cause depolarization transition inside the gas target also. Since reducing the depolarization from the resonance induced by the bunch field is one of the main part of this thesis, Detailed introduction about the hyperfine transition will be given here.

Using the Hamilton operator (3.1) in the Schrödinger equation to one of its eigenstates Ψ:

$$i\hbar\frac{\partial}{\partial t}\Psi = \mathcal{H}\Psi \tag{3.23}$$

If one multiplies from the left with the orthonormal operator U_0[1] , one has:

$$i\hbar\frac{\partial}{\partial t}\left(U_0^T\Psi\right) = \mathcal{H}\left(U_0^T\Psi\right)$$

[1]where the orthonormal matrix U_0 is given for hydrogen by

$$U_0 = \begin{pmatrix} 1 & 0 & 0 & 0 \\ 0 & \cos\theta & 0 & -\sin\theta \\ 0 & 0 & 1 & 0 \\ 0 & \sin\theta & 0 & \cos\theta \end{pmatrix}$$

$$i\hbar\left(\frac{\partial}{\partial t}U_0^T\Psi + U_0^T\frac{\partial}{\partial t}\Psi\right) = \left(\mathcal{H}U_0^T + U_0^T\mathcal{H}\right)\Psi$$

$$i\hbar\left(\frac{\partial}{\partial t}U_0^T\Psi + U_0^T\frac{\partial}{\partial t}\Psi\right) = \left(i\hbar\frac{\partial}{\partial t}U_0^T + U_0^T\mathcal{H}\right)\Psi \tag{3.24}$$

Applying $U_0^T U_0 = \mathbf{1}$ in the right of the equation (3.24), one obtains:

$$i\hbar\left(\frac{\partial}{\partial t}U_0^T\Psi + U_0^T\frac{\partial}{\partial t}\Psi\right) = \left(i\hbar\frac{\partial}{\partial t}U_0^T U_0 + U_0^T\mathcal{H}U_0\right)U_0^T\Psi \tag{3.25}$$

Changing the basis by means of the transformation $\Phi = U^T\Psi$, one can get:

$$i\hbar\frac{\partial}{\partial t}\Phi = \left(i\hbar\frac{\partial}{\partial t}U_0^T U_0 + \mathcal{H}_1^{st}\right)\Phi \tag{3.26}$$

where $\mathcal{H}_1^{st}$ represents the diagonal static Hamiltonian[Dav02].

When holding field changes with time, the term $i\hbar\frac{\partial}{\partial t}U_0^T U_0$ is non-zero. In such case, the distortion of the eigenstates by the field may cause transitions between pairs of hyperfine states.

A hyperfine transition has a defined frequency ν_{ab}, related to the energy difference between the two hyperfine states $E_a - E_b$ of transition $a \leftrightarrows b$:

$$\nu_{ab} = \frac{|E_a - E_b|}{2\pi\hbar} \tag{3.27}$$

Two kinds of hyperfine transitions can be classified depending on the relative orientations of the static holding field $\vec{B}^{st}$ and the time dependent one $\vec{B}(t)$: Transitions caused by the component of $\vec{B}(t)$ parallel to the static one are called σ, whereas transitions generated by the perpendicular component of $\vec{B}(t)$ are called π transitions.

The transition types and corresponding change in Δm_F and ΔF are shown in table 3.1 for the HFT used in ABS and BRP.

3.3 Hyperfine Resonance Transitions in Bunch Field Induced by HERA Beam

The polarized hydrogen/deuterium gas of the HERMES target is immersed in a static strong magnetic field, which provides the target spin direction. The field can also ensure high polarization of the mixed hyperfine states by effectively decoupling the electrons and nucleons magnetic moments.

---

and

$$U_0 = \begin{pmatrix} 1 & 0 & 0 & 0 & 0 & 0 \\ 0 & \cos\theta_+ & 0 & 0 & 0 & 0 \\ 0 & 0 & \cos\theta_- & 0 & -\sin\theta_+ & 0 \\ 0 & 0 & 0 & 1 & 0 & 0 \\ 0 & 0 & \sin\theta_- & 0 & \cos\theta_- & 0 \\ 0 & \sin\theta_+ & 0 & 0 & 0 & \cos\theta_+ \end{pmatrix}$$

for deuterium

Orientation	σ/π	Type	Δm_F	ΔF	Δm_I	Δm_S	Hydrogen	Deuterium
$B(t) \| B^{st}$	σ	SFT	0	±1	±1	±1	$2 \leftrightarrow 4$	$2 \leftrightarrow 6$
$B(t) \| B^{st}$	σ	SFT	0	±1	±1	±1		$3 \leftrightarrow 5$
$B(t) \perp B^{st}$	π	SFT	±1	±1	0	±1	$1 \leftrightarrow 4$	$1 \leftrightarrow 6$
$B(t) \perp B^{st}$	π	SFT	±1	±1	0	±1		$2 \leftrightarrow 5$
$B(t) \perp B^{st}$	π	SFT	±1	±1	±2	±1		$3 \leftrightarrow 6$
$B(t) \perp B^{st}$	π	SFT	±1	±1	±1	0	$3 \leftrightarrow 4$	$4 \leftrightarrow 5$
$B(t) \perp B^{st}$	π	MFT	±1	0	±1	0	$1 \leftrightarrow 2$	$1 \leftrightarrow 2$
$B(t) \perp B^{st}$	π	MFT	±1	0	±1	0		$2 \leftrightarrow 3$
$B(t) \perp B^{st}$	π	MFT	±1	0	±1	0		$5 \leftrightarrow 6$
$B(t) \perp B^{st}$	π	MFT	±1	0	0	±1	$2 \leftrightarrow 3$	
$B(t) \perp B^{st}$	π	MFT	±1	0	0	±1		$3 \leftrightarrow 4$

Table 3.1: The possibilities of hyperfine transitions of hydrogen and deuterium. The values Δm_I and Δm_S are valid in the high holding field regime, where the eigenstates of the static Hamiltonian can be approximated by $|\uparrow +\rangle$, $|\uparrow -\rangle$, $|\downarrow +\rangle$, $|\downarrow -\rangle$ for hydrogen and $|\uparrow 1\rangle, |\uparrow 0\rangle, |\uparrow -1\rangle, |\downarrow 1\rangle, |\downarrow 0\rangle, |\downarrow -1\rangle$ for deuterium

During data taking of HERMES, an additional time dependent magnetic field induced by the bunched positron current is presented. The field temporal structure can be decomposed in terms of Fourier's harmonics. Those can make the target depolarized by resonance transition when the values of static holding magnetic field meet certain condition.

3.3.1 HERA Positron Beam Structure

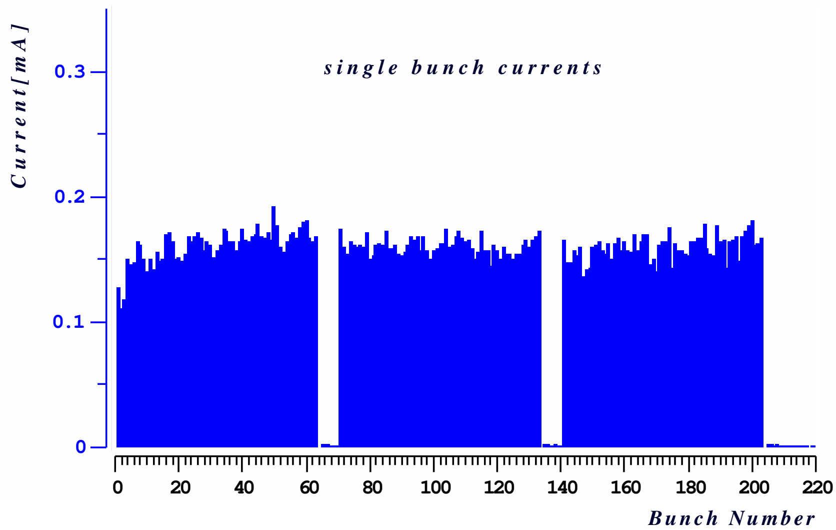

Figure 3.4:
The structure of the HERA positron beam. Typically almost all 220 bunches are filled with approximately the same amount of positrons. Some of the bunches are left empty

As shown in figure 3.4, The HERA positron beam is composed of 220 bunches. Each bunches can be filled with around $3.6 \cdot 10^{10}$ particles and is circling in the storage cell with a frequency around $\nu_L = 47.36\,\text{kHz}$. The time interval between two bunches is very easy to be calculated $\tau = \frac{1}{47.36kHz\times 220} = 96\,\text{ns}$. The longitudinal structure of the single bunch has a Gaussian shape, whose width is made very short ($\sigma_z = 11.3\,\text{mm}$ or, equivalently, $\sigma_t = 37.7\,\text{ps}$ for the 27.5 GeV positron beam) in order to provide optimization luminosity for the colliding experiments[Dav02].

Due to each bunch consists roughly the same amount of positron/electron (see figure 3.4), the total beam current can be approximately described by a periodic function:

$$I(t) = I_0 \exp\Big[-\frac{t^2}{2{\sigma_t}^2}\Big] \qquad -\frac{\tau}{2} \leq t \leq \frac{\tau}{2} \qquad \tau = 96\,\text{ns} \tag{3.28}$$

where I_0 is the single bunch peak current.

The amplitude of the infinite harmonics can be given after Fourier transform analysis of the (3.28) from time structure of the positron beam field to the frequency spectrum:

$$a_n(\nu_n) = 2I_{tot} \exp\Big[-\frac{{\nu_n}^2}{2{\sigma_\nu}^2}\Big] \qquad \text{n=1,2,...} \tag{3.29}$$

where the I_{tot} is the integrated beam current, n is the harmonic number and $\nu_n = \frac{n}{\tau}$ the corresponding frequency.

The frequency spacing between two subsequent harmonics can be calculated with the time interval τ:

$$\Delta\nu = \frac{1}{\tau} = 10.42\,\text{MHz} \tag{3.30}$$

The width of the Fourier convolution can be given by

$$\sigma_\nu = \frac{1}{2\pi\sigma_t} = 4.22\,\text{GHz} \tag{3.31}$$

The number of the harmonics within the width, whose amplitude is comparable with the fundamental one, is around 405 (calculated with $\frac{\sigma_\nu}{\Delta\nu}$).

A schematic plot of the Fourier transform of the beam is shown in figure 3.5. The electromagnetic field induced by positron beam is shown with “circulate” lines around the axis of the positron beam in figure 3.6.

3.3.2 Resonance Conditions

In the HERMES storage cell, a resonance transition will happen between two hyperfine states $|\,a\,\rangle$ and $|\,b\,\rangle$ of hydrogen or deuterium when one of the frequency ν_n equals the frequency difference of the hyperfine states:

$$\nu_{ab} = \frac{|E_a - E_b|}{2\pi\hbar} = \nu_n \qquad \text{n=1,2,...} \tag{3.32}$$

where E_a and E_b are the eigenenergies of states $|\,a\,\rangle$ and $|\,b\,\rangle$.

After calculating the strength of the magnetic field at the discrete values of ν_n with the equation (3.32), we can get the resonance points corresponding to different harmonics of the induced field by HERA beam. Those results are shown in figure 3.7.

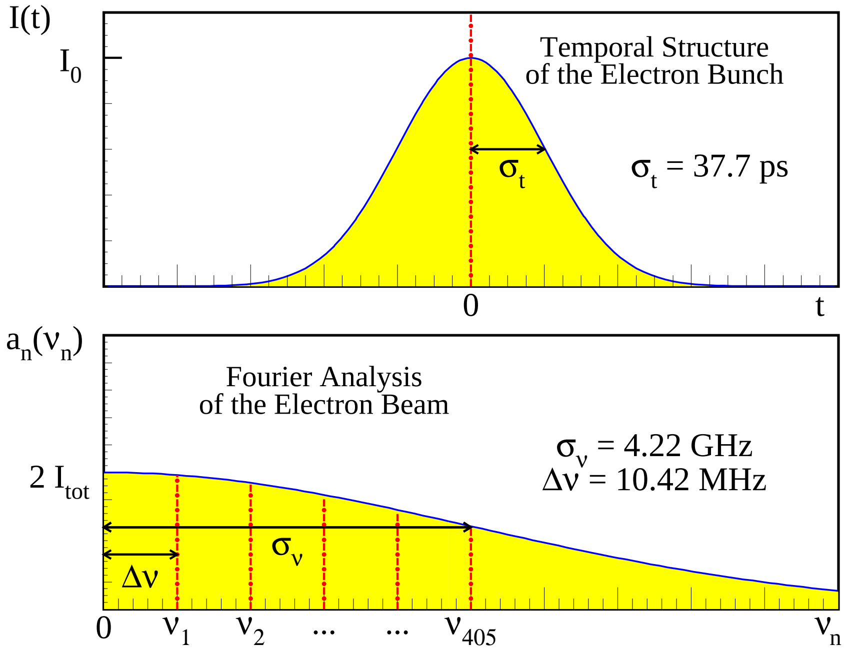

Figure 3.5:
Bunch shape of one of 220 HERA e-beam bunches (top). The frequency distribution of the bunch decomposed by Fourier transformation from time field to frequency field (bottom).

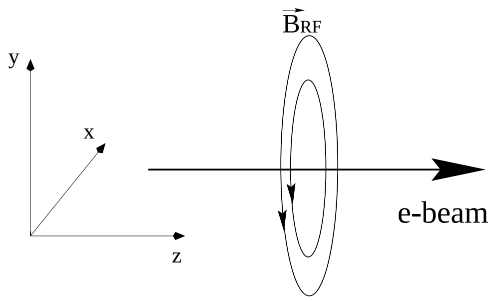

Figure 3.6:
The orientation of the electromagnetic field induced by the HERA positron beam current.

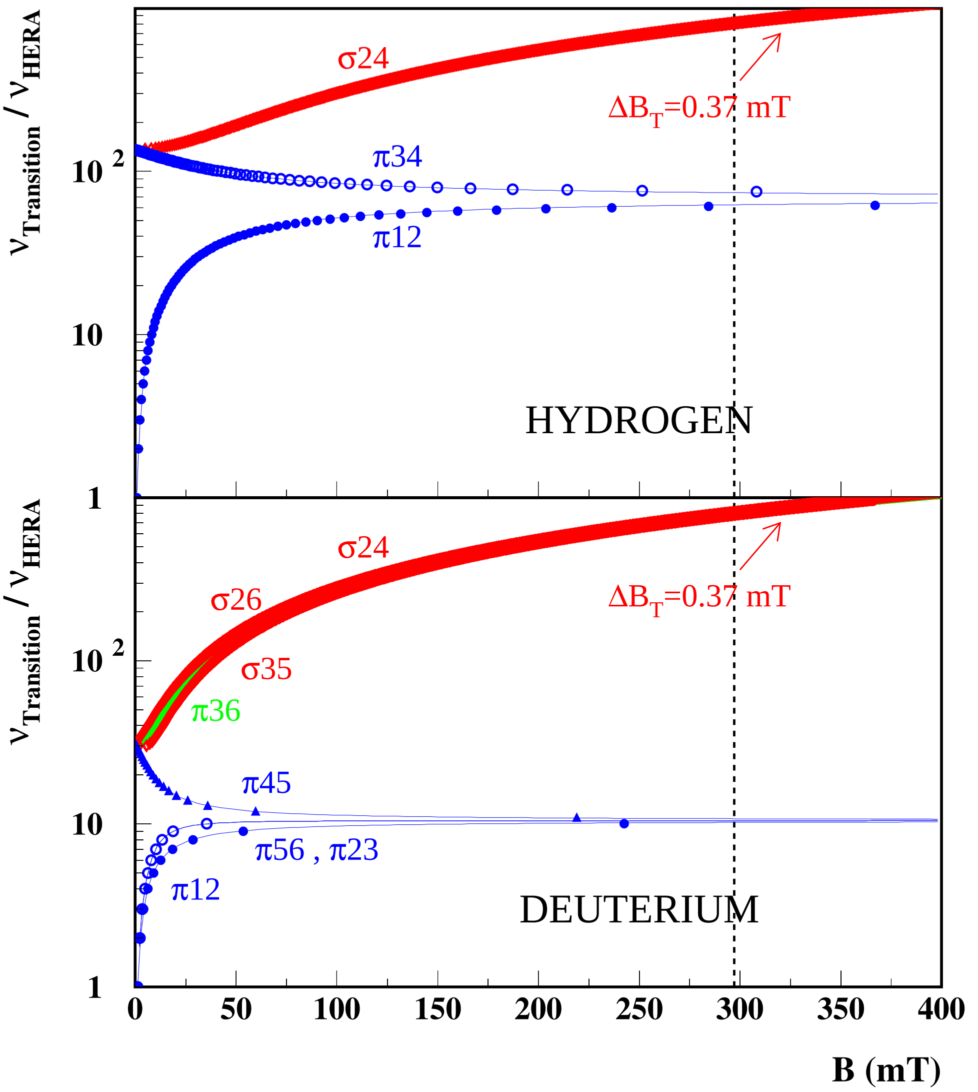

Figure 3.7:
Possible beam induced nuclear depolarization resonance in the HERMES target. The frequency differences between pairs of hydrogen hyperfine states whose transitions lead to nuclear depolarization are plotted as a function of the holding field. The frequency values are normalized to $\nu_{HERA} = 10.42\,\mathrm{MHz}$. The marks, representing the resonance condition, are clearly distinguishable for the π transitions, while they overlap with each other in case of σ and $\pi\,|\,3\,\rangle \leftrightarrow |\,6\,\rangle$ transitions. The dashed line represents the working point of the transversely polarized target[Dav02].

3.3.3 Transition Probability

For the static holding field of HERMES transverse target, the strength of magnetic field is around 297 mT, so the beam induced time dependent field can be treated as perturbation. Taking the interaction time as τ, the transition probability between two hyperfine states $|\,a\,\rangle$ and $|\,b\,\rangle$ is obtained at the first order perturbation by [Mes61, Coh77]:

$$W_{ab} \simeq \left(\frac{y_{\pi,\sigma} E_{HFS}}{\hbar}\right)^2 |V_{ab}|^2 f(\nu - \nu_{ab}, \tau) \tag{3.33}$$

where the matrix element V_{ab} is defined as

$$V_{ab} = \frac{\langle\, i\,|\,\mathcal{H}_1^{\pi,\sigma}\,|\,n\,\rangle}{y_{\pi,\sigma} E_{HFS}} \tag{3.34}$$

with $y_{\pi,\sigma} = \frac{b(t)}{B_C}$. The $\mathcal{H}_\infty^{\pi,\sigma}$ is the time dependent part of Hamiltonian operator[2]. When the time dependent field and the static holding field are parallel, and changing like $b(t) = b_{\|} \cos \nu t$, $\mathcal{H}_\infty^{\sigma}$ for hydrogen is:

$$\mathcal{H}_1^{\sigma} = i\hbar \begin{pmatrix} 0 & 0 & 0 & 0 \\ 0 & s\dot{s} + c\dot{c} & 0 & -s\dot{c} + c\dot{s} \\ 0 & 0 & 0 & 0 \\ 0 & s\dot{c} - c\dot{s} & 0 & s\dot{s} + c\dot{c} \end{pmatrix} = \frac{i\hbar\nu}{2} y_\sigma \sin \nu t \begin{pmatrix} 0 & 0 & 0 & 0 \\ 0 & 0 & 0 & \sin^2\theta \\ 0 & 0 & 0 & 0 \\ 0 & -\sin^2\theta & 0 & 0 \end{pmatrix} \tag{3.35}$$

and for deuterium is:

$$\mathcal{H}_1^{\sigma} = i\hbar \begin{pmatrix} 0 & 0 & 0 & 0 & 0 & 0 \\ 0 & s_+\dot{s}_+ + c_+\dot{c}_+ & 0 & 0 & 0 & -s_+\dot{c}_+ + c_+\dot{s}_+ \\ 0 & 0 & s_+\dot{s}_- + c_+\dot{c}_- & 0 & -s_-\dot{c}_- + c_-\dot{s}_- & 0 \\ 0 & 0 & 0 & 0 & 0 & 0 \\ 0 & 0 & s_-\dot{c}_- - c_-\dot{s}_- & 0 & s_+\dot{s}_- + c_+\dot{c}_- & 0 \\ 0 & s_+\dot{c}_+ - c_+\dot{s}_+ & 0 & 0 & 0 & s_+\dot{s}_- + c_+\dot{c}_- \end{pmatrix} =$$

$$= \frac{3i\hbar\nu}{4\sqrt{2}} y_\sigma \sin \nu t \begin{pmatrix} 0 & 0 & 0 & 0 & 0 & 0 \\ 0 & 0 & 0 & 0 & 0 & \sin^2 2\theta \\ 0 & 0 & 0 & 0 & \sin^2 2\theta & 0 \\ 0 & 0 & 0 & 0 & 0 & 0 \\ 0 & 0 & -\sin^2 2\theta & 0 & 0 & 0 \\ 0 & -\sin^2 2\theta & 0 & 0 & 0 & 0 \end{pmatrix} \tag{3.36}$$

where $c = \cos\theta$, $s = \sin\theta$ for hydrogen and $c_\pm = \cos\theta_\pm$, $s_\pm = \sin\theta_\pm$ for deuterium respectively.

When the holding field and the time dependent field is perpendicular to each other and the later changes like $b(t) = b_\perp \cos \nu t$:

$$\mathcal{H}_1^{\pi} \simeq i\frac{E_{HFS}^H}{2} y_\pi \cos \nu t \begin{pmatrix} 0 & \sin\theta & 0 & -\cos\theta \\ \sin\theta & 0 & -\cos\theta & 0 \\ 0 & \cos\theta & 0 & -\sin\theta \\ \cos\theta & 0 & -\sin\theta & 0 \end{pmatrix} \tag{3.37}$$

[2] Refer equation (3.26) for hydrogen

for hydrogen and

$$\mathcal{H}_1^{\pi} = i\frac{E_{HFS}^2}{2} y_\pi \cos\nu t \begin{pmatrix} 0 & -s_+ & 0 & 0 & 0 & -c_- \\ s_+ & 0 & -s_-c_+ & 0 & -c_-c_+ & 0 \\ 0 & s_-c_+ & 0 & -c_- & 0 & -s_-s_+ \\ 0 & 0 & c_- & 0 & -s_- & 0 \\ 0 & c_-c_+ & 0 & s_- & 0 & -s_+c_- \\ c_+ & 0 & s_-s_+ & 0 & s_+c_- & 0 \end{pmatrix} \tag{3.38}$$

for deuterium.

The θ and $\theta_\pm$ are the functions of x and $x = \frac{B}{B_C}$, So the V_{ab} in equation (3.33) is the function of B. The function $f(\nu - \nu_{ab}, \tau)$ is given by:

$$f(\nu - \nu_{ab}, \tau) = 4\frac{\sin^2 \frac{(\nu-\nu_{ab})\tau}{2}}{(\nu - \nu_{ab})^2} \tag{3.39}$$

A plot of this function is shown in figure 3.8.

In the resonance condition, the function turns into:

$$\lim_{\nu\to\nu_{ab}} f(\nu - \nu_{ab}, \tau) = \tau^2 \tag{3.40}$$

Then the transition probability becomes

$$W_{ab} \simeq \nu_{HFS}^2 y_{\pi,\sigma}^2 |V_{ab}|^2 \tau^2 \tag{3.41}$$

Considering the relations $\nu_{HFS} = \frac{E_{HFS}}{\hbar}$, $y_{\pi,\sigma} = \frac{b_{x,y}}{B_C}$ (where $b_{x,y}$ represents the amplitude of the oscillating field) and $B_C = \frac{E_{HFS}}{g_S\mu_B}$, the (3.41) can be written as the following:

$$W_{ab} \simeq \left(\frac{\mu_B}{\hbar}\right) b_{x,y}^2 |V_{ab}|^2 g_S^2\, \tau^2 \tag{3.42}$$

According to equation (3.42), while a static holding magnetic field supplies an axis of spin, the transition probability between two states $|\,a\,\rangle$ and $|\,b\,\rangle$ in resonance condition with the presence of a time dependent oscillating magnetic field depends on:

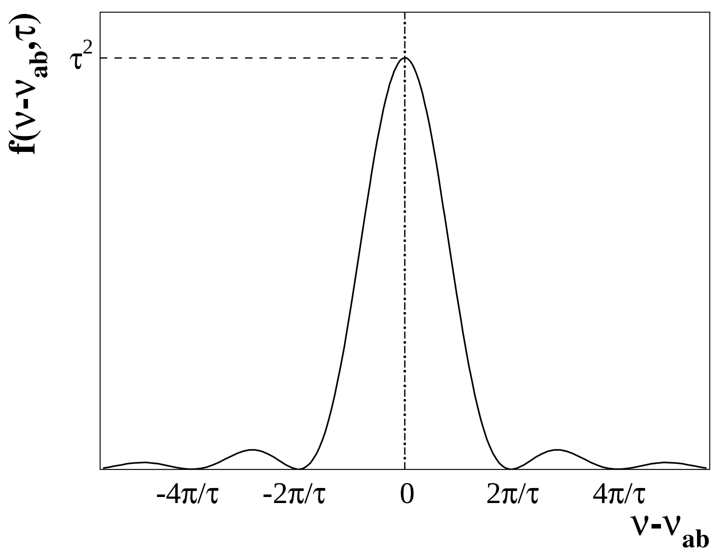

Figure 3.8:
$f(\nu - \nu_{ab}, \tau)$ at fixed τ as a function of $\nu - \nu_{ab}$.

1. The amplitude of time dependent magnetic field;

2. The strength of the holding magnetic field;

3. The time τ

The relationships between the relative probabilities for various transitions and the strength of the holding field are shown in figure 3.9.

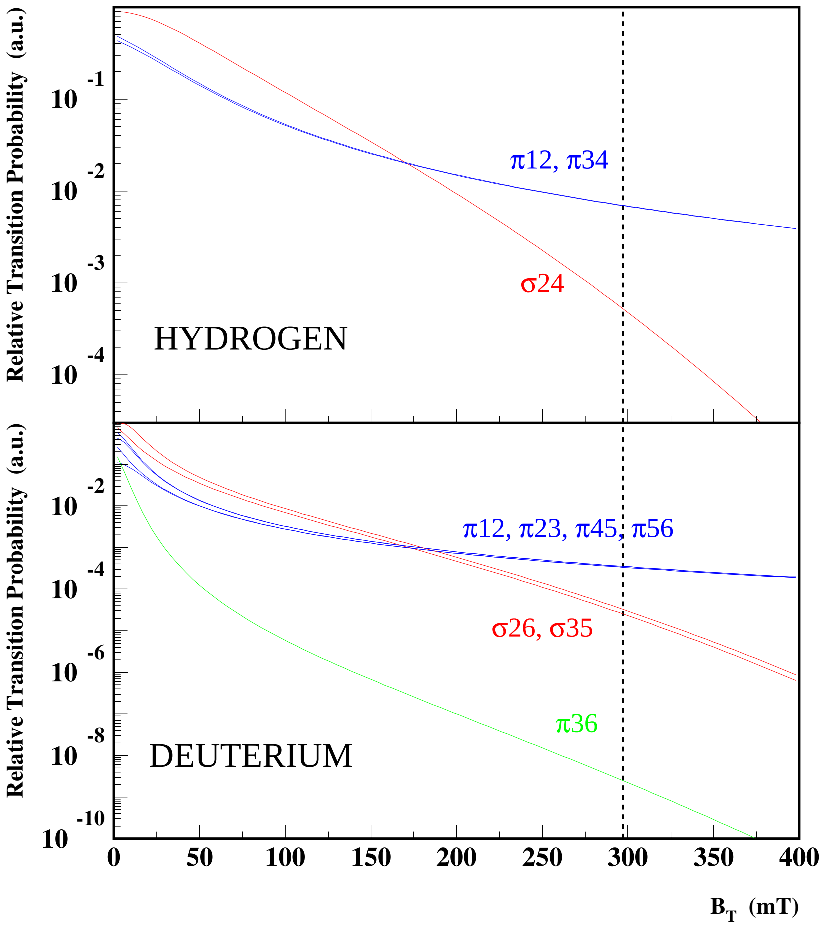

Figure 3.9: Relative probabilities of the nuclear depolarization resonance. At the working point of the HERMES transversely polarized target (dashed line), the σ resonance is by roughly one order of magnitude less probable than the π resonance transition for hydrogen. The probability of the $\pi\,|\,3\,\rangle \leftrightarrow |\,6\,\rangle$ is strongly suppressed with respect to all other transitions for deuterium[Dav02].

To keep the higher polarization of the transverse target, we must try to avoid the holding field meeting the resonance condition. The figure 3.7 and 3.9 can give us the instructions to design or improve the holding magnetic field characteristics:

1. From the figure 3.9 we notice, that to make the transition probability lower, the magnetic flux density should be strong, and the stronger the better for the target polarization. But extreme strong field will make the HERA positron beam diverted too much.

2. The field should be set as far as possible from the resonance points and must be stable.

3. As shown in figure 3.7, the difference between two consecutive resonance points of σ_{24} for hydrogen and deuterium is 0.37 mT around the working point. The uniformity of the magnetic field better than that at the region of the storage cell is demanded for avoiding the σ_{24} resonance transition.

3.4 Improvement in the Uniformity of the Holding Field

Although the probability of σ_{24} resonance transition is much lower than the π_{12} and π_{34} for hydrogen, because the two resonance points are around 0.37 mT in working region, the σ_{24} resonance transition will happen very easily if the holding field is not uniform enough. Due to the direction of the magnetic field is in vertical, only the y component[3], B_y, of the magnetic field is interested.

For making sure that our target magnet is matching the requirement, we have measured the field distribution with a hall probe in April during the HERA long shutdown period of 2003. According to the results, two improvements have been made about the uniformity of the magnetic field:

3.4.1 Improvement of the Uniformity of Magnetic Field along HERA Beam Direction

To make the field more uniform along the HERA beam direction, several shims, which are made of ferromagnetic materials and can change the magnetic field distribution, on the bottom pole tip of the magnet are added, refer to figure 3.15.

After adding the shims, the non-uniformity of the magnetic filed in y direction (vertical direction) changed as $\Delta B_y = 0.5\,Gs$ from the initial value $\geq 9.0\,Gs$[4]. Distributions of B_y along z direction after adding the first and tenth shim are shown in figure 3.10, while a distribution of B_y along x axis after finished shimming is shown in figure 3.11.

3.4.2 Improvement of the Uniformity of the Magnetic Field Along the Direction Perpendicular to the Beam Direction and in the Horizontal Plane

To improve the uniformity of the magnetic field, correction coils are added along the storage cell, see figure 3.12.

The cell-coils are made of copper with cross section $0.63 \times 0.1\ cm^2$ and have total two layers. Because the heads of cell-coils are inside the acceptance of the HERMES spectrometer, the size of the coils cannot be too thick, or more events will be lost, especially for Λ events which have very short lifetime.

[3] coordination definition: z is the direction along the HERA beam; y is in vertical direction and x is horizontal in a right hand coordinate system.

[4] The non-uniformity, ΔB_y, defined as the maximum difference among the y-components of the magnetic flux density in the measured spacial zone.

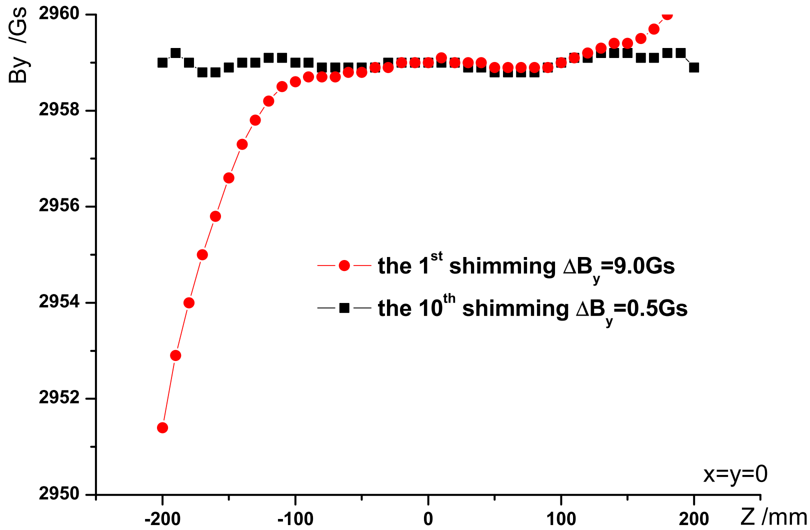

Figure 3.10: Measured B_y distribution along the HERA beam direction z over the storage cell length. One measurement is performed after each shimming until the $\Delta B_y \approx 0.5\,Gs$ after the ten times shimming..

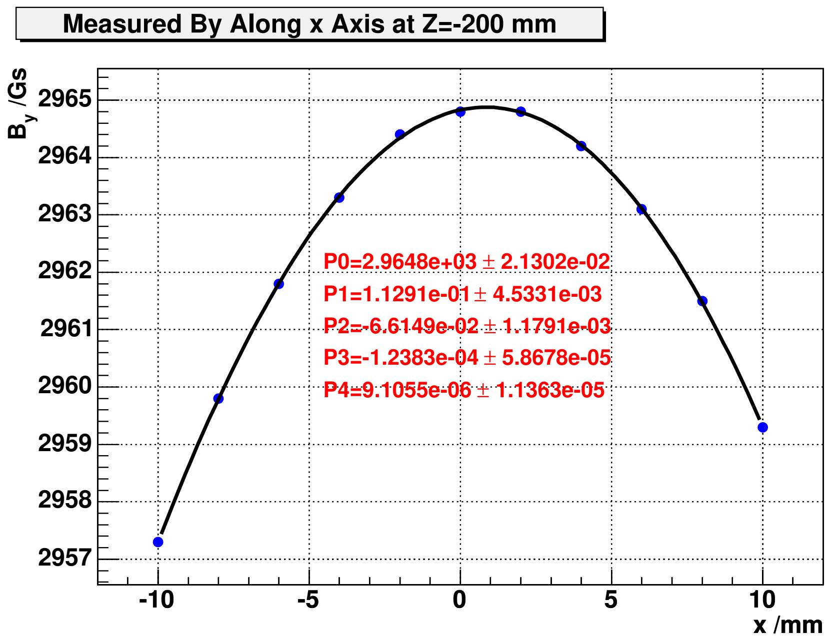

Figure 3.11: Measured B_y distribution along x axis, which is perpendicular to the HERA beam in horizontal direction.

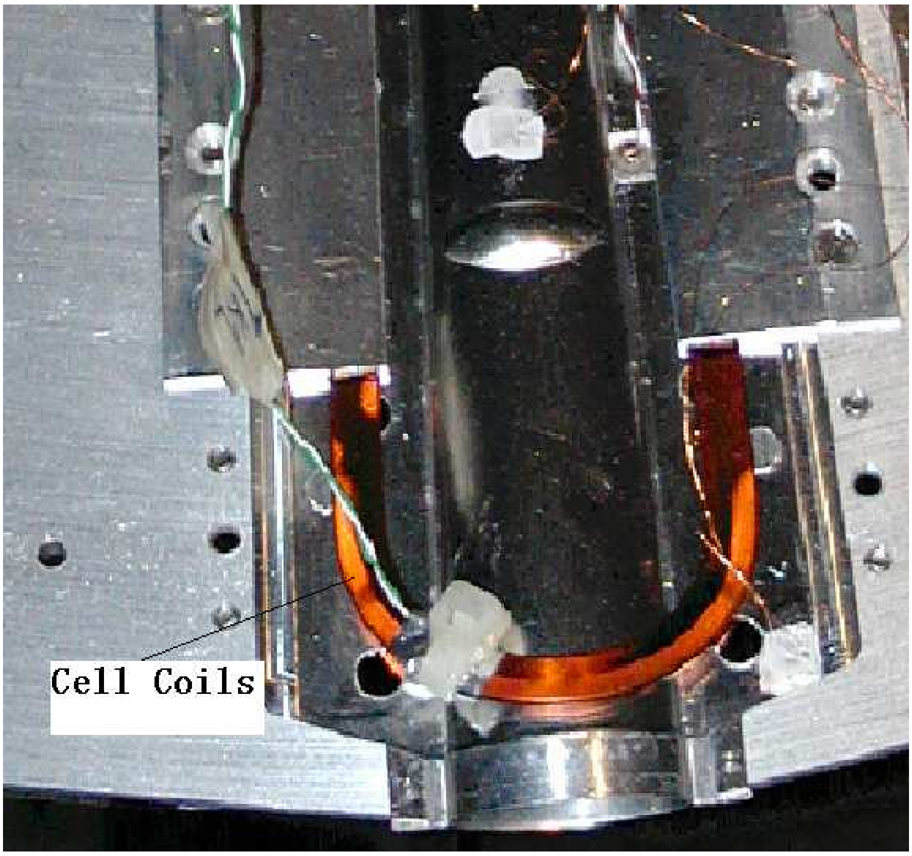

Figure 3.12: A photo about the correction coils beside the storage cell of the HERMES transverse target.

After installing the cell-coils, we faced a question about which current we should apply. Due to the spacial limitation inside the storage cell, it is impossible to measure the magnetic field.

With the measured B_y distribution along x direction without cell-coils, marked as B_y^{MEAS}, after using MAFIA[5] to simulate the B_y^{MAFIA} distribution with different current inside the cell-coils, a $B_y^{MAFIA} + B_y^{MEAS}$ distribution can be obtained by adding the B_y^{MAFIA} and the measured B_y^{MEAS} together. Four plots about $B_y^{MAFIA+MEAS}$ distributions along x-axis (along the direction perpendicular to the beam direction and in the horizontal plane) with $I_{cellcoils}$ = 40, 60, 80, 100 are shown in figure 3.13.

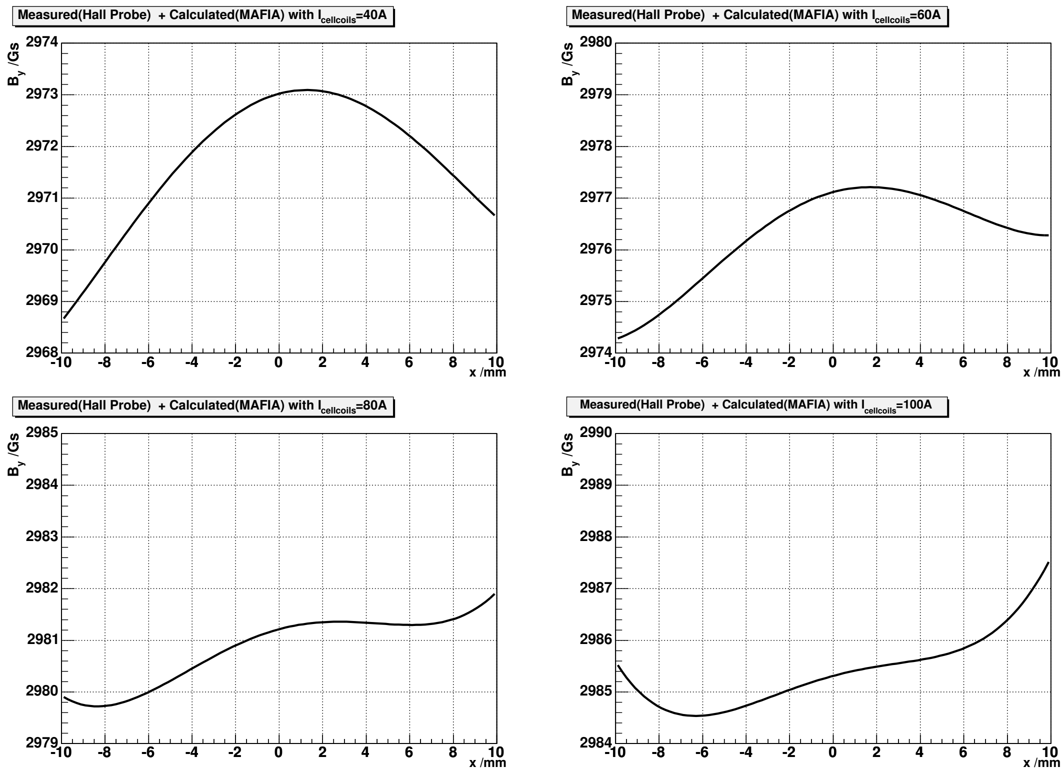

Figure 3.13: The $B_y^{MEAS} + B_y^{MAFIA}$ distributions along x-axis with different current values inside the cell-coils. The measured B_y^{MEAS} values were obtained during the shutdown time in 2003. The B_y^{MAFIA} values are the calculated values with MAFIA.

It can be easily got from the figure 3.13 that the uniformity would be improved if the $I_{cellcoils}$ is slightly greater than 60 A. The problem is technological: Increasing the current will increase the heating by Joule effect, which would cause an increase in the cell temperature. Because the cell-coils and the relative cooling system are designed for a maximum current of 60 A, we set the $I_{cellcoils}$ value as 60 A according to the calculation. The non-uniformity along x axis is around 0.3 mT with 60 A in cell-coils, see the top-right plot in figure 3.13.

[5]See section 5.2 in chapter 5

3.5 Improvement in Stability of the Holding Field

If the holding magnetic field is changing and can not be set at a fixed value, the beam induced depolarization will happen even equipped with the cell-coils.

3.5.1 Variation of Magnetic Field with Time

Two coils produce the magnetic field of the HERMES transverse polarized target. During normal operation, the current in the coils is $545A$, which corresponds to a magnetic field of 297 mT in the region of the target cell.

In May of 2003, the magnetic flux density B decreasing over the time after the coils were switched on was noticed while measuring the uniformity of the field. One measurement shows the magnetic value can decrease more than 0.4 mT within 8 hours (See figure 3.14).

Considering the current in the coils is constant during the measurement, the continually decreasing of the B should be due to the increasing temperature of the main yoke, pole and pole tips within several hours after the coils were switched on. The thermal motion of the atoms inside the yoke, pole and tips will partly destroy the regulation of the same direction align of magnetic domains, which affect the magnetic field strength. Because the distance from yoke to the coils is longer than that from the pole to the coils and the volume of the iron in yoke is much larger than that of the pole, the increasing speed of temperature of the yoke will be slower comparing with that of the pole. That is the reason why the field is decreasing quickly at the first half an hour (the pole plays the main role) and then decreasing slowly after the temperature of the pole is roughly stable while the yoke's temperature is continually increasing (observations show the temperature increasing will last more than 10 hours).

Because the distance between resonance transitions of σ_{24} as 0.37 mT around the working condition of the target, and the non-uniformity along beam direction around 0.05 mT and along x direction about 0.3 mT, the stability of the holding field has to be improved to avoid the beam induced depolarization.

3.5.2 Method to Stabilize the Strong Magnetic Field

In order to compensate the decrease of the magnetic flux density B with time, a pair of correction coils have been added to the main coils, as shown in figure 3.15.

A DTM-141 Digital teslameter[6] is used to monitor the magnetic flux density B_r inside the chamber near the storage cell. The difference between the measured flux density B_r and the desired magnetic flux density B_{set} is then calculated, and the current in the correction coils is adjusted to maintain the B_r around the B_{set}.

Two codes are used to automatically compensate the system: an interface code and a client. The interface code, named as "Jokecoil"[7], is written with PinK, which is an interface to access

[6] Group3 Technology Ltd., P. O. Box 71-111 Rosebank, Auckland 7, New Zealand

[7] At the very beginning, it was said that to add this correction coil is a joke. Now, we can confidently say: The

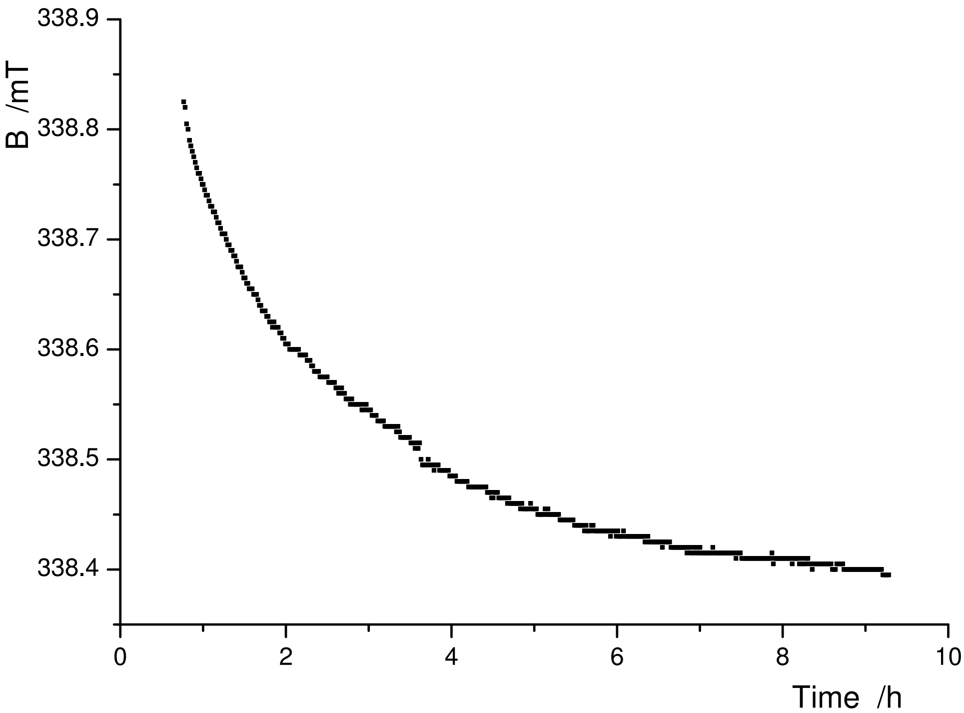

Figure 3.14: The magnetic flux density at a fixed point inside the HERMES transverse target chamber is changing with time.

ADAMO[8] and DAD[9] from X11 script language Tcl/TK. It sends the control parameters and receives the value for display from a client code, which reads the value of B_r, calculates the correction voltage value and sends the digital signal to DAC[10]. Then the voltage of DAC output changes the current in correction coils by controlling their current.

To test the validity of the automatic compensating system, the following tests have been performed:

Response Characteristics Test

As shown in figure 3.16, we change the B_{set} at different points: 338.900, 339.000, 339.200, 339.400 and 339.200[11] mT. The output of DAC and B_r changes corresponding to the B_{set}. The output range of DAC from 0 to 10 V, corresponds to a current in correction coils from 0 to 10 A,

"Jokecoil" is not a joke! That is the right reason the name was given according to Chinese tradition with best wishes.

[8]ADAMO, originally developed for the ALEPH experiment at LEP, supports an experiment-wide strategy for data design and organization. it uses a form of the Entity-Relationship model and allows data to be represented as a diagram.

[9]DAD (Distributed Adamo Database) is an extension to Adamo. Dad's main purpose is to make Adamo data available between different processes and different machines on the network. It's data exchange format can however be used to write and read from sequential files at a much higher i/o rate than the generic Adamo ZEBRA i/o drivers.

[10]Model 3112-M1A 8-channel, 12-bit D/A Converter.

[11]There is a short distance between the hall probe measuring B_r and the target storage cell, where the value is around 297 mT.

Figure 3.15: Main coils and correction coils in the transverse target of HERMES

and produces a compensation field ΔB $0 \sim 0.7$ mT. When the output of DAC reaches its limit values $0V$ or $10\,V$, the control system sends out warning message and the main coils' current needs to be manually adjusted to recover the control ability.

Stability Test

A stability test has been performed by keeping the current in the main coils at $545A$ and setting $B_{set} = 338.600$ mT. The automatic compensation system has been then switched on to fix the magnetic flux density value around B_{set}. B_r and output of DAC are given in figure 3.17, the mean of B_r is 338.600 ± 0.004 mT. For the long term running from January to June of 2004, average value of the difference between the B_r and B_{set} is -0.0005 ± 0.0009 mT for 27588 measurements, see the histogram in figure 3.18.

3.5.3 Accuracy of the Magnetic Field with Compensation System

The systematic error is determined by the precision in the measurement of the magnetic flux density. According to the manual[Grp3] of MPT-141 with DTM-141 teslameter, the systematic

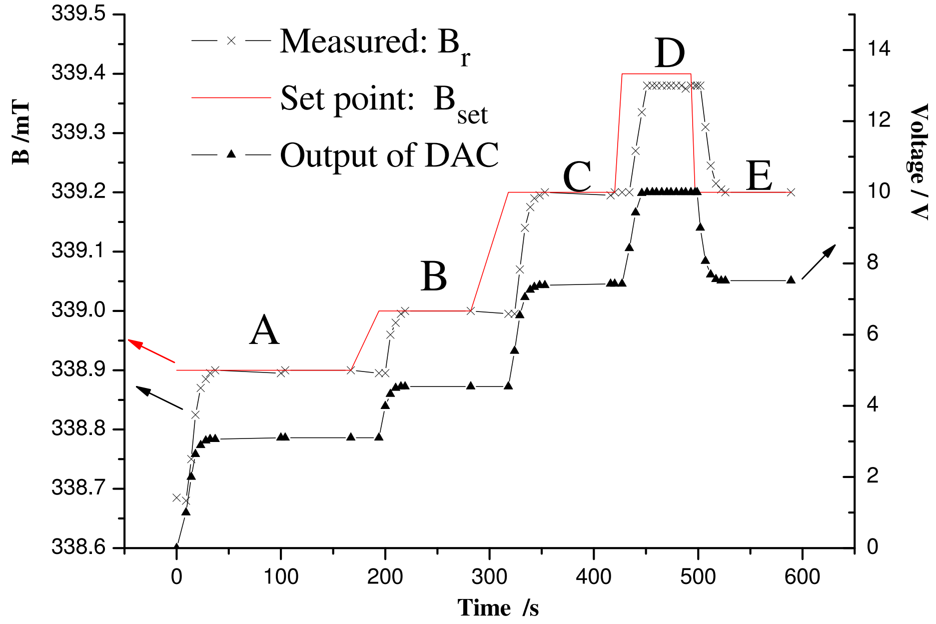

Figure 3.16: Set B_{set} at different values to test the response characteristics of the automatic compensation system.

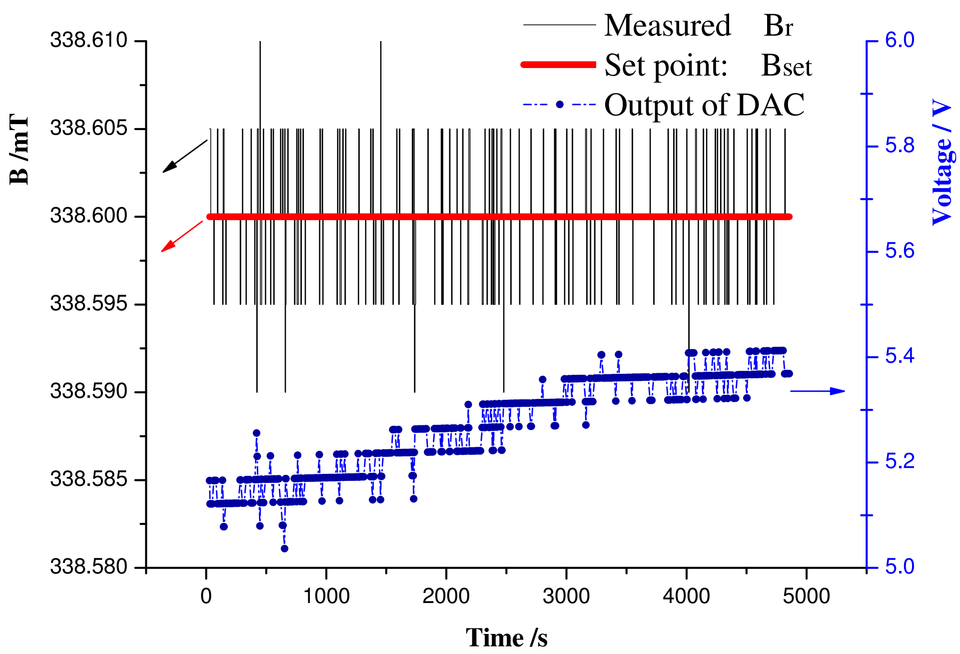

Figure 3.17: The performance of the automatic compensation system. $1V$ output of DAC vs. $1A$ in the correction coils.

errors mainly come from two sources: the thermal drift of the Hall probe and the temperature effects on the cable. The temperature variation inside the chamber near the Hall probe is less than 5^oC, which implies an error from the Hall probe $\Delta B_1 \leq 0.017$ mT. The temperature in

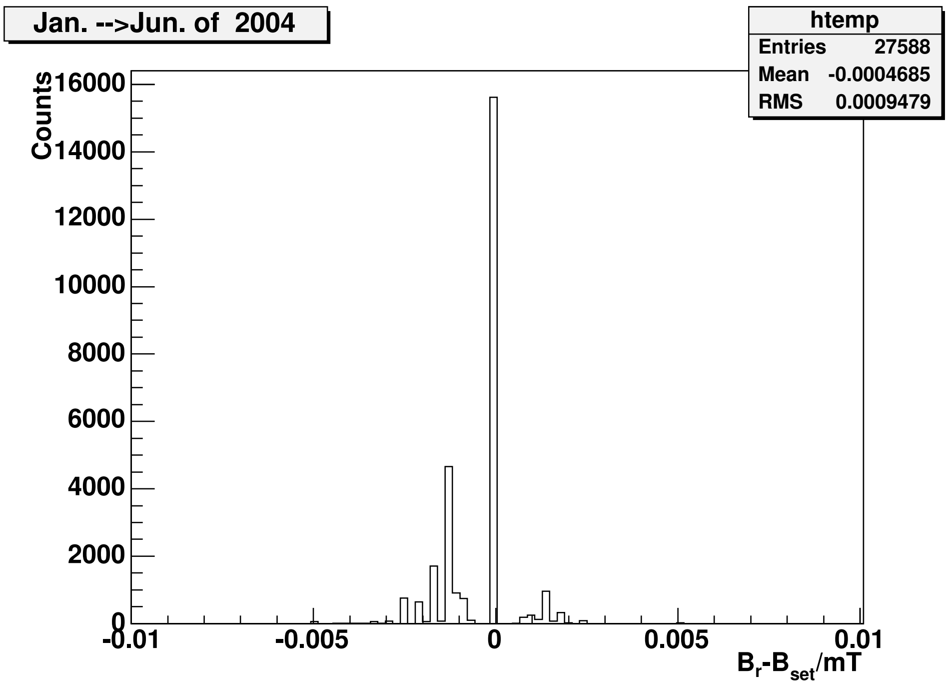

Figure 3.18: The difference values between B_r and B_{set} from January to June of 2004

our experiment Hall is kept nearly constant with the air conditioners although the cable is 20 m long. For a variation of the air temperature of 1^oC, we get a contribution from the cable of 0.041 mT. The maximum zero point drift with the temperature is $\pm(0.001mT + 0.0003\% \times B_{full})/^oC$. Where the B_{full} is the full-scale and equals 600 mT in the system. Then the zero point drift error is 0.003 mT. So the systematic error is $\sqrt{0.017^2 + 0.041^2 + 0.003^2} \approx 0.045$ mT. The total error is $\pm 0.004(Stat.) \pm 0.045(Syst.)$ mT, matching the requirement to avoid depolarizing resonance induced by the HERA beam.

3.5.4 Depolarization Scan for B_{set} Value Optimization

After establishing the automatic system, the next step is to search for the best set point, B_{set}, of the holding magnetic field.

There is an old saying: "The horse and mule can be distinguished after letting them walk". Based on this idea, we add a special function of the compensation system for automatically scan: The system changes the B_{set} from higher to lower while measuring the Pz^+ and Pz^- with BRP. The figure 3.19 shows the performance of the "Jokecoil" during the depolarization scanning. The results for the Pz^+ and Pz^- changing with the strength of the holding field are shown in figure 3.20. The B_{set} can be determined very easily from the figure.

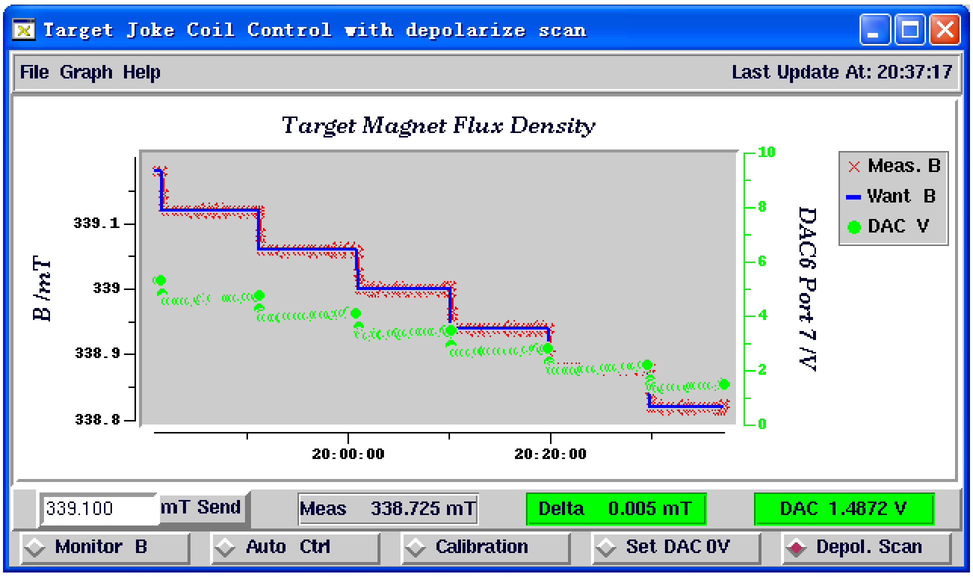

Figure 3.19: The interface of Jokecoil. "Monitor B" for measuring the magnetic field without changing the current in correction coils; "Auto Ctrl" for maintaining the magnetic field at a fixed input value in the editor above the "Monitor B" button; "Calibration" for measuring the magnetic field changing with the current in correction coils; "Set DAC 0V" for resetting the current in the correction coils to zero; "Depol. Scan" button for changing the magnet cooperating with BRP to get the best setting point of the magnet.

3.6 Evaluation of the Cell-coils and the "Jokecoil" System

The effect of "Cell-coil" can be evaluated by two depolarization scans: With 60 A current or without current in it. Due to different intensity of the HERA beam will lead to different amplitudes of depolarization, this influence has to be corrected before comparing the polarization degree with or without current in "Cell-coils". The relationships between HERA beam intensity and Pz^+, Pz^- are shown in figure 3.21. The contribution to the polarization degree from the "Cell-coils" is around 1% for the normal running.

As shown in figure 3.18, the strength of the target magnetic field can be stabilized on any value with the "Jokecoil" system. Its contribution to the polarization of the internal gas target can be demonstrated from one miss-operation: During one fill of the positron beam, the "Auto ctrl" button, which was for sending out command to automatically keep the field around the set value, wasn't pushed and let the "Jokecoil" system working in the "Monitor B" mode, which made the system only measuring the strength of the field, after the magnet was switched on. Since the strength of the holding field kept decreasing, see the bottom right plot in figure 3.22, the Pz^+ (the top left plot in figure 3.22) and Pz^- (the top right plot in figure 3.22) change with the variations of the probability of beam induced depolarization under different strength of external holding magnetic field. The resonance peaks could have been avoided if the "Jokecoil" system had been working in "Auto ctrl" mode.

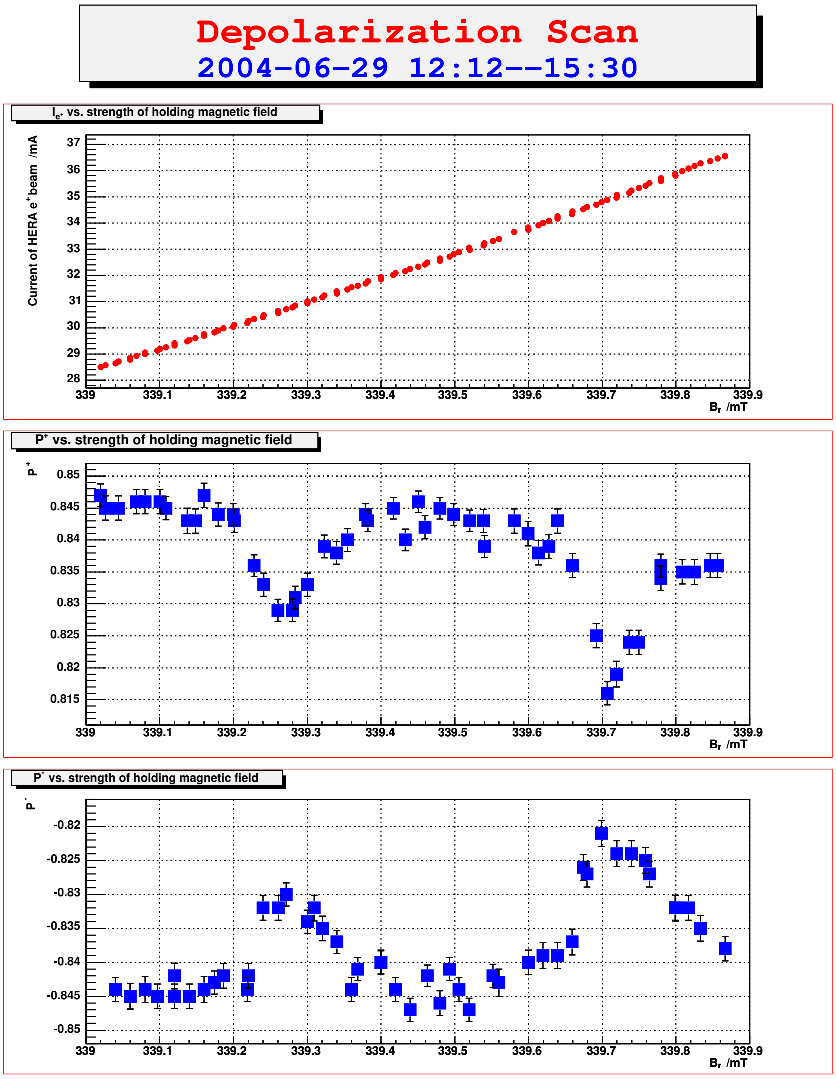

Figure 3.20: Depolarization scan with 60 A current in cell-coils. The HERA beam current keeps decreasing step by step during the scanning. The magnetic field was changing from higher to lower. The HERA beam current corresponding to the measured field with a Hall Probe is shown in the top plot. The Pz^+ (in middle plot) corresponding to the hyperfine states $|1\rangle$ and $|4\rangle$ while the Pz^- (in the bottom plot) for the hydrogen atoms in $|2\rangle$ and $|3\rangle$ states. The step length of the magnetic field for the scan is 0.06 mT.

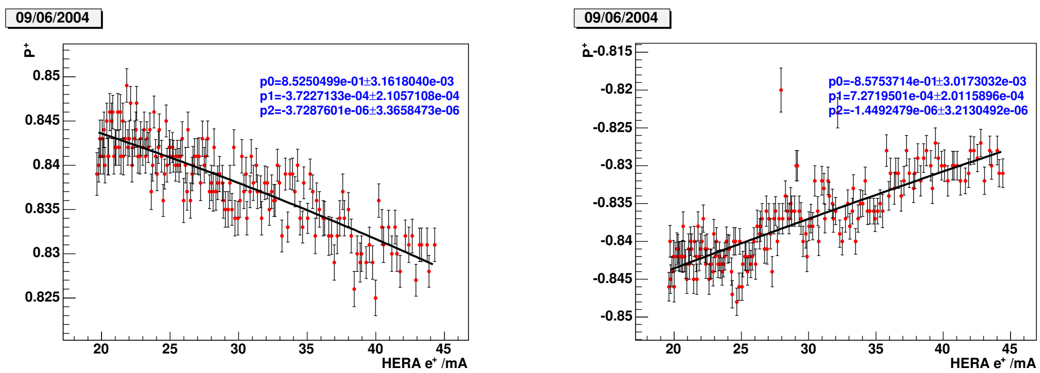

Figure 3.21: Pz^+(left) and Pz^- (right) change with the intensity of HERA e^+ beam. The holding magnetic field is fixed and the current in the cell-coils is 60A.

Since October of 2003, the intensity of HERA beam has been getting higher and higher, see figure 3.24, the role of the "Jokecoil" system has been getting more and more important. One beam induced depolarization resonance peak with amplitude of 3% has ever been measured with a "Jokecoil" depolarization scan, see figure 3.25, without current in cell-coils.

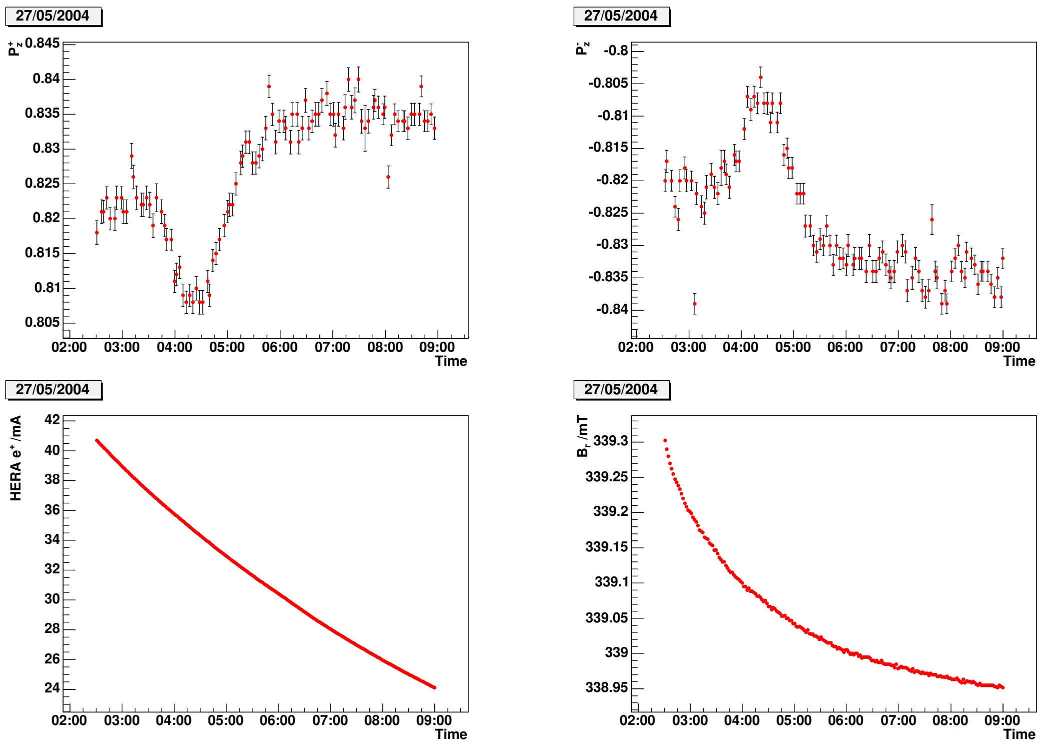

Figure 3.22: Pz^+ (top left plot) and Pz^- (top right plot) change with time due to the decrease of the HERA beam current (bottom left plot) and the strength of magnetic field (bottom right plot) without the compensation of "Jokecoil" system.

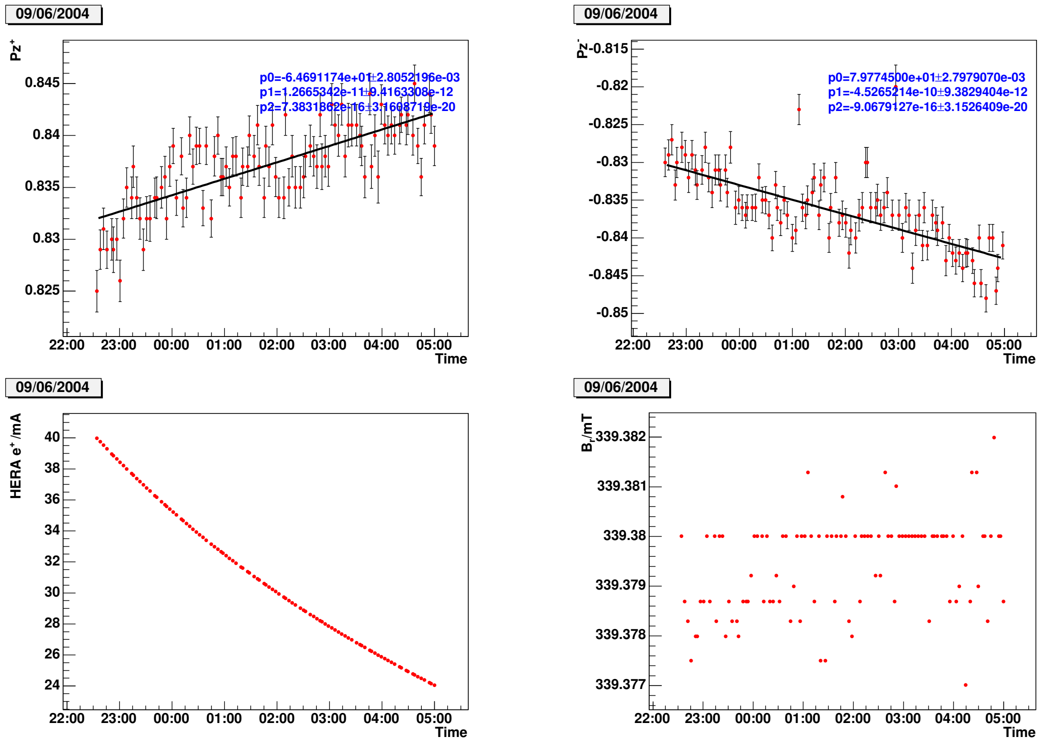

Figure 3.23: Pz^+ (top left plot) and Pz^- (top right plot) change with time due to the decrease of the HERA beam current (bottom left plot). The strength of magnetic field(bottom right plot) is automatically fixed with the compensation of "Jokecoil" system.

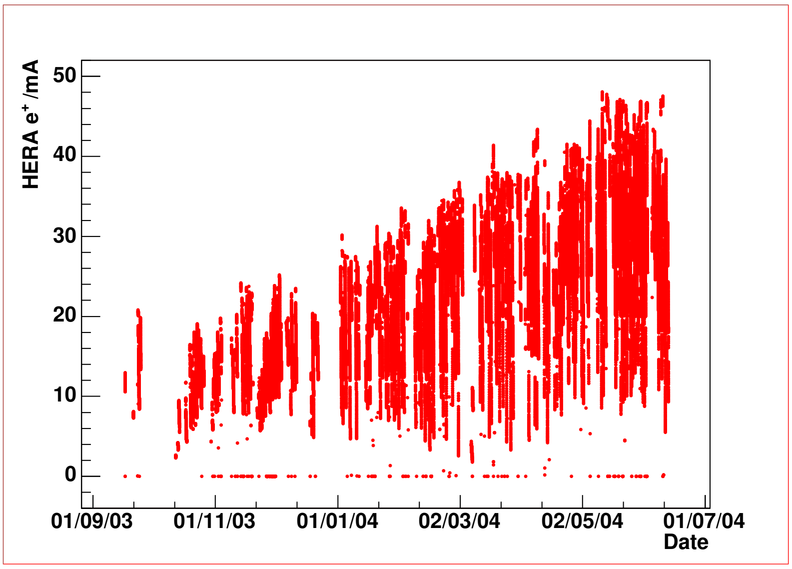

Figure 3.24: The intensity of HERA positron beam from Oct., 2003 to Jul., 2004.

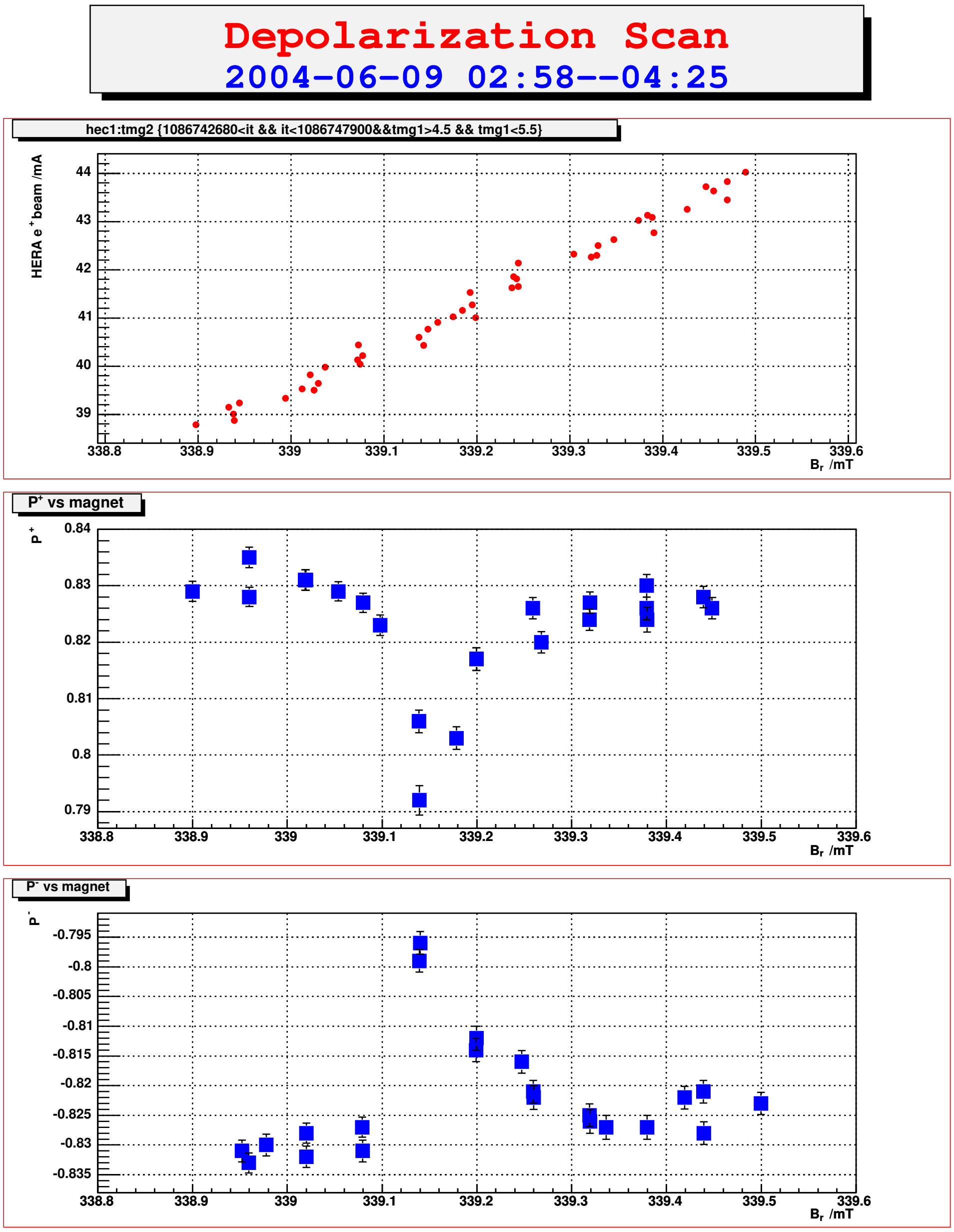

Figure 3.25: Depolarization scan without current in cell-coils. The amplitudes of beam induced depolarization peaks are around 3% when the beam intensity is around 41 mA.

Chapter 4

Improvement in Target Calibrations

This chapter describes two new methods about how to directly measure G(T) function, which describes the temperature dependence of the counting rates of TGA.

4.1 Introduction

As mentioned before, The TGA consists of a chopper, two baffles and a quadrupole mass spectrometer (QMS) with a cross beam ionizer. A channeltron is used for detecting the ionized atoms and molecules. As for the target storage cell, there are three tubes connected with it: an injection tube (IT) from ABS to the cell, a sample tube (ST) for sampling the gas from the storage cell to perform analysis work while the target running and a feed line of unpolarized gas feed system for the injection of unpolarized gas to the cell in some unpolarized physics experiments. An extension tube (ET) is installed just behind the sample tube to conduct gas into the TGA chamber. Figure 4.1 shows the relative geometries and size of those tubes.

After atoms or molecules are injected into the storage cell, they will diffuse out through the open end of the target cell, the injection tube, sample tube and extension tube. The

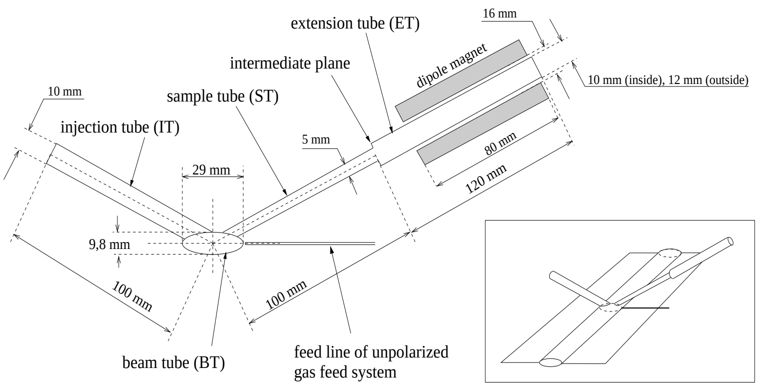

Figure 4.1: Schematic plots of the storage cell and it tubes. The main figure shows the details of the elliptical cross section and the side tubes with their dimensions while the inlay on the right side gives a 3-dimensional plot for the cell.

conductance for gas freely diffusing inside these tubes will be changed once the temperature of the tubes changes. So the count rates of the TGA for atoms and molecules are affected by the temperature variation.

4.2 κ calibration of TGA

The relative sensitivity of the TGA for the atomic and molecular beam is defined by a constant:

$$\kappa = \frac{\sigma_a^{ion} \cdot \varepsilon_a}{\sigma_m^{ion} \cdot \varepsilon_m} \tag{4.1}$$

where the $\sigma_{a,m}^{ion}$ is the ionization cross section and $\varepsilon_{a,m}^{ion}$ is the efficiency. κ calibration is to measure this value with a method called temperature scan. The effect of temperature on the conductance has to be taken into account during temperature scanning for κ calibration.

The TGA signal of S_a, for atoms, and S_m, for molecules, are proportional to the atomic and molecular flow rates, $\Phi_{a,m}^{TGA}$, into TGA. The amplitudes of $S_{a,m}$ signals can be affected by ionization cross section $\sigma_{a,m}^{ion}$ and the detection efficiency $\varepsilon_{a,m}^{ion}$. The $\varepsilon_{a,m}^{ion}$ includes the transmission probabilities of the ions through the quadrupole mass spectrometer (QMS) and detection efficiency by the channeltron of TGA. Magnetic fringe fields in the target region, caused by the target magnet and HERMES spectrometer magnet, have an influence on the trajectories of the ions inside the cross beam ionizer and the mass spectrometer, so that the detection efficiency and the absolute count rates of the TGA depend on the magnetic fields. During calibration measurements and HERMES data taking periods, the strength of the fields of these magnets was kept constant. The influence on TGA from the fields can be treated as a constant. Because the ionization probability in the cross beam ionizer is proportional to the time τ, that the atoms or molecules need to pass through the ionization volume, the signals are proportional to the particles mean inverse velocity $\langle \frac{1}{v_{a,m}} \rangle$. The emission current I_{emis} of the electron gun of the cross beam ionizer can affect the amplitudes either. One thing that should be mentioned is: that although as space charges in the electron gun can lead to a change in the trajectories of the ionizing electrons and to a change in the ionization efficiency, measurements of the TGA count rates as a function of the emission current show that the signals can be taken as a linear function of I_{emis} (see the figure 2.12 in chapter 2).

$$S_{a,m} \propto \Phi_{a,m}^{TGA} \cdot \sigma_{a,m}^{ion} \cdot \varepsilon_{a,m}^{ion} \cdot \langle \frac{1}{v_{a,m}} \rangle \cdot f_{a,m}(B, I_{emis}) \tag{4.2}$$

$f_{a,m}(B, I_{emis})$ for the effect from I_{emis} and the magnetic field and can be obtained by scanning the TGA emission current while monitoring the TGA signal, $S_{a,m}$. Due to the mean velocity of gas is related with the gas temperature, which is nearly equal to the temperature of the extension tube, $T_{a,m} \approx T_{ET}$, for the gas into the ionization volume of TGA, with the Maxwell-Boltzmann distribution equation, we have:

$$\langle v_{a,m} \rangle = \sqrt{\frac{8kT_{a,m}}{\pi M_{a,m}}} \approx \sqrt{\frac{8kT_{ET}}{\pi M_{a,m}}} \tag{4.3}$$

where k is Boltzmann constant, $T_{a,m}$ is the temperature of the atomic or molecular gas, T_{ET} is the temperature of the extension tube and $M_{a,m}$ is the mass of atoms or molecules. Then we can re-write equation (4.3) as

$$S_{a,m} \propto \Phi^{TGA}_{a,m} \cdot \sigma^{ion}_{a,m} \cdot \varepsilon^{ion}_{a,m} \cdot \frac{\sqrt{M_{a,m}}}{\sqrt{T_{ET}}} \cdot f_{a,m}(B, I_{emis}) \tag{4.4}$$

Introducing C^{xx} as conductance for the tubes (the sample Tube is labelled as ST instead of xx, Extension Tube as ET, Storage cell or Beam Tube as BT and Injection Tube as IT), we can obtain the total number of atoms injected into the TGA for hydrogen, $\Phi^{TGA} = \Phi^{TGA}_a + 2\Phi^{TGA}_m$, is proportional to the flux, Φ^{ABS}, injected into the target cell from ABS and can be expressed as:

$$\Phi^{TGA} \propto \Phi^{ABS} \cdot \frac{C^{TGA}}{2C^{BT} + C^{IT} + C^{TGA}} \tag{4.5}$$

where the "2" before C^{BT} is for two open ends of the storage cell (beam tube) and C^{TGA} is the total conductance of the sample tube and extension tube and can be calculated as:

$$C^{TGA} = \frac{C^{ST}C^{ET}}{C^{ST} + C^{ET}} = \frac{C^{ST}}{1 + \frac{C^{ST}}{C^{ET}}} \tag{4.6}$$

If we express the conductance C^{xx} as $C^{xx} = \tilde{C}^{xx}\sqrt{\frac{T_{xx}}{M_{a,m}}}$ and assuming the tubes except for the extension tube, which is only connected by a thread to the storage cell frame, have the same temperature ($T_{BT} = T_{IT} = T_{ST} = T$), the equation (4.5) can be expressed as:

$$\begin{aligned} \Phi^{TGA} &\propto \Phi^{ABS} \cdot \frac{\tilde{C}^{ST}}{(2\tilde{C}^{BT} + \tilde{C}^{IT}) \cdot (1 + \frac{\tilde{C}^{ST}}{\tilde{C}^{ET}}\sqrt{\frac{T}{T_{ET}}}) + \tilde{C}^{ST}} \\ &= \Phi^{ABS} \cdot \frac{1}{1 + \frac{(2\tilde{C}^{BT} + \tilde{C}^{IT})}{\tilde{C}^{ST}} + \frac{(2\tilde{C}^{BT} + \tilde{C}^{IT})}{\tilde{C}^{ET}} \cdot \sqrt{\frac{T}{T_{ET}}}} \\ &\equiv \Phi^{ABS} \cdot \frac{1}{C_1 + C_2\sqrt{\frac{T}{T_{ET}}}} \end{aligned} \tag{4.7}$$

where C_1 and C_2 are constants. we definite $G(T)$ as:

$$G(T) \equiv \frac{1}{G_0}\frac{1}{C_1 + C_2\sqrt{\frac{T}{T_{ET}}}} \tag{4.8}$$

where G_0 is a normalized constant that makes $G(T_0)$ equals 1 when the temperature of the storage cell equals T^0 and the extension tube equals T^0_{ET}. Both the temperatures are selected as the general temperature when taking data, for example: $T_0 \equiv 100$ K as the cell temperature and $T^0_{ET} \equiv 130.4$ K as the extension tube temperature.

Then the equation (4.7) can be written as:

$$\Phi^{TGA} \propto \Phi^{ABS} \cdot G\,(T) \tag{4.9}$$

Keeping the total atom flux from ABS injecting into the target cell stable, the value $\frac{\Phi^{TGA}}{G(T)} = \frac{\Phi_a^{TGA}+2\Phi_m^{TGA}}{G(T)} \propto \Phi^{ABS}$ is a constant either during temperature scan, and is defined as:

$$\Phi_{Tot}^{CELL} \equiv \frac{\Phi_a^{TGA} + 2\Phi_m^{TGA}}{G(T)} \tag{4.10}$$

From equation (4.4) and equation (4.10), we can get:

$$\frac{\sqrt{T_{ET}}S_a}{G(T)f_a\left(B, I_{emis}\right)} \cdot \frac{1}{\sigma_a^{ion}\varepsilon_a^{ion}\sqrt{M_a}} + 2\frac{\sqrt{T_{ET}}S_m}{G(T)f_m\left(B, I_{emis}\right)} \cdot \frac{1}{\sigma_m^{ion}\varepsilon_m^{ion}\sqrt{M_m}} = C_{tot} \tag{4.11}$$

where C_{tot} is a constant. Considering $M_m \approx 2M_a$ and the definition of κ in equation (4.1), the (4.11) can be transformed as:

$$\frac{\sqrt{T_{ET}}S_a}{G(T)f_a\left(B, I_{emis}\right)} + \sqrt{2}\kappa\frac{\sqrt{T_{ET}}S_m}{G(T)f_m\left(B, I_{emis}\right)} = \sigma_a^{ion}\varepsilon_a^{ion}\sqrt{M_a}C_{tot} = C_{tot}^{'} \tag{4.12}$$

here, the detection efficiency $\varepsilon_{a,m}^{ion}$ and the ionization cross section $\sigma_{a,m}^{ion}$ are taken as constants in the general running of the calibration and HERMES data taking. The temperature of the extension tube is a measured value. $C_{tot}^{'}$ is a constant under the condition that the total atom flux injected into the target storage cell is stable.

The $f(B, I_{emis})$ can be measured by scan the emission current of the electron gun of the cross beam ionizer while measuring the atomic and molecular count-rates with TGA.

For the constants C_1 and C_2 in $G(T)$ function, we only have theoretical values calculated with the conductance of all the tubes by the equation[Bau00] before Sep. 2003:

$$C = \frac{16}{3\sqrt{2\pi}}\frac{S^2}{UL + \frac{16}{3}S}\sqrt{\frac{kT}{M_{a,m}}} \tag{4.13}$$

where S is the cross section area of an elliptical shaped tube of radius $a \times b$, and is given by $S = \pi ab$, and the circumference U of the elliptical tube can be approximately written as[Bro 79]:

$$U \simeq \pi[1.5(a+b) - \sqrt{ab}] \tag{4.14}$$

Experiments show that at different temperatures of the target cell, the probability of two atoms of hydrogen recombined into a molecule is different. One of the reasons is that the lower temperature will lead to higher density of the gas inside the cell and increasing the recombination probability. The other reason is that the physical characters of the surface will change the temperature and make the recombination probability on the surface changes. If keeping the injection flux of ABS stable, the κ value can be measured by variation of the cell temperature and fitting with equation (4.12).

As for the $G(T)$ function, it is very necessary to do some experiments measuring the coefficients C_1 and C_2 corresponding to the complicated geometry of the HERMES target.

After studying the structure of the HERMES target, two methods to directly measure C_1 and C_2, one with the Unpolarized Gas Feed System (UGFS) and the other with ABS, were proposed and performed.

4.3 New Method to Measure $G(T)$ with UGFS

The schematic plot of unpolarized gas feed system is shown in figure 4.2.

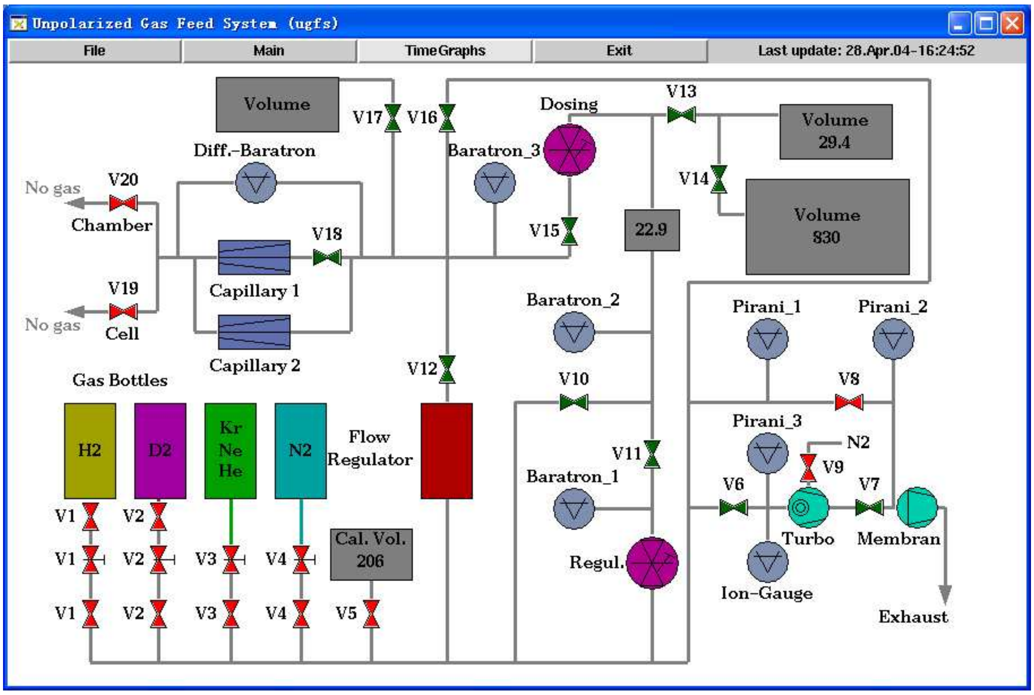

Figure 4.2: The schematic plot of UGFS. The injection flux can be adjusted by the "dosing" valve.

The flux of the gas is controlled by a "Dosing" valve and can be kept stable even the temperature of the target cell is changed. Because the pure H_2 doesn't recombine inside the target cell, the flux of molecules injected into the TGA chamber is determined by the opening size of "Dosing" valve at a fixed temperature.

The $G(T)$ function, which describes the influence of the temperature of the storage cell and the extension tube on the gas conductance of the tubes, can be obtained from TGA signals changing with the temperature if we keep a constant H_2 gas flow injected into the storage cell while changing the cell temperature. Before the temperature scan, the molecular flux, Φ^{UGFS}, injected into the storage cell should be adjusted to be the same as for the temperature scan with ABS injecting for κ calibration. In this case, the first term in the left of the equation (4.12) equals zero for pure H_2 gas injection with UGFS. The normalized relationship between $S_m^{corr} \equiv \frac{\sqrt{T_{ET}}S_m}{f_m(B,I_{emis})}$ and $\sqrt{\frac{T}{T_{ET}}}$ can be fitted with a function:

$$y\left(x\right) = \frac{1}{C_1 + C_2 x} \tag{4.15}$$

Then the $G(T)$ can be obtained from the fitting result. An example of the $G(T)$ calibration result with UGFS is shown in figure 4.3.

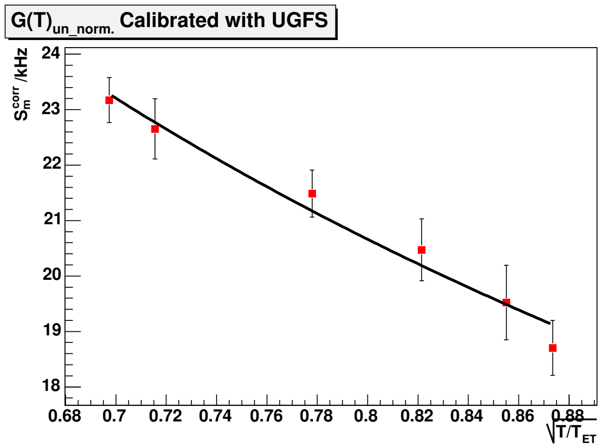

Figure 4.3: The experimental results of $G(T)_{un-norm.}$ function calibrated with UGFS (Sep. 26, 2003). $G(T)$ can be obtained by normalization.

4.4 New Method to Measure $G(T)$ with ABS

Another new method to measure $G(T)$ with ABS was proposed following the proposal about calibration with UGFS. The method with ABS can only be performed under certain condition: the coated Drifilm layer inside the surface of the storage cell is perfect, which means the molecular signal of TGA is far more less than that of atoms: $S_m \ll S_a$.

Under such condition, from the equation (4.12), a total TGA signal $S_{tot} \equiv S_a^{corr} + \sqrt{2}\kappa S_m^{corr} = \frac{\sqrt{T_{ET}}S_a}{f_a(B,I_{emis})} + \sqrt{2}\kappa_0 \frac{\sqrt{T_{ET}}S_m}{f_m(B,I_{emis})}$ is obtained after a initial value κ_0 is given for a temperature scan with ABS injection. The systematic error that introduced from the κ_0 is very small since $S_m \ll S_a$. A relationship between S_{tot} and $\sqrt{T/T_{ET}}$, which is $G(T)$, can be fitted with the equation 4.15.

One $G(T)$ calibration with ABS was performed. The ratio between the signal S_m and S_a is small and roughly constant during the temperature scan, see figure 4.4. The un-normalized $G(T)$ result is shown in figure 4.5.

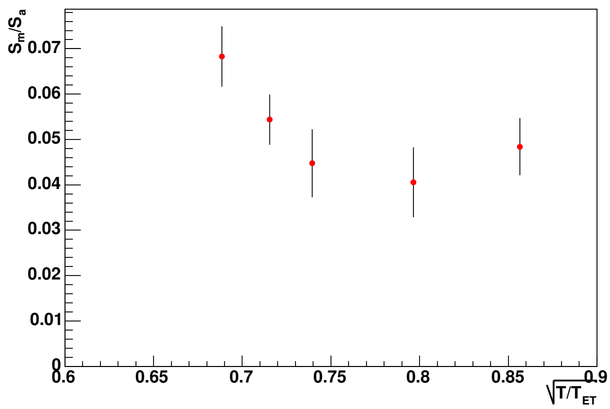

Figure 4.4: S_m/S_a changes with $\sqrt{T/T_{ET}}$ during calibrating $G(T)$ with ABS on Sep. 27, 2003. Perfect coated Drifilm layer inside the storage cell suppresses the variation of the recombination probability.

So far we have three $G(T)$ from theory, ABS and UGFS temperature scan methods. The $G(T)$ from theory is obtained from equation (3.14) of Christian Baumgarten's dissertation[Bau00].

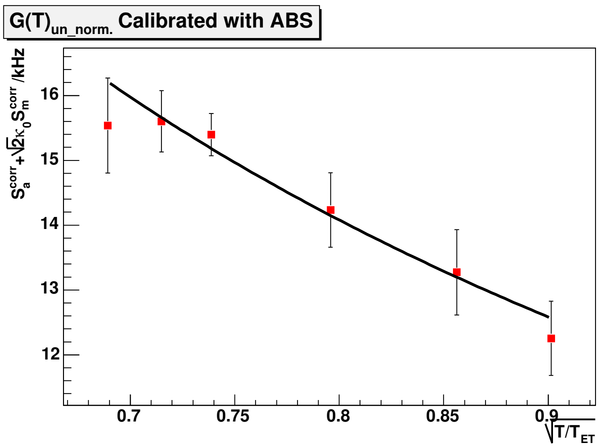

Figure 4.5: The experimental results of $G(T)_{un-norm.}$ function calibrated with ABS (Sep. 27, 2003). $G(T)$ can be obtained by normalization. $\kappa_0 = 0.55$ from the previous κ calibration result performed on Aug. 16, 1997[Bau00] in calculating the total signal.

The formulation is like:

$$G(T)_{theo} = \frac{1}{1+\frac{\tilde{C}^{ST}}{\tilde{C}^{ET}}\sqrt{\frac{T}{T_{ET}}}} = \frac{1}{1+\frac{0.076}{0.286}\sqrt{\frac{T}{T_{ET}}}} \tag{4.16}$$

where the $\tilde{C}^{ST} = 0.076$ is the conductance of the sample tube and $\tilde{C}^{ET} = 0.286$ is the conductance of the extension tube.

The theoretical and the experimental $G(T)_{norm}$, which are normalized $G(T)$ and defined as $G(T)_{norm} = \frac{G(T)}{G(0.7)}$, are shown in figure 4.6.

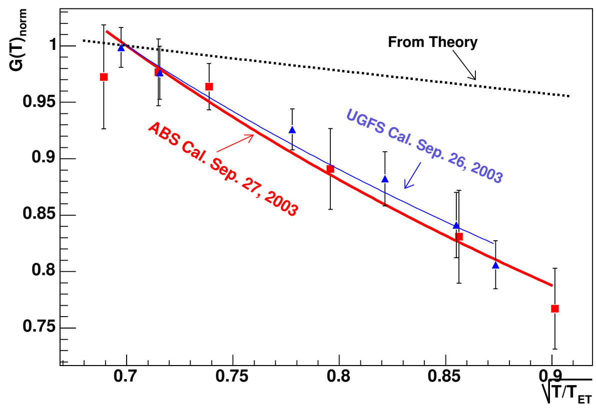

Figure 4.6: Normalized G(T) functions from theory, experiments with ABS and UGFS. The theoretical normalized G(T) is calculated from equation (4.16), The $G(T)$ from experiment with UGFS is calculated with the results shown in figure 4.3 and the another one from experiment with ABS is from the results in figure 4.5.

4.5 κ calibration results with different $G(T)$

One κ calibration was performed on Apr. 4, 2004 after the target storage cell was warmed up to room temperature for one day and cooled down again. The recombination probability is greater than that in the previous experiment performed on Sep. 27, 2003, because the ice layer on the surface inside the target cell was lost during the day with the room temperature and the perfect

Drifilm layer had been partly destroyed due to the radiation from the interaction between the positron beam and gas atoms in the period during data taking. The κ result without $G(T)$ correction is shown in figure 4.7 while the results corrected with theoretical $G(T)$ functions is shown figure 4.8.

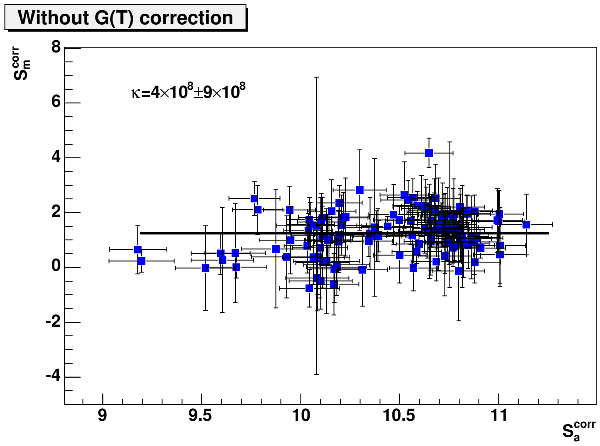

Figure 4.7: κ value from the temperature scan (Apr. 4, 2004) without $G(T)$ correction. Atomic and molecular signals of TGA have been corrected with the mean velocity passing through the ionizer and emission current of TGA.

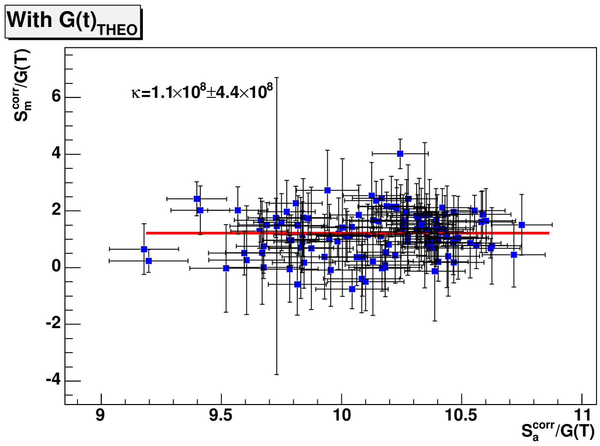

Figure 4.8: κ value from the temperature scan (Apr. 4, 2004) corrected with $G(T)_{THEO}$ functions from the theory. Atomic and molecular signals of TGA have been corrected with the mean velocity passing through the ionizer and emission current of TGA.

Due to TGA optical geometry has been slightly changed at the beginning of Oct., 2003, another $G(T)$ calibration with UGFS was arranged on the Apr. 10, 2004 for getting the κ value corrected with experimental $G(T)$. The normalized $G(T)$ result from the calibration is shown in figure 4.9 and the κ value corrected with it is shown in figure 4.11.

According to the theory, if one assumes, that the ratio of the detection efficiency for atoms and molecules is close to one, $\varepsilon_a \approx \varepsilon_m$, for the channeltron of TGA, then κ can be approximately given by $\kappa = \frac{\sigma_a}{\sigma_m} = 0.626$ for $70\,eV$ ionization energy of the electron gun. The cross sections used here are from [Sha87]. Considering the measured value for the $\kappa = 0.5507 \pm 0.00226$ with temperature scan on Aug. 16, 1997 and another $\kappa = 0.572 \pm 0.0026$ measured with HERA beam loss in Oct. 1997, and the storage cell, the position of sample tube and the TGA optical geometry has been slightly changed since then. The κ results show the methods to measure $G(T)$ by temperature with UGFS is reliable. If the TGA optical geometry hadn't been changed

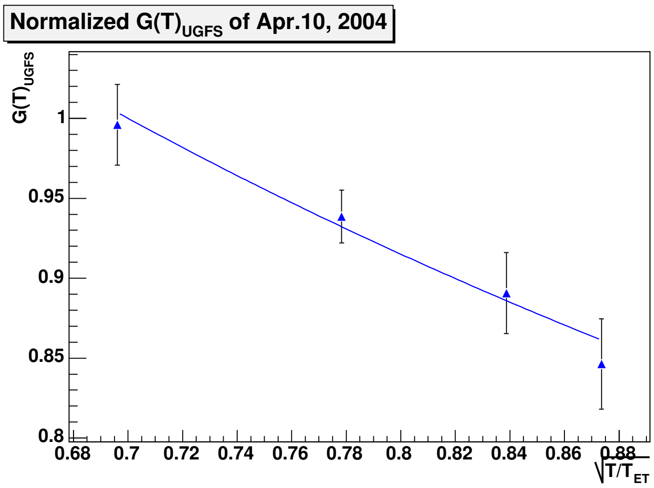

Figure 4.9: Normalized G(T) function is from the $G(T)$ calibration with UGFS performed on Apr. 10, 2004.

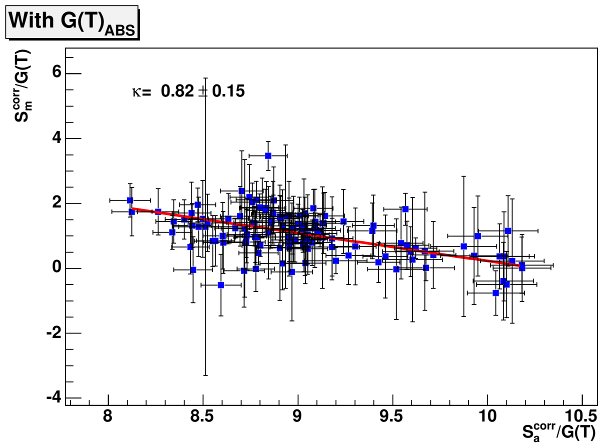

Figure 4.10: κ value from the temperature scan (Apr. 4, 2004) corrected with $G(T)_{ABS}$ functions from the temperature scan with ABS (Sep. 27, 2003). Atomic and molecular signals of TGA have been corrected with the mean velocity passing through the ionizer and emission current of TGA. The TGA optic geometry has been changed in the beginning of Oct., 2003, which will introduce a systematic deviation to the κ result.

after the storage cell installed, the $G(T)$ calibration with ABS was valid.

The reasons that the experimental $G(T)$ is more reliable than the theoretical $G(T)$ are:

- The assumption about the $T_{BT} = T_{IT} = T_{ST} = T$ is different from the fact. The temperature distribution is not uniform along the beam tube and along the sample tube.

- The temperature of the extension tube is not uniform either. The temperature sensor can

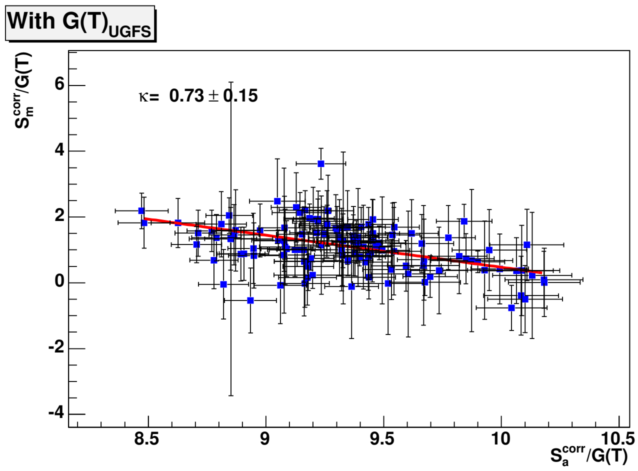

Figure 4.11: κ value from the temperature scan (Apr. 4, 2004) corrected with $G(T)_{UGFS}$ functions from the temperature scan with UGFS (Apr. 10, 2004) . Atomic and molecular signals of TGA have been corrected with the mean velocity passing through the ionizer and emission current of TGA.

only give the temperature at one point on the extension tube, the temperature distribution will change once the temperature of the sample tube changes.

- The size of the beam tube is not uniform: to avoid the thermal stress breaking the thin cell, many sunken surfaces are distributed along the beam tube.

Temperature distribution variations and sunken surfaces on beam tube will introduce some systematic errors when the conductance of those tubes is calculated with simple model. Due to the processes of cooling down the target storage cell are the same as during the temperature scans for $G(T)$ measurement and for κ calibration, those systematic errors are suppressed when we use the measured $G(T)$ to correct the signals of TGA during the κ calculation.

Besides the improvement in two new $G(T)$ calibration methods, analysis codes used in monitoring the performances of the target have been improved from old PAW[PAWSite] codes to ROOT[ROOTSite] codes. New calibration codes take the advantage of ROOT, and are more easily to maintain comparing with the old PAW codes.

Chapter 5

Calculation of the Sextupole Magnetic Field

The sextupole magnet plays an important role in ABS of HERMES. To improve the target thickness, HERMES group in FERRARA of Italy has done a lot of research. They plan to use a super conducting magnet instead of the permanent magnet to obtain stronger field and to increase the inner radius. ABS such as that of HERMES needs at least two magnets. One super conducting magnet has yet been built. Before making the second one, it is necessary to perform some simulation to confirm that the planned ABS can work with a pair of such supper conducting magnets.

The simulation is divided into 2 parts:

1. Calculation of the magnetic flux density distribution

2. Simulation with the distribution.

In this chapter, we will describe the calculation of the magnetic flux density. We have performed calculations with three different currents with a code named as MAFIA:

1A Comparing the calculation results of MAFIA with measured value in CERN to make sure our input file is correct.

517A Comparing the calculated results of MAFIA with measured value in FERRARA to make a judgement of which one is better, then using $\mu_{steel} = 1$ or H-B curve in table 5.2 to describe the property of the steel layer on the pole.

500A What is the designed working current. With the calculated results for the current equal to 500A as the input parameter for a code, named as SCANSHELL.X, to simulate the atoms' track inside the sextupole magnet while they pass through.

At the end of the chapter, some comments about the future simulation work are presented.

5.1 Sextupole magnet

There are two "pieces" of iron that are called yoke and inner iron of the pole in the sextupole magnet. The yoke is a almost cylindrical piece that surrounds the outside of the coils. There are 6 poles for each sextupole magnet. Each pole is made of a piece of iron inside and a layer of steel outside the iron for mechanical rigidity.

Outside the steel layer of each pole, super conducting NbTi wire are circled [Cap03]. The wire's cross section is $1.35\,mm \times 0.75\,mm$ and the ratio $\frac{Cu}{NbTi} = 1.63$. The coils were winded starting from the bottom, with the second loop above the first in the radial direction. Each of these loops of the wire in same layer has the same length. Practically, this is required for the coil to keep its shape, otherwise the second loop of wire does not stay in place while it is being glued. This constraint determines the shape of the coil. The coils have 14 turns of wire in the radial direction and 22 in the azimuthal. The coils cross section is roughly $19.3 \times 19.5\,mm^2$ along the straight section. The additional space is occupied by the glue. The designed specification about the current is 500 A in the wire[Mec03]. Figures 5.1 and 5.2 show the layout of the magnet.

The coils are electrically connected in series by two slabs. The wire's ends are fixed mechanically between the two slabs by 4 screws. Figure 5.3 shows the shape of a testing coil. And figure 5.4 shows the position of the coils inside the magnet.

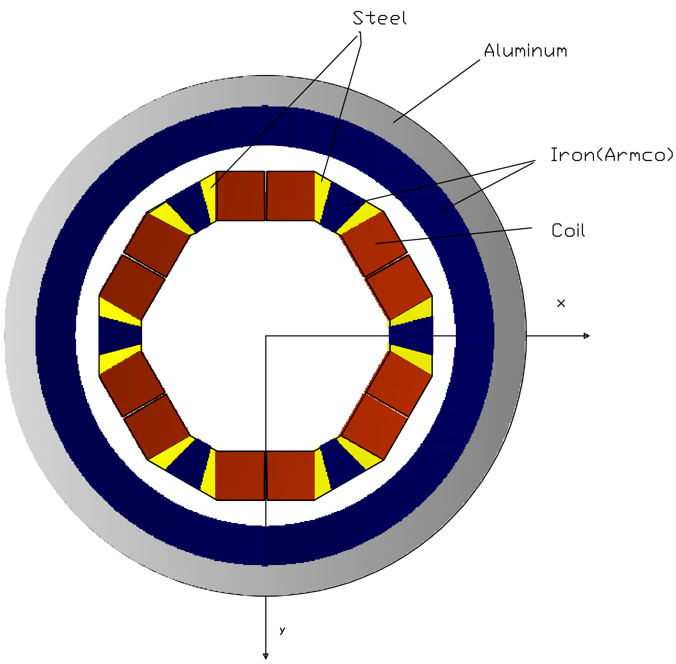

Figure 5.1: The magnet layout in the rϕ -plane.

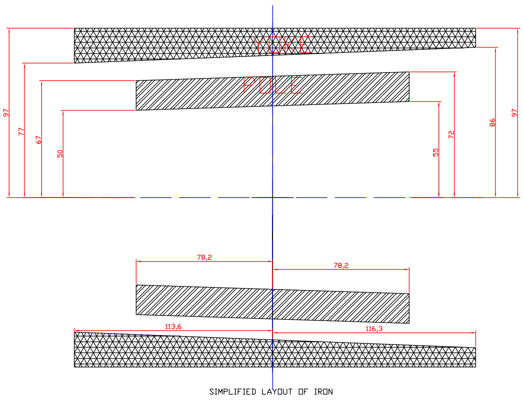

Figure 5.2:
The sextupole magnet layout in the rz-plane. Here only the relative geometry of the pole and iron yoke is shown. (Unit: mm)

Figure 5.3: The picture of the test coils. It is on the construction instrument. When being wined layer by layer with right shape, the coils are glued to keep the shape.

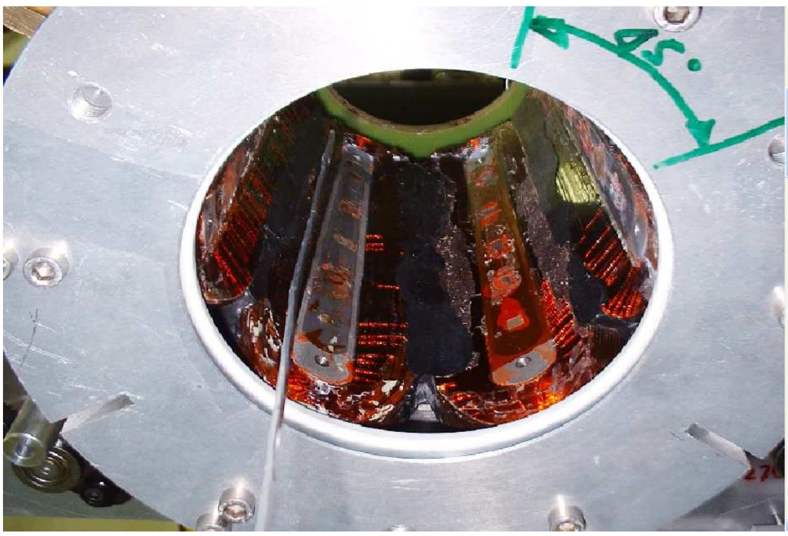

Figure 5.4:
Picture of the coil inside the sextupole magnet in FERRARA

5.2 MAFIA

We use MAFIA to calculate the magnetic flux density distribution of the sextuple magnet.

5.2.1 What is MAFIA?

MAFIA (Solution of **MA**xwell's Equations by the **F**inite **I**ntegration **A**lgorithm) , produced by Computer Simulation Technology(CST), is an interactive program package for the computation of electromagnetic fields.

The history of MAFIA is very old: It started with 2D frequency domain codes in 1977, followed by the first time domain codes for relativistic particle beams. The first fully three dimensional implementation was realized for 3D eddy current solvers in 1978. Later a new 3D code family for 3D resonators and transient fields was developed and got the current name, MAFIA, released in the first version in 1983. Following the first release, the code was improved significantly.

MAFIA is directly based on the fundamental equations of electromagnetic fields, the Maxwell equations. The simulation is based on the theory of discrete Maxwell grid equations, the Finite Integration Technique (FIT), which was developed during the last 20 years. The formulation of Maxwell's equations are in the form of algebraic matrix equations. The matrices fulfill the same formal relations as the differential operators in the basic field equations. The vector solutions on the grid possess the same physical properties as the electromagnetic fields. MAFIA is a modular and divided into preprocessor, postprocessor and solvers for different special cases of Maxwell equations[Bar92, MAF3x].

MAFIA includes an optimizer, which runs interactively as well as in batch or semi interactive using predefined command sequences. It has a powerful command language for automation and optimization purposes and an advanced interactive graphical output with thousands of display options.

The following modules are available[MAF00] :

- M: Preprocessor, includes solid modeler, CAD import and 3D graphics.
- P: Postprocessor, includes 3D graphics and calculation of deduced quantities like far field and impedance.
- S: Static field module, solves electrostatics, magnetostatics, heat flow problems, stationary current flow problems and electro-quasistatic problems.
- T3: Time domain module, simulates time dependent wave propagation, most general and versatile in application. Uses Cartesian coordinates.
- TS3: Time domain module, simulates charged particle movement in time dependent fields including the interaction of particles and fields. Uses Cartesian coordinates only.

- TS2: Time domain module, simulates charged particle movement in time dependent fields including the interaction of particles and fields in cylinder symmetrical structures.
- E: Frequency domain eigenmode module, finds modes in resonators and waveguides.
- W3: Frequency domain module, covers the whole frequency range.
- H3 : Thermodynamic module, solving thermodynamic problems in time domain in either Cartesian or polar coordinate system.
- T2: Time domain module, simulates time dependent wave propagation within cylinder symmetrical structures. Not yet available under GUI.
- OO: Optimizer with many built in strategies. Optimizing capabilities not yet completely available under GUI.
- A3: Time domain acoustic solver. Not yet available under GUI.

5.3 Method of Magnetic Flux Density Calculation

MAFIA has provided some functions, which are very basic shapes such as brick, cylinder, circular or elliptical cylinder, sphere, circular or elliptical cone, ellipsoid, washer, torus, figure of rotation et al., to construct model before calculating. The method that we used to make the model for calculating the magnetic flux density distribution is as follows:

5.3.1 Model Construction

According to the information from FERRARA[Mec03], we use the following parameters to perform the calculation: In the r-z-ϕ coordinate system, the yoke extends from 11.36 cm to 11.63 cm in z. At the end where $z = 11.36\,cm$, it covers the space from $r = 7.7\,cm$ to 9.7 cm. At the other end, it covers from 8.6 to 9.7 cm. And 360 degrees in azimuth.

Due to the shape of the pole is a little complicated comparing with other parts, it is very important to model poles as detail as possible, or the calculated results of the distribution of magnetic flux density will be distorted from that of the real shape.

The method to describe the inner part of iron (ARMCO) inside the poles, shown in as figure 5.5, with MAFIA can be divided into two steps:

The first one is to construct the main part of the iron. Taking the advantage of logical calculating functions, with very basic shapes provided by MAFIA as shown in figure 5.6 a bar is made in a trapezoid shape in the cross section. The width of bottom edge equals 1.178 cm at the end where $z = -7.689\,cm$, and the other width of bottom is 0.632 cm at $z = 7.962\,cm$; The edge's width at the top is 2.073 cm at $z = -7.2415\,cm$ and 1.527 cm at $z = 7.5145\,cm$. The big head of the pole is at negative coordinate along z axis.

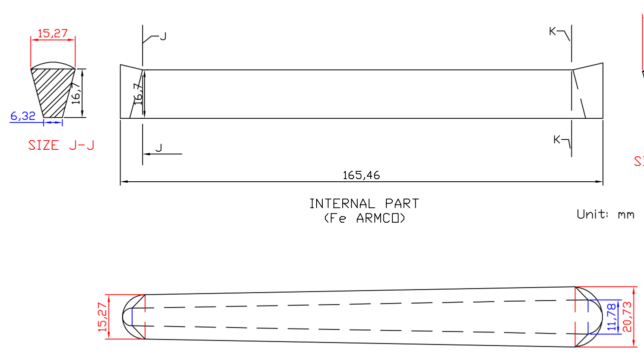

Figure 5.5: Inner iron inside the steel layer of sextupole magnet pole using in MAFIA calculation.(Unit: mm)

Next step is to make one of the ends of the iron. Put a half cylinder with r_1 of the bottom end equal to $\frac{1.178}{2} = 0.589\,cm$ and r_2 of the top end $\frac{2.073}{2} = 1.0365\,cm$ at $z = -7.689\,cm$ with height $\sqrt{1.67^2 + (1.0365 - 0.589)^2} = 1.729\,cm$. Then this cylinder is rotated around bottom edge in clockwise direction until the center of the top half circle touch the face of the trapezoid at $z = -7.2415\,cm$. See (a) to (b) step in figure 5.7. After rotating the half cylinder, we put a cylinder with radius $r = 0.589\,cm$ at both the bottom and top faces as patch to fill the gap left from the rotating near the bottom of the half cylinder((c) of figure 5.7). So far one end of the inner iron is finished constructing. The 3-D shape drawing of the end with MAFIA can be found in figure 5.8. The same method is applied in constructing the end in the other side.

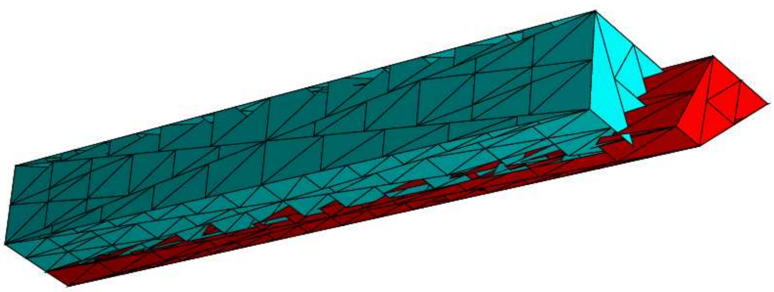

Figure 5.6: Constructing the main part of the inner iron through logical calculation method to trim a cuboid with a slab after rotating to the right position

The next tricky work is to construct the steel layer. Thanks to the feature of MAFIA about material describing: When put two different materials in the same space, the later will replace the previous one. Taking the advantage of this feature, we can simply construct a solid bar with the same shape looking from outside as the steel layer instead of constructing a steel layer leaving a hollow for the inner iron. The size of the solid steel layer is shown in figure 5.9. The shape of one end is given in figure 5.10. The method to construct the steel is similar with that constructing the inner iron of the pole: First, make a trapezoid shape bar with width $1.256\,cm$

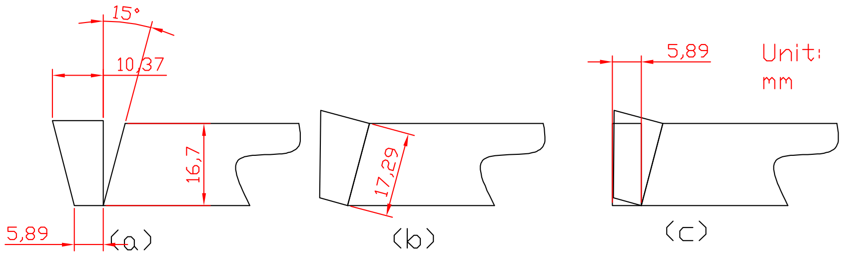

Figure 5.7: The steps to construct the end of inner iron inside the pole with MAFIA. (a) construct a half cylinder for attaching on the trapezoidal iron. (b) rotate the half cylinder until touching the face of the trapezoidal body. (c) add cylinder a patch filling the gap left from rotating. (Unit: mm)

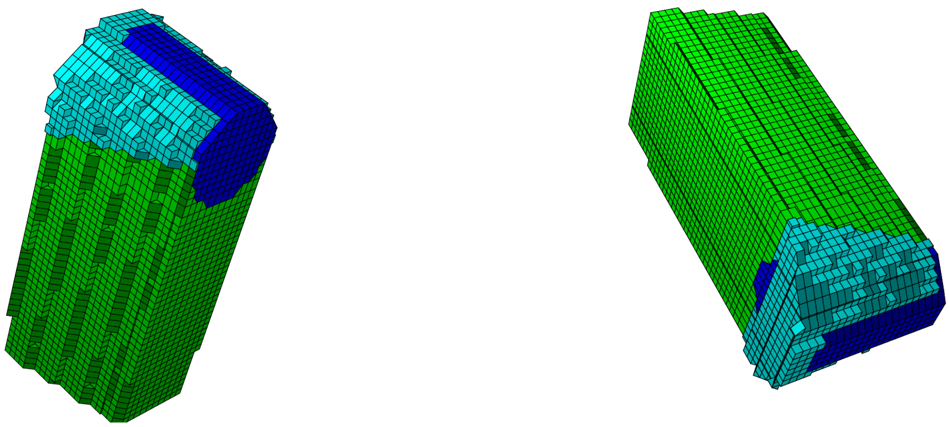

Figure 5.8: The head of inner iron inside the pole drawn with MAFIA

at $z = 8.9165\,cm$ and width $1.94\,cm$ at $z = -8.5745\,cm$ for the bottom edge while the top edge with width of $3.243\,cm$ at $z = 7.4755\,cm$ and $3.91\,cm$ at $z = -7.1420\,cm$. Then construct a half cylinder and put the center of the bottom at $z = -7.1420\,cm$ with the radius of the bottom equals $\frac{1.94}{2} = 0.97$cm and the radius of the cross section parallel to the bottom at height of $1.67\,cm$ is $\frac{3.91}{2} = 1.955\,cm$. The total height of the half cylinder is $2.3\,cm$ to leave enough space for trimming to get the right shape (see (a) of figure 5.11). After drawing the half cylinder, we perform skewing along horizontal direction while keeping the height in vertical direction unchanged until the angle between the bevel edge and bottom plane equals $75°$. The result is shown in (b) of figure 5.11. The next step is to trim with the line shown in figure 5.10 with the powerful functions about logical calculation. The finial shape of the steel layer for one end is shown in (c) of figure 5.11. The other end has been constructed with the similar method and with same cutting line to trim out the curved face on the top.

After constructing the steel layer, the next step is to wind the wires on the outside of the steel layer. We use 3×4 coils representing 14×22 coils while increasing the current $\frac{14\times22}{3\times4} = 25.6667$ times for saving the memory of computer and increasing the speed. There are 3 layers of coils

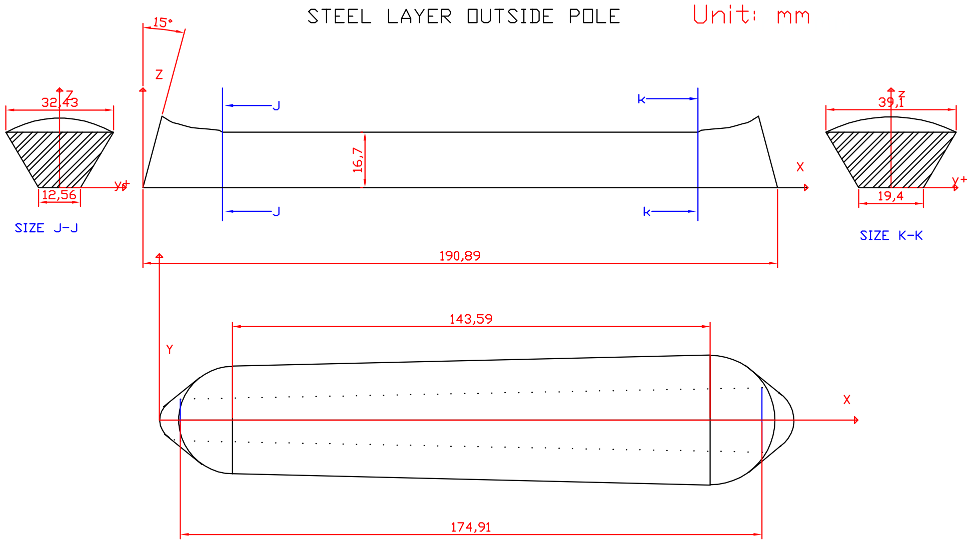

Figure 5.9: The size of pole with steel layer

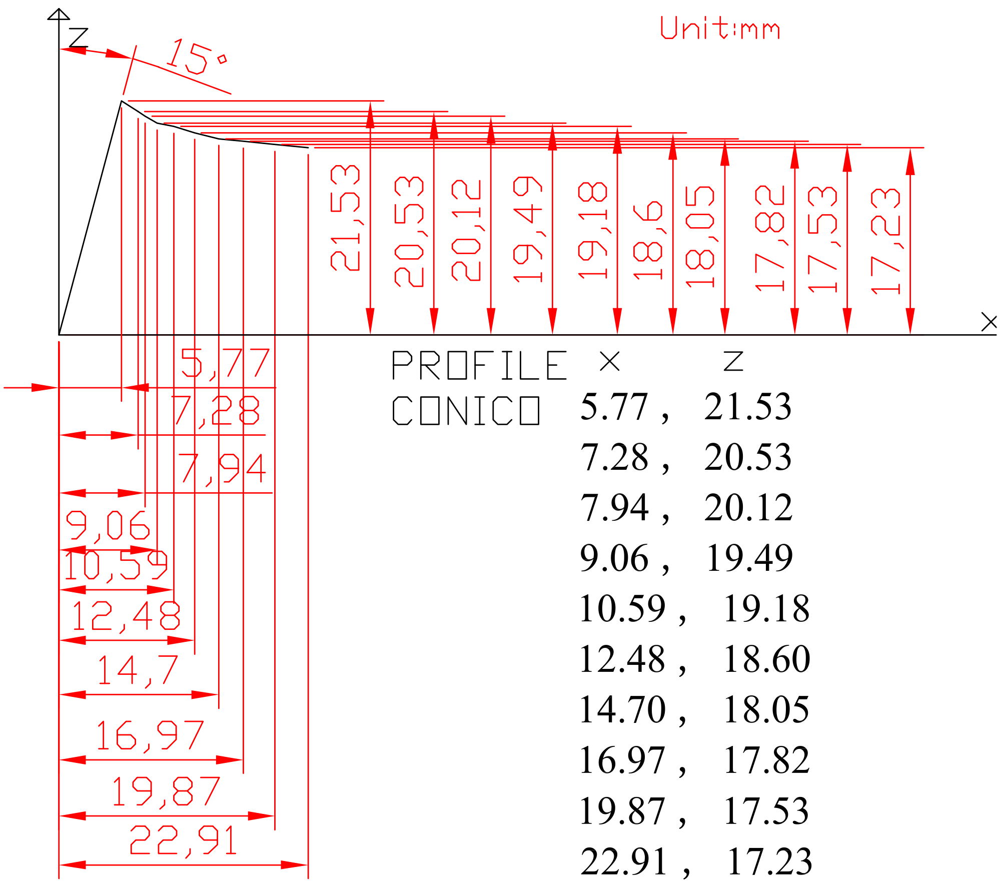

Figure 5.10: The conic lines used to define the shape of the steel layer

in radial direction equally distributed along the 1.93 cm side bevel edge of the steel layer and 4 layers of coils in ϕ(azimuthal, perpendicular to the side face of the steel layer) with equal gaps

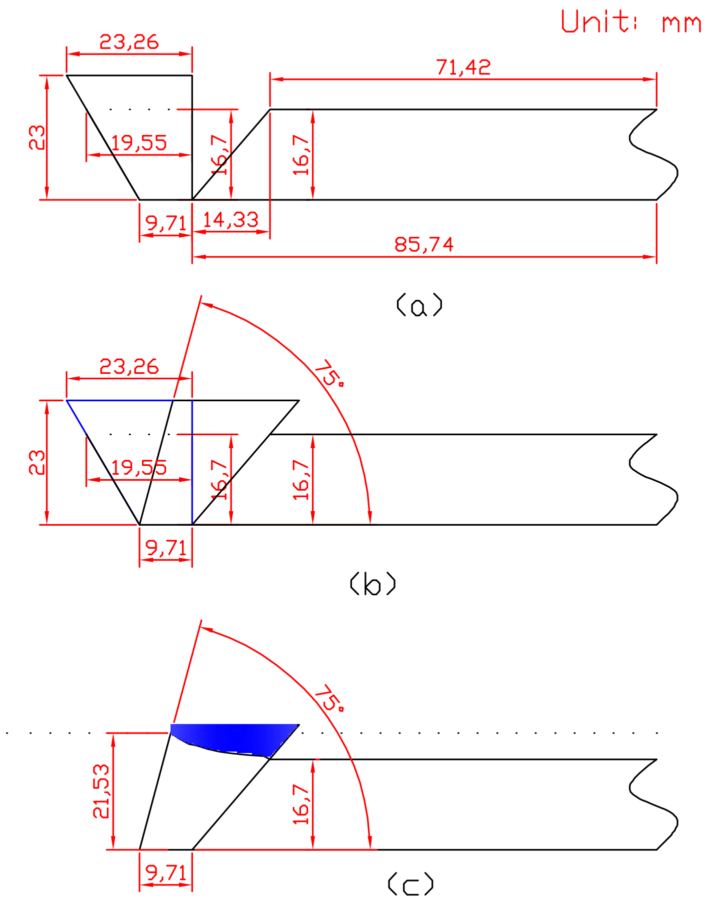

Figure 5.11: Sketch map about steps to make the model of steel layer with MAFIA
(a) Draw the half cylinder (b) Skew the cylinder until the angle between bevel edge and bottom plane equals 75^o
(c) Trim the filled part with a curve line given in figure 5.10.

of 1.95 cm between each sequential coils. For describing the coils in the side part of the steel layer, we use a straight line; for the coils at the end part, we use 18 short lines connecting one after the other describing the arc line. The layout of constructed coils and the pole(including the inner iron and the steel layer) is shown in figure 5.12.

To prepare the input file about those wires, we has written a special code with ROOT to calculate the exact coordinate of every turning points on each wires.

After using the inner iron to fill the steel layer, we perform rotating to keep the pole (both the inner iron and the steel layer) at the right position: at the end $z = 7.82\,cm$, it extends from radius equal to 5.0 to 6.7 cm; at the other end, $z = -7.82\,cm$, the distance from center axis of the magnet to the inner surface is 5.5 cm. The other 5 poles can be done by copying the first one.

The data of H-B curve for the inner iron (ARMCO) of the pole and the yoke are listed in table 5.1. The data of H-B curve for steel layer are listed in table 5.2.

Table 5.1: H-B curve for iron (ARMCO) used in yoke and inner part of pole[Mec03]

H[A/m]	B (T)	H[A/m]	B (T)	H[A/m]	B (T)
1000	0.5	18000	1.88	120000	2.21
3000	1.15	25000	1.96	160000	2.26
5000	1.454	40000	2.06	200000	2.31
9000	1.72	60000	2.11		
13000	1.81	80000	2.15		

Table 5.2: H-B curve for steel used in the steel layer of pole[Ema37]

H[A/m]	B (T)	H[A/m]	B (T)	H[A/m]	B (T)
0	0.0	200.0	0.2512	2937.5	1.5721
17.9	0.0081	270.2	0.4418	3964.4	1.6400
24.6	0.0117	364.2	0.6358	5349.5	1.7001
32.8	0.0166	489.6	0.8080	7212.3	1.7577
39.6	0.0206	659.7	0.9673	9696.0	1.8163
44.8	0.0240	889.6	1.1175	13087.2	1.8797
60.5	0.0351	1191.1	1.2548	17577.0	1.9461
81.3	0.0518	1200.1	1.2581	23881.8	2.0181
109.7	0.0799	1618.0	1.3840		
148.5	0.1349	2179.2	1.4885		

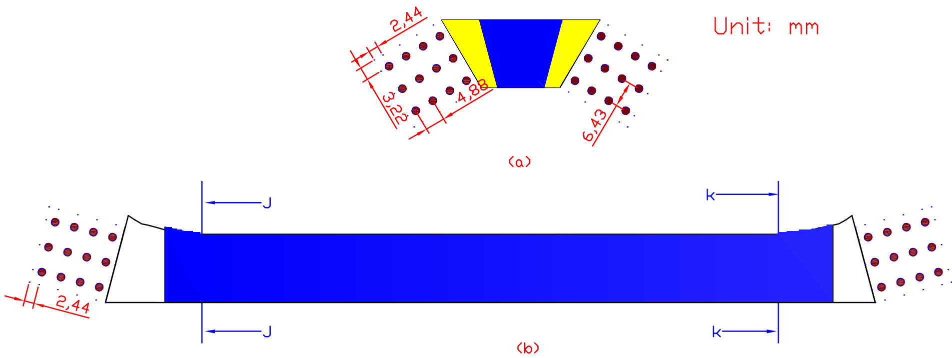

Figure 5.12: The coils outside the pole (a) Section in the vertical plane perpendicular to z axis (b) Section in the vertical plane along z axis passing through the middle of pole

5.4 Magnetic Field Calculated with MAFIA

All the calculations with different current are applied in x-y-z reference frame. z axis is the symmetric center line of the magnet, x axis passes through one pole and y axis through a gap between two coils of different poles. One calculation will cost 2 days and need about 1Gb memory. After calculating, we put the results into root files for the further analysis.

5.4.1 2D Results of Magnet Field with 1A in Coils

The results of magnetic flux density are given in $\vec{B}_x$, $\vec{B}_y$ and $\vec{B}_z$ components with the coordinate information. For getting a general idea about the distribution of magnetic flux density, we show several 2-Dimension plots at different planes in figure 5.13 and figure 5.14. Those results are from the calculation using the H-B curves listed in table 5.2 for the steel layer.

In principle, the result in figure 5.13 should be symmetric every 30° and one period is 60°. The little differences are due to that the x-y-z reference frame is not symmetric in ϕ direction. Using quadrate grids to describe a circular shape will introduce some distortion. Same effects can be seen clearly in the right plot of figure 5.14. The inner surface of the yoke is smooth diagonal line but now turning into several step lines at the edge in the cross section.

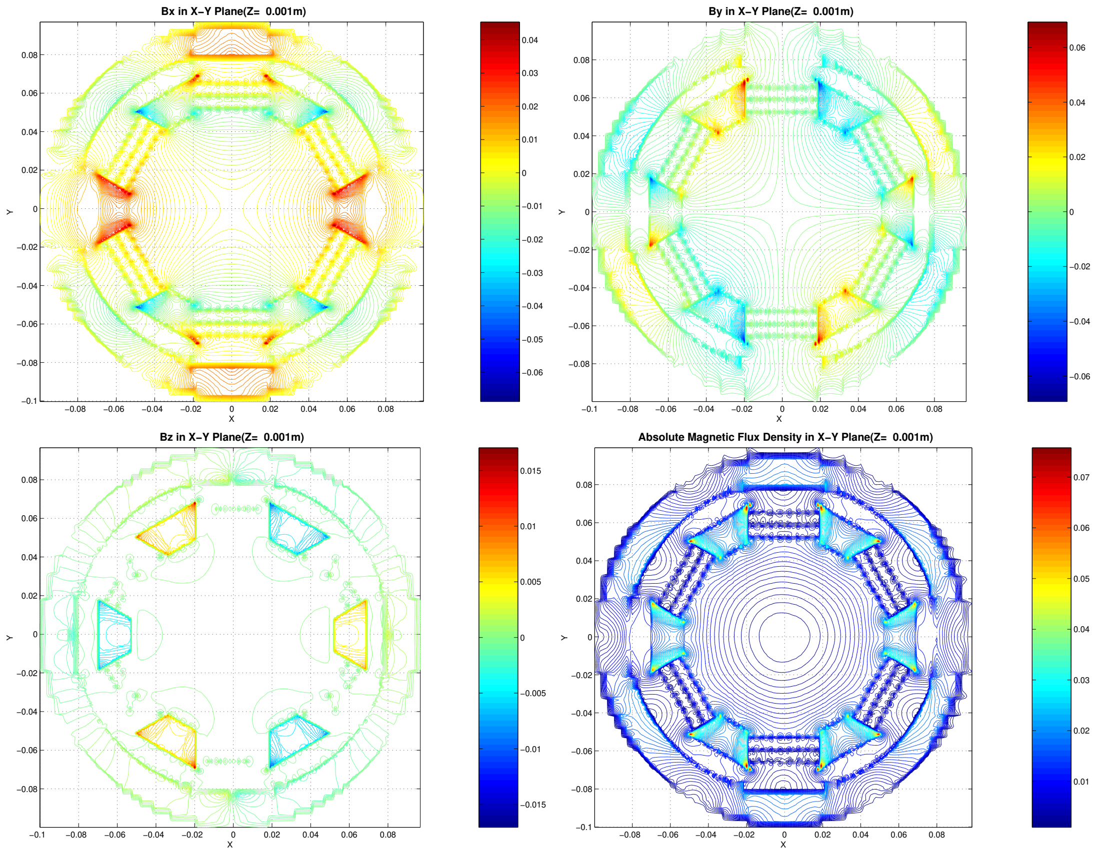

Figure 5.13: The distribution of $\vec{B}_x$(left up), $\vec{B}_y$(right up), $\vec{B}_z$(left down) and absolute magnetic flux density $\left|\vec{B}\right|$(right down) in X-Y plane where z=0.1cm.$\left|\vec{B}\right| = \sqrt{\vec{B}_x^2 + \vec{B}_y^2 + \vec{B}_z^2}$. Using the H-B curve to describe the property of steel layers. ($I = 1$ A; Units of x-, y- axis: m; B: T)

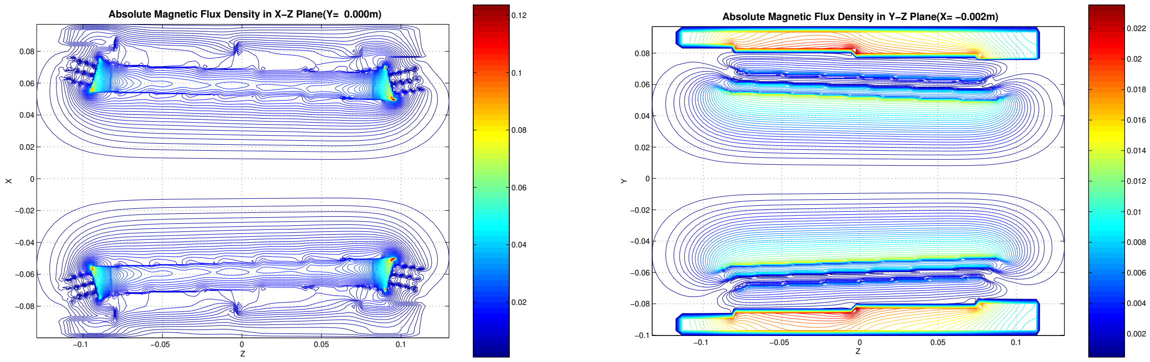

Figure 5.14: The distribution of absolute magnetic flux $\left|\vec{B}\right|$ density in X-Z and Y-Z planes where $\left|\vec{B}\right| = \sqrt{\vec{B}_x^2 + \vec{B}_y^2 + \vec{B}_z^2}$. For the Left plot, $Y = 0cm$ means the plane passes through the center of pole; For the Right plot, $X = 0.2\,cm$, the plane passes through the gap between tow coils belong to different poles. Using the H-B curve to describe the property of steel layers. ($I = 1$ A; Units of x-, y-, z- axis: m; B: T)

5.4.2 1D Results of Magnet Field with 1A in Coils

There are two calculations with 1A in the coils: One uses the H-B curve listed in table 5.2 to describe the property of the steel layer outside the pole. The other calculation is using relative permeability $\mu_{steel} = 1$ to describe the property due to that we don't know the right H-B curve of the steel layer. Of course, for the inner iron, we use both the same H-B curve listed in table 5.1, which we know exactly.

Results Using H-B Curve Describing Steel Layer

The calculated results are analyzed to obtain a reasonable Fourier analysis of the sextupole magnetic field. The dipole, quadrupole, sextupole, 8-pole, 10-pole, 12-pole, 18-pole and 24-pole components are calculated on each x-y plane passing different points along z-axis. Those values can be obtained by fitting the components of magnet field density in r direction and in θ direction within cylindrical coordinates with functions:

$$B_r\left(r,\theta\right) = \sum_n K_n \left(\frac{r}{r_M}\right)^{n-1} \cos\left(n\theta\right)$$

$$B_\theta\left(r,\theta\right) = \sum_n K_n \left(\frac{r}{r_M}\right)^{n-1} \sin\left(n\theta\right)$$

Where $2n$ is the component number of poles and r_M is the reference radius. For an ideal sextupole magnet, it should have only n=3 components. θ is the angle between two planes: one passes through z-axis and x-axis(which passes through the center of the inner iron of poles) and the other passes through z-axis and the calculated(measured) point.

The fitting results for the one which uses the H-B curve shown in table 5.2 describing the steel are listed in tables 5.3 and 5.4. Where $r_M = 4.9\,cm$. The z axis coincides with the geometrical center symmetric axis and its origin(where z=0) is set in the middle of the pole. The bigger venthole of the sextupole magnet is placed at negative z while the smaller one is at positive. During the fitting, only the contributions from K_1, K_2, K_3, K_4, K_5, K_6, K_9 and K_{12} are taken into account. The data points are selected from the two regions along axis x and y at different z. The selecting cut is as follows:

- along z-axis: $-0.2\,cm < (z - z_0) < 0.2\,cm$.
- along y-axis: $-0.2\,cm < y < 0.2\,cm$
- along x-axis: $1.0\,cm < x < 4.5\,cm$

Where z_0 are the coordinate values along z-axis. We give the value $z_0 = -13\,cm, -12\,cm, \cdots, 11\,cm, 12\,cm, 13\,cm$ for demonstrating the distributions of magnet field. For the data along x-axis, the $\vec{B}_x$ component can be taken as $\vec{B}_r$ in the fitting with $\theta = 0°$. $\vec{B}_x$ component along y-axis are taken as B_θ with $\theta = 90°$ during the fitting .

Table 5.3: Fitting results of K_1, K_2, K_3, and K_4[gauss] for 1A current in coils calculated with MAFIA using H-B curve for steel layers as that in the table 5.2.

z (cm)	K_1	K_2	K_3	K_4
-13.0	0.069 ± 0.036	-0.175 ± 0.211	-13.388 ± 0.329	7.890 ± 0.840
-12.0	0.074 ± 0.036	0.118 ± 0.211	-24.418 ± 0.329	9.941 ± 0.840
-11.0	0.077 ± 0.036	0.848 ± 0.211	-44.515 ± 0.329	8.259 ± 0.840
-10.0	-0.773 ± 0.041	10.574 ± 0.136	-93.135 ± 0.199	28.636 ± 0.266
-9.0	-1.549 ± 0.049	19.252 ± 0.179	-142.884 ± 0.305	43.730 ± 0.480
-8.0	0.197 ± 0.021	1.900 ± 0.122	-104.756 ± 0.190	0.160 ± 0.482
-7.0	0.192 ± 0.025	2.440 ± 0.149	-116.953 ± 0.232	0.766 ± 0.591
-6.0	0.209 ± 0.036	2.391 ± 0.211	-124.012 ± 0.329	4.648 ± 0.840
-5.0	0.216 ± 0.036	2.341 ± 0.211	-127.517 ± 0.329	6.615 ± 0.840
-4.0	0.225 ± 0.025	2.180 ± 0.149	-130.230 ± 0.232	8.622 ± 0.591
-3.0	0.219 ± 0.036	2.214 ± 0.211	-132.583 ± 0.329	9.141 ± 0.840
-2.0	0.222 ± 0.036	2.178 ± 0.211	-134.480 ± 0.329	9.985 ± 0.840
-1.0	0.222 ± 0.025	2.299 ± 0.149	-136.785 ± 0.232	10.040 ± 0.591
0.0	0.233 ± 0.036	2.324 ± 0.211	-138.994 ± 0.329	10.620 ± 0.840
1.0	0.244 ± 0.036	2.312 ± 0.211	-140.867 ± 0.329	11.684 ± 0.840
2.0	0.253 ± 0.025	2.345 ± 0.149	-142.980 ± 0.232	12.553 ± 0.591
3.0	0.242 ± 0.036	2.540 ± 0.211	-145.116 ± 0.329	12.141 ± 0.840
4.0	0.217 ± 0.036	2.588 ± 0.211	-146.941 ± 0.329	13.447 ± 0.840
5.0	0.210 ± 0.036	2.563 ± 0.211	-148.094 ± 0.329	13.141 ± 0.840
6.0	0.179 ± 0.025	2.842 ± 0.149	-148.382 ± 0.232	10.899 ± 0.591
7.0	0.122 ± 0.036	3.400 ± 0.211	-145.116 ± 0.329	5.541 ± 0.840
8.0	-2.141 ± 0.049	26.210 ± 0.179	-204.661 ± 0.305	29.377 ± 0.480
9.0	-2.451 ± 0.049	29.665 ± 0.179	-203.581 ± 0.305	56.836 ± 0.480
10.0	-1.929 ± 0.035	20.952 ± 0.131	-138.082 ± 0.198	18.989 ± 0.267
11.0	0.034 ± 0.021	1.457 ± 0.122	-53.638 ± 0.190	11.715 ± 0.482
12.0	0.074 ± 0.025	0.187 ± 0.149	-30.541 ± 0.232	14.812 ± 0.591
13.0	0.082 ± 0.036	-0.362 ± 0.211	-13.695 ± 0.329	10.630 ± 0.840

Table 5.4: Fitting results of K_5, K_6, K_9 and K_{12}[gauss] for 1A current in coils calculated with MAFIA using H-B curve for steel layers as that in the table 5.2.

z (cm)	K_5	K_6	K_9	K_{12}
-13.0	-7.840 ± 0.667	13.607 ± 1.014	0.332 ± 0.537	-2.807 ± 0.797
-12.0	-11.587 ± 0.667	23.313 ± 1.014	-0.935 ± 0.537	-1.636 ± 0.797
-11.0	-11.864 ± 0.667	26.666 ± 1.014	-5.560 ± 0.537	7.218 ± 0.797
-10.0	48.165 ± 0.326	-70.534 ± 0.382	26.111 ± 0.571	-5.341 ± 0.572
-9.0	102.498 ± 0.698	-169.033 ± 0.974	68.427 ± 2.454	-55.950 ± 3.976
-8.0	5.342 ± 0.385	-29.010 ± 0.584	-8.661 ± 0.310	7.980 ± 0.460
-7.0	0.748 ± 0.471	-12.197 ± 0.715	-8.122 ± 0.380	8.809 ± 0.563
-6.0	-3.525 ± 0.667	-3.223 ± 1.014	-8.066 ± 0.537	8.652 ± 0.797
-5.0	-5.642 ± 0.667	0.822 ± 1.014	-8.318 ± 0.537	4.684 ± 0.797
-4.0	-6.676 ± 0.471	0.542 ± 0.715	-8.853 ± 0.380	7.741 ± 0.563
-3.0	-7.269 ± 0.667	1.202 ± 1.014	-9.684 ± 0.537	3.864 ± 0.797
-2.0	-7.506 ± 0.667	0.170 ± 1.014	-10.565 ± 0.537	8.598 ± 0.797
-1.0	-7.955 ± 0.471	1.006 ± 0.715	-11.322 ± 0.380	4.829 ± 0.563
0.0	-8.336 ± 0.667	0.744 ± 1.014	-12.373 ± 0.537	10.232 ± 0.797
1.0	-8.786 ± 0.667	-1.256 ± 1.014	-13.027 ± 0.537	8.453 ± 0.797
2.0	-9.074 ± 0.471	-1.978 ± 0.715	-14.097 ± 0.380	7.433 ± 0.563
3.0	-9.362 ± 0.667	1.006 ± 1.014	-15.021 ± 0.537	10.775 ± 0.797
4.0	-10.060 ± 0.667	-2.126 ± 1.014	-15.151 ± 0.537	7.550 ± 0.797
5.0	-9.287 ± 0.667	-5.443 ± 1.014	-17.258 ± 0.537	8.594 ± 0.797
6.0	-7.367 ± 0.471	-9.039 ± 0.715	-19.089 ± 0.380	17.508 ± 0.563
7.0	-2.843 ± 0.667	-19.076 ± 1.014	-21.199 ± 0.537	12.234 ± 0.797
8.0	180.554 ± 0.698	-256.770 ± 0.974	64.705 ± 2.454	-20.386 ± 3.976
9.0	198.943 ± 0.698	-324.282 ± 0.974	139.678 ± 2.454	-158.778 ± 3.976
10.0	67.794 ± 0.327	-56.410 ± 0.383	-70.088 ± 0.574	29.629 ± 0.573
11.0	-20.090 ± 0.385	47.569 ± 0.584	-9.634 ± 0.310	11.780 ± 0.460
12.0	-18.015 ± 0.471	36.496 ± 0.715	-1.415 ± 0.380	-3.172 ± 0.563
13.0	-10.054 ± 0.667	16.143 ± 1.014	0.924 ± 0.537	-4.649 ± 0.797

Results Using $\mu_{steel} = 1$ Describing Steel Layer

Frankly, we don't know the real H-B curve of the steel layer until now. If we closely research the two H-B curves listed in table 5.1 and table 5.2, we will recognize that the curves are very similar, see figure 5.15. It is useful to perform another calculation to obtain the contribution

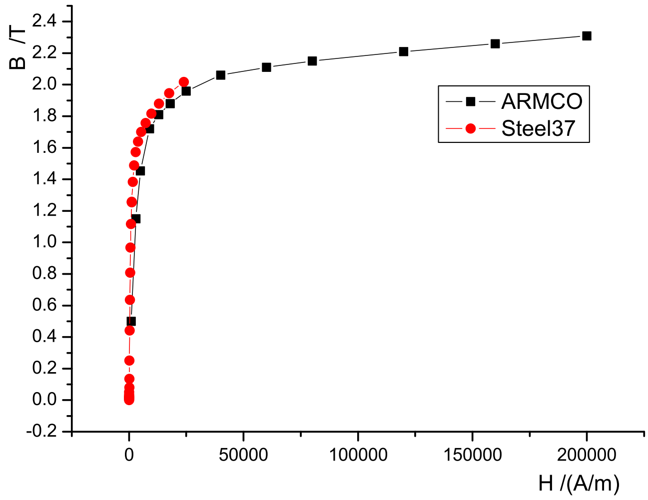

Figure 5.15: The plots of H-B curves of Steel 37 and ARMCO iron

from the steel layer by setting the relative permeability, μ, equal 1. From the calculating results, we obtain the K_1, K_2, K_3, K_4, K_5, K_6, K_9 and K_{12}. The values are listed in table 5.5 and 5.6. The cuts are the same as previous data analyses during selecting data fitting.

Table 5.5: Fitting results of K_1, K_2, K_3, and K_4[gauss] for 1A current in coils calculated with MAFIA by setting $\mu_{steel} = 1$

z (cm)	K_1	K_2	K_3	K_4
-13.0	0.036 ± 0.036	-0.142 ± 0.211	-8.848 ± 0.329	5.400 ± 0.840
-12.0	0.043 ± 0.036	-0.034 ± 0.211	-16.212 ± 0.329	7.324 ± 0.840
-11.0	0.052 ± 0.036	0.305 ± 0.211	-30.205 ± 0.329	7.786 ± 0.840
-10.0	-0.726 ± 0.041	9.246 ± 0.136	-73.327 ± 0.199	32.883 ± 0.266
-9.0	-1.017 ± 0.049	12.451 ± 0.179	-100.122 ± 0.305	27.518 ± 0.480
-8.0	0.042 ± 0.021	2.042 ± 0.122	-84.299 ± 0.190	0.516 ± 0.482
-7.0	0.052 ± 0.025	2.253 ± 0.149	-98.681 ± 0.232	1.426 ± 0.591
-6.0	0.038 ± 0.036	2.563 ± 0.211	-108.573 ± 0.329	3.607 ± 0.840
-5.0	0.031 ± 0.036	2.681 ± 0.211	-113.567 ± 0.329	5.774 ± 0.840
-4.0	0.036 ± 0.025	2.563 ± 0.149	-116.953 ± 0.232	8.711 ± 0.591
-3.0	0.026 ± 0.036	2.653 ± 0.211	-119.354 ± 0.329	9.365 ± 0.840
-2.0	0.021 ± 0.036	2.598 ± 0.211	-121.058 ± 0.329	10.544 ± 0.840
-1.0	-0.001 ± 0.025	2.792 ± 0.149	-123.075 ± 0.232	10.337 ± 0.591
0.0	-0.009 ± 0.036	2.797 ± 0.211	-124.852 ± 0.329	10.914 ± 0.840
1.0	-0.017 ± 0.036	2.844 ± 0.211	-126.317 ± 0.329	11.380 ± 0.840
2.0	-0.021 ± 0.025	2.942 ± 0.149	-127.973 ± 0.232	11.788 ± 0.591
3.0	-0.033 ± 0.036	3.219 ± 0.211	-129.702 ± 0.329	11.221 ± 0.840
4.0	-0.057 ± 0.036	3.507 ± 0.211	-131.095 ± 0.329	11.131 ± 0.840
5.0	-0.065 ± 0.036	3.742 ± 0.211	-131.311 ± 0.329	8.798 ± 0.840
6.0	-0.088 ± 0.025	3.968 ± 0.149	-129.006 ± 0.232	5.525 ± 0.591
7.0	-0.107 ± 0.036	4.004 ± 0.211	-120.890 ± 0.329	1.138 ± 0.840
8.0	-2.873 ± 0.049	33.413 ± 0.179	-210.208 ± 0.305	79.731 ± 0.480
9.0	-1.664 ± 0.049	19.497 ± 0.179	-142.499 ± 0.305	44.613 ± 0.480
10.0	-3.572 ± 0.035	38.225 ± 0.131	-182.548 ± 0.198	110.355 ± 0.267
11.0	0.042 ± 0.021	0.349 ± 0.122	-35.103 ± 0.190	9.688 ± 0.482
12.0	0.031 ± 0.025	-0.010 ± 0.149	-20.104 ± 0.232	10.034 ± 0.591
13.0	0.032 ± 0.036	-0.227 ± 0.211	-9.119 ± 0.329	6.966 ± 0.840

Table 5.6: Fitting results of K_5, K_6, K_9 and K_{12} [gauss] for 1A current in coils calculated with MAFIA by setting $\mu_{steel} = 1$

z (cm)	K_1	K_2	K_3	K_4
-13.0	-5.221 ± 0.667	8.887 ± 1.014	0.242 ± 0.537	-1.822 ± 0.797
-12.0	-7.840 ± 0.667	14.963 ± 1.014	-0.430 ± 0.537	-1.309 ± 0.797
-11.0	-9.287 ± 0.667	19.536 ± 1.014	-2.385 ± 0.537	0.912 ± 0.797
-10.0	35.822 ± 0.326	-56.947 ± 0.382	36.722 ± 0.571	-15.135 ± 0.572
-9.0	66.756 ± 0.698	-97.539 ± 0.974	39.813 ± 2.454	-14.169 ± 3.976
-8.0	1.125 ± 0.385	-16.155 ± 0.584	-3.692 ± 0.310	-17.629 ± 0.460
-7.0	1.236 ± 0.471	-19.121 ± 0.715	-5.912 ± 0.380	-8.019 ± 0.563
-6.0	-3.076 ± 0.667	-7.808 ± 1.014	-6.441 ± 0.537	-2.722 ± 0.797
-5.0	-6.520 ± 0.667	0.127 ± 1.014	-6.215 ± 0.537	-7.956 ± 0.797
-4.0	-8.693 ± 0.471	1.832 ± 0.715	-6.085 ± 0.380	-6.717 ± 0.563
-3.0	-9.817 ± 0.667	4.031 ± 1.014	-6.334 ± 0.537	-13.180 ± 0.797
-2.0	-10.227 ± 0.667	2.739 ± 1.014	-6.770 ± 0.537	-9.462 ± 0.797
-1.0	-10.930 ± 0.471	4.477 ± 0.715	-6.999 ± 0.380	-15.733 ± 0.563
0.0	-11.270 ± 0.667	3.895 ± 1.014	-7.547 ± 0.537	-11.460 ± 0.797
1.0	-11.766 ± 0.667	3.034 ± 1.014	-7.624 ± 0.537	-15.972 ± 0.797
2.0	-12.291 ± 0.471	3.302 ± 0.715	-7.866 ± 0.380	-20.108 ± 0.563
3.0	-12.683 ± 0.667	6.375 ± 1.014	-8.152 ± 0.537	-17.055 ± 0.797
4.0	-13.086 ± 0.667	5.469 ± 1.014	-7.853 ± 0.537	-25.328 ± 0.797
5.0	-11.541 ± 0.667	3.963 ± 1.014	-9.634 ± 0.537	-29.238 ± 0.797
6.0	-7.961 ± 0.471	-4.011 ± 0.715	-10.977 ± 0.380	-20.401 ± 0.563
7.0	-2.364 ± 0.667	-19.183 ± 1.014	-10.797 ± 0.537	-40.701 ± 0.797
8.0	223.444 ± 0.698	-379.082 ± 0.974	235.854 ± 2.454	-202.568 ± 3.976
9.0	103.824 ± 0.698	-165.079 ± 0.974	63.708 ± 2.454	-26.653 ± 3.976
10.0	140.546 ± 0.327	-231.093 ± 0.383	118.608 ± 0.574	-48.912 ± 0.573
11.0	-12.365 ± 0.385	28.101 ± 0.584	-5.590 ± 0.310	3.560 ± 0.460
12.0	-11.339 ± 0.471	22.494 ± 0.715	-1.118 ± 0.380	-1.102 ± 0.563
13.0	-6.583 ± 0.667	10.765 ± 1.014	0.532 ± 0.537	-2.897 ± 0.797

5.5 Magnetic Field Measured with Hall Probe while 1A Current in Coils

We have the measured values of the magnetic field distribution. The measurements at room temperature of the sextupole super conducting magnet are described in [Rea95, Cap03] and performed in CERN. The measurements at liquid helium temperature (4.2 K) in FERRARA were performed during the training [Cap03]. The aim of the measurements in CERN is to obtain the sextupole (Fourier) component of the magnetic field and the non sextupole components, if present.

Before measuring the field, the first step was to fix the sextupole magnet on the support and measure the coordinate geometry for describing the positions of the measured points with (x,y,z). This measurements were performed with a high precision numeric control machine shown in figure 5.16.

The magnetic field was measured by a single hall probe moved from one point to another by 3 numeric control axis. The probe was set for measuring vertical magnetic field. The magnet could be rotated to six different positions. The support was machined with high precision to obtain exactly 60 degrees each rotation. The angular precision of each rotation was fundamental for the measurement.

The field was measured after each rotation along x (horizontal in figure 5.1) and y (vertical) axes, from zero to four (or 4.5) centimeters, depending on the tapering of the inner bore. Along the z axis (corresponding to the geometrical axis) the field was measured at every 1 cm interval. The field was also measured at 7 cm outside the magnet on both sides, so that the strength of the fringing field could be obtained.

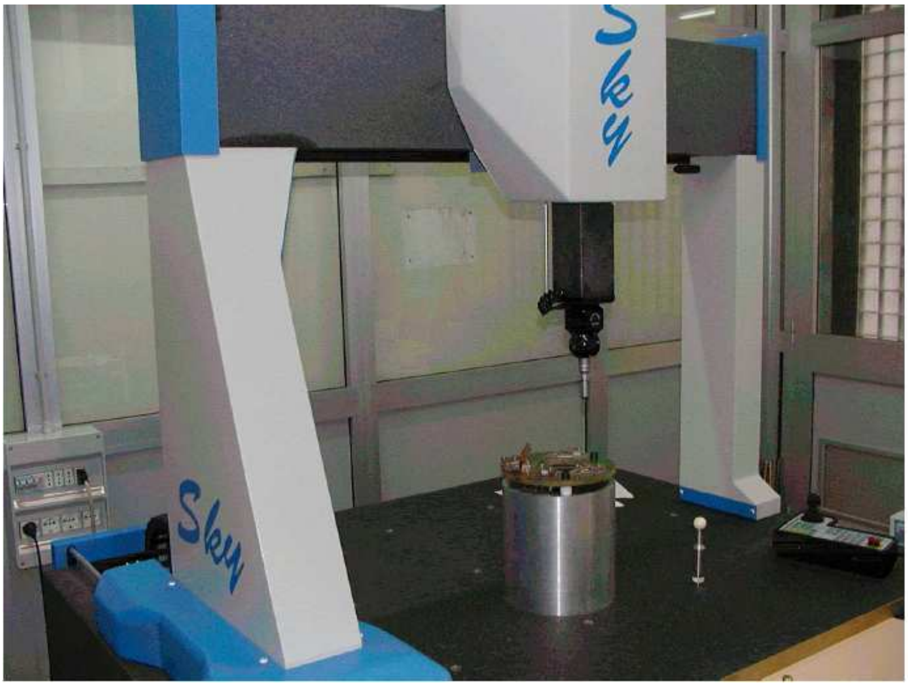

Figure 5.16: High precision numeric controlled machine for measuring the dimensions of the sextupole magnet

The measured results in CERN are listed in table 5.7 and 5.8. The fitting method is the same as ours. In fact we used the same code.

5.6 Magnetic Field Calculated with TOSCA with 1A in Coils

Beside the measured results, The HERMES group in FERRARA also performed some simulation of the sextupole magnet with TOSCA. The calculated results are list in table 5.9 and 5.10. The definition of the sign of $\vec{B}$ in the tables is opposite to the measured results. During the calculation with TOSCA, the μ of steel was taken as 1 like vacuum.

5.7 Summary of Magnetic Flux Density Results with 1A in Coils

With various series of K_n obtained by different methods, we plot the absolute value of $\vec{B_r}$ in figure 5.17. The black solid line is the measured result with Hall probe. The other three are calculated results. The MAFIA results with the contribution from steel layer include are shown with red dash line, while the blue dot line stands for the results without including such contribution by setting $\mu_{steel} = 1$. The green dash-dot line represents the TOSCA results calculated by HERMES group of FERRARA in Italy.

For the magnetic field measured with Hall probe, the values at the center region with z around $0\,cm$ inside the sextupole magnet are more reliable than the values outside (or nearly outside) the magnet. The reason is that the magnetic field is more sensitive to position coordinates

Table 5.7: Fitting results of K_1, K_2, K_3, and K_4 [gauss] for 1A current in coils measured with hall probe in CERN at the room temperature on each plane.

z(cm)	k1	k2	k3	k4
-18	-0.009±0.016	-0.021±0.058	-0.182±0.018	0.031±0.086
-17	-0.012±0.016	-0.021±0.058	-0.220±0.018	0.020±0.086
-16	-0.020±0.016	-0.011±0.058	-0.325±0.018	0.010±0.086
-15	-0.031±0.016	0.007±0.058	-0.558±0.018	0.015±0.086
-14	-0.045±0.016	0.024±0.058	-1.051±0.018	0.006±0.086
-13	-0.053±0.016	0.055±0.058	-2.068±0.018	-0.005±0.086
-12	-0.065±0.016	0.085±0.058	-4.225±0.018	-0.002±0.086
-11	-0.076±0.016	0.135±0.058	-8.972±0.018	-0.011±0.086
-10	-0.094±0.016	0.200±0.058	-19.234±0.018	-0.064±0.086
-9	-0.135 ± 0.016	0.297 ± 0.058	-37.355 ± 0.018	-0.228 ± 0.086
-8	-0.208 ± 0.016	0.393 ± 0.058	-61.262 ± 0.018	-0.385 ± 0.086
-7	-0.307 ± 0.016	0.492 ± 0.058	-87.604 ± 0.018	-0.480 ± 0.086
-6	-0.376 ± 0.016	0.594 ± 0.058	-107.221 ± 0.018	-0.643 ± 0.086
-5	-0.445 ± 0.016	0.748 ± 0.058	-115.873 ± 0.018	-0.814 ± 0.086
-4	-0.482 ± 0.016	0.871 ± 0.058	-119.946 ± 0.018	-0.966 ± 0.086
-3	-0.503 ± 0.016	0.972 ± 0.058	-122.524 ± 0.018	-1.070 ± 0.086
-2	-0.510 ± 0.020	1.228 ± 0.064	-125.585 ± 0.020	-1.080 ± 0.095
-1	-0.493 ± 0.020	1.318 ± 0.064	-127.610 ± 0.020	-1.135 ± 0.095
0	-0.462 ± 0.020	1.473 ± 0.064	-129.634 ± 0.020	-1.217 ± 0.095
1	-0.395 ± 0.017	1.113 ± 0.068	-130.405 ± 0.027	-0.468 ± 0.129
2	-0.349 ± 0.017	1.258 ± 0.068	-132.405 ± 0.027	-0.608 ± 0.129
3	-0.280 ± 0.017	1.428 ± 0.068	-134.478 ± 0.027	-0.697 ± 0.129
4	-0.222 ± 0.017	1.531 ± 0.068	-136.478 ± 0.027	-0.627 ± 0.129
5	-0.161 ± 0.017	1.720 ± 0.068	-138.430 ± 0.027	-0.688 ± 0.129
6	-0.110 ± 0.017	1.817 ± 0.068	-139.973 ± 0.027	-0.656 ± 0.129
7	-0.092 ± 0.017	1.867 ± 0.068	-140.166 ± 0.027	-0.444 ± 0.129
8	-0.096 ± 0.017	1.752 ± 0.068	-136.213 ± 0.027	-0.010 ± 0.129
9	-0.092 ± 0.017	1.544 ± 0.068	-119.319 ± 0.027	0.199 ± 0.129
10	-0.111 ± 0.017	1.435 ± 0.068	-88.592 ± 0.027	-0.580 ± 0.129
11	-0.116 ± 0.017	1.115 ± 0.068	-57.720 ± 0.027	-0.864 ± 0.129
12	-0.096 ± 0.017	0.797 ± 0.068	-30.101 ± 0.027	-1.057 ± 0.129
13	-0.069 ± 0.017	0.494 ± 0.068	-12.734 ± 0.027	-0.937 ± 0.129
14	-0.031 ± 0.017	0.245 ± 0.068	-5.350 ± 0.027	-0.561 ± 0.129
15	-0.003 ± 0.017	0.105 ± 0.068	-2.385 ± 0.027	-0.293 ± 0.129
16	0.017 ± 0.017	0.054 ± 0.068	-1.127 ± 0.027	-0.176 ± 0.129
17	0.017 ± 0.017	0.063 ± 0.068	-0.571 ± 0.027	-0.150 ± 0.129
18	0.003 ± 0.017	0.059 ± 0.068	-0.388 ± 0.027	-0.028 ± 0.129

around the pole's end than that at the center. Comparing the figure 5.18 and figure 5.19, we can see the relative values of the magnetic field at X-Y plane, where $z = -12.4\,cm$, changing much more than that in the plane where $z = 0.1\,cm$. Same results can be obtained for the magnetic field distribution in X-Z plane (see figure 5.20), and Y-Z plane (figure 5.21). When measuring magnetic field at the region outside the pole, little miss-alignment will cause a bigger error in the outside region than that in the center.

Table 5.8: Fitting results of K_5, K_6, K_9, and K_{12} [gauss] for 1A current in coils measured with hall probe in CERN at the room temperature on each plane.

z(cm)	k5	k6	k9	k12
-18	-0.016±0.045	-0.058±0.149	0.000±0.002	0.000±0.000
-17	-0.025±0.045	-0.135±0.149	0.001±0.002	0.000±0.000
-16	-0.025±0.045	-0.242±0.149	0.005±0.002	0.000±0.000
-15	-0.040±0.045	-0.428±0.149	0.012±0.002	0.000±0.000
-14	-0.027±0.045	-0.497±0.149	0.023±0.002	0.000±0.000
-13	-0.016±0.045	-0.597±0.149	0.046±0.002	0.000±0.000
-12	0.040±0.045	-0.648±0.149	0.089±0.002	0.000±0.000
-11	0.202±0.045	-0.547±0.149	0.148±0.002	0.000±0.000
-10	0.624±0.045	-0.281±0.149	0.151±0.002	0.000±0.000
-9	1.282±0.045	-0.097±0.149	0.034±0.002	0.000±0.000
-8	2.011±0.045	-0.137±0.149	-0.141±0.002	0.000±0.000
-7	2.601±0.045	-0.455±0.149	-0.525±0.002	0.000±0.000
-6	2.409±0.045	-0.904±0.149	-0.754±0.002	0.000±0.000
-5	2.227±0.045	-1.168±0.149	-0.627±0.002	0.000±0.000
-4	2.132±0.045	-0.981±0.149	-0.539±0.002	0.000±0.000
-3	2.021±0.045	-0.804±0.149	-0.520±0.002	0.000±0.000
-2	2.327±0.058	0.789±0.166	-0.568±0.002	-0.001±0.000
-1	2.148±0.058	1.359±0.166	-0.601±0.002	-0.002±0.000
0	1.995±0.058	2.468±0.166	-0.641±0.002	-0.002±0.000
1	1.731±0.080	0.424±0.405	-0.726±0.004	-0.001±0.000
2	1.569±0.080	1.411±0.405	-0.778±0.004	-0.002±0.000
3	1.297±0.080	1.541±0.405	-0.843±0.004	-0.002±0.000
4	1.151±0.080	1.799±0.405	-0.908±0.004	-0.002±0.000
5	0.899±0.080	2.658±0.405	-1.005±0.004	-0.003±0.000
6	0.651±0.080	3.005±0.405	-1.150±0.004	-0.003±0.000
7	0.600±0.080	3.643±0.405	-1.420±0.004	-0.003±0.000
8	0.368±0.080	3.532±0.405	-1.867±0.004	-0.002±0.000
9	-0.838±0.080	2.605±0.405	-1.661±0.004	-0.002±0.000
10	-1.206±0.080	0.866±0.405	-0.618±0.004	-0.001±0.000
11	-1.241±0.080	0.123±0.405	-0.255±0.004	0.000±0.000
12	-1.244±0.080	0.070±0.405	0.162±0.004	0.000±0.000
13	-0.635±0.080	0.113±0.405	0.356±0.004	0.000±0.000
14	-0.178±0.080	0.007±0.405	0.213±0.004	0.000±0.000
15	0.025±0.080	-0.271±0.405	0.092±0.004	0.000±0.000
16	0.117±0.080	-0.675±0.405	0.032±0.004	0.001±0.000
17	0.165±0.080	-0.978±0.405	0.008±0.004	0.001±0.000
18	0.099±0.080	-0.843±0.405	0.000±0.004	0.001±0.000

Table 5.9: Fitting results of K_1, K_2, K_3, and K_4[gauss] for 1A current in coils calculated with TOSCA.

z(cm)	k1	k2	k3	k4
-15	-0.0325±0.0240	0.0996±0.1325	1.7510±0.3527	1.2330±1.0460
-14	-0.0433±0.0240	0.1923±0.1325	2.7330±0.3527	2.0390±1.0460
-13	-0.0970±0.0240	0.3011±0.1325	5.7130±0.3527	2.9590±1.0460
-12	-0.0773±0.0240	0.5635±0.1325	15.8200±0.3527	3.6750±1.0460
-11	-0.0489±0.0240	0.3839±0.1325	32.5700±0.3527	1.4350±1.0460
-10	-0.0275±0.0240	0.0908±0.1325	54.6400±0.3527	-0.4666±1.0460
-9	0.0727±0.0240	-0.1901±0.1325	80.9000±0.3527	-1.4680±1.0460
-8	0.2053±0.0240	-0.4960±0.1325	104.2000±0.3527	-4.0080±1.0460
-7	0.2681±0.0240	-0.0282±0.1325	120.7000±0.3527	2.3840±1.0460
-6	0.1599±0.0240	-0.4518±0.1325	123.4000±0.3527	-3.7680±1.0460
-5	0.2412±0.0240	0.4717±0.1325	123.8000±0.3527	4.5270±1.0460
-4	0.1189±0.0240	0.7711±0.1325	116.7000±0.3527	5.6560±1.0460
-3	0.0479±0.0240	-0.1053±0.1325	106.5000±0.3527	-4.2820±1.0460
-2	0.1031±0.0240	0.2645±0.1325	102.2000±0.3527	1.3780±1.0460
-1	0.0437±0.0240	0.1851±0.1325	95.7300±0.3527	2.4790±1.0460
0	0.1581±0.0223	0.9764±0.1096	94.9800±0.2589	11.2400±0.6783
1	0.1506±0.0223	0.9504±0.1096	91.4400±0.2589	9.2510±0.6783
2	0.1484±0.0223	0.7376±0.1096	88.5000±0.2589	6.9620±0.6783
3	0.1530±0.0223	0.7791±0.1096	86.5000±0.2589	6.6010±0.6783
4	0.1389±0.0223	0.5459±0.1096	83.6900±0.2589	4.2510±0.6783
5	0.1183±0.0223	0.2284±0.1096	80.7000±0.2589	2.5230±0.6783
6	0.1395±0.0223	-0.0739±0.1096	77.1200±0.2589	0.1922±0.6783
7	0.1649±0.0223	-0.3816±0.1096	72.0200±0.2589	-1.0890±0.6783
8	0.1181±0.0223	-0.0485±0.1096	63.0200±0.2589	1.3890±0.6783
9	0.0449±0.0223	0.0440±0.1096	50.3800±0.2589	0.4925±0.6783
10	-0.0336±0.0223	0.6375±0.1096	37.4000±0.2589	4.6810±0.6783
11	-0.1315±0.0223	0.9053±0.1096	24.1800±0.2589	5.5620±0.6783
12	-0.1009±0.0223	-0.2220±0.1096	14.1400±0.2589	-2.5240±0.6783
13	-0.0996±0.0223	0.3257±0.1096	9.0170±0.2589	2.2010±0.6783
14	-0.0789±0.0223	0.2724±0.1096	6.2540±0.2589	2.1340±0.6783
15	-0.0747±0.0223	0.1837±0.1096	5.1090±0.2589	1.5800±0.6783

Table 5.10: Fitting results of K_5, K_6, K_9, and K_{12}[gauss] for 1A current in coils calculated with TOSCA.

z(cm)	k5	k6	k9	k12
-15.0	2.3450±1.1220	0.4204±1.8980	0.2562±1.8970	-3.6620±1.9030
-14.0	3.7120±1.1220	0.6829±1.8980	0.5146±1.8970	-5.8120±1.9030
-13.0	6.5750±1.1220	-1.3990±1.8980	3.3770±1.8970	-15.2600±1.9030
-12.0	13.4700±1.1220	-11.0400±1.8980	12.7800±1.8970	-41.4500±1.9030
-11.0	13.4000±1.1220	-14.5400±1.8980	5.2560±1.8970	-48.6700±1.9030
-10.0	1.2700±1.1220	-4.6950±1.8980	8.3310±1.8970	-18.2400±1.9030
-9.0	-3.7830±1.1220	12.4300±1.8980	-19.2800±1.8970	35.6400±1.9030
-8.0	-7.5920±1.1220	25.8700±1.8980	-31.7700±1.8970	42.6100±1.9030
-7.0	-6.7150±1.1220	67.2500±1.8980	-43.5200±1.8970	32.3000±1.9030
-6.0	-16.5900±1.1220	56.9600±1.8980	0.8298±1.8970	-3.7120±1.9030
-5.0	-3.2280±1.1220	59.8200±1.8980	-0.6088±1.8970	16.1800±1.9030
-4.0	6.6720±1.1220	43.1500±1.8980	-22.7100±1.8970	11.9800±1.9030
-3.0	-0.8128±1.1220	-2.4370±1.8980	8.8620±1.8970	-8.1920±1.9030
-2.0	9.7060±1.1220	-5.3000±1.8980	4.7070±1.8970	-24.2200±1.9030
-1.0	7.2050±1.1220	-0.0304±1.8980	-5.7630±1.8970	-3.8560±1.9030
0.0	16.8200±0.6531	18.4900±0.9601	-25.4900±0.6809	12.8100±0.4432
1.0	13.0500±0.6531	15.5900±0.9602	-21.9100±0.6809	11.9300±0.4432
2.0	10.1000±0.6531	12.3100±0.9602	-18.3600±0.6809	10.4000±0.4432
3.0	9.1360±0.6531	11.2700±0.9602	-16.1200±0.6809	9.2540±0.4432
4.0	6.3180±0.6531	8.1510±0.9602	-13.0700±0.6809	7.9210±0.4432
5.0	3.9080±0.6531	6.7160±0.9602	-11.2800±0.6809	7.6920±0.4432
6.0	0.6816±0.6531	4.9870±0.9602	-9.9940±0.6809	8.0630±0.4432
7.0	-1.4400±0.6531	6.9280±0.9602	-11.9900±0.6809	11.2100±0.4432
8.0	-2.3140±0.6531	11.8900±0.9602	-15.1200±0.6809	12.8300±0.4432
9.0	-4.2950±0.6531	5.6590±0.9602	-7.5720±0.6809	6.9990±0.4432
10.0	0.4966±0.6531	8.0690±0.9602	-8.2430±0.6809	1.0060±0.4432
11.0	2.5030±0.6531	5.0680±0.9602	-8.3250±0.6809	-3.1350±0.4432
12.0	-0.9859±0.6531	-5.4710±0.9602	0.5125±0.6809	-4.6640±0.4432
13.0	3.1200±0.6531	-0.3632±0.9602	1.0540±0.6809	-4.0070±0.4432
14.0	2.9340±0.6531	0.3705±0.9602	0.6751±0.6809	-2.6380±0.4432
15.0	2.2430±0.6531	-0.0949±0.9602	1.0250±0.6809	-2.3010±0.4432

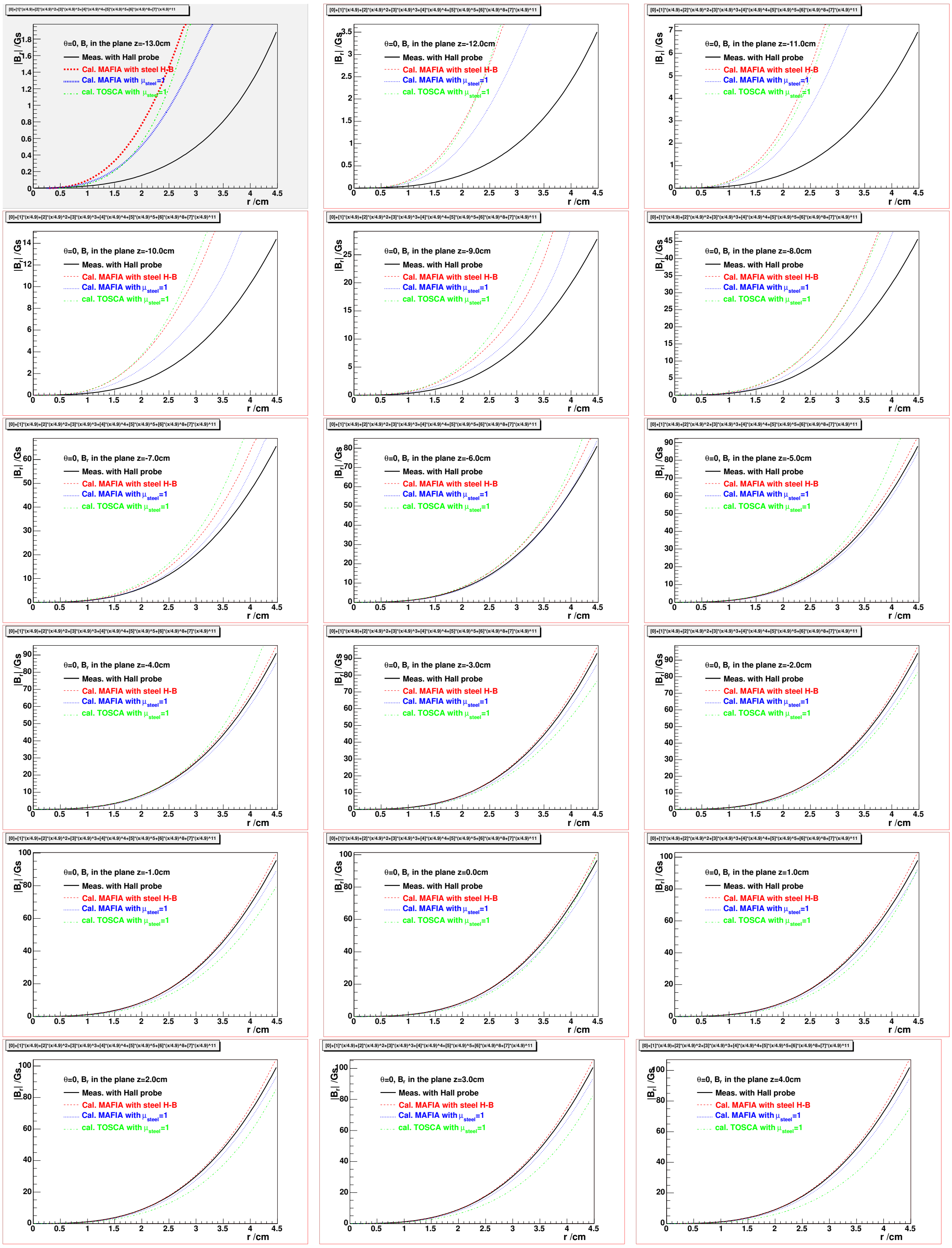

to be continued · · ·

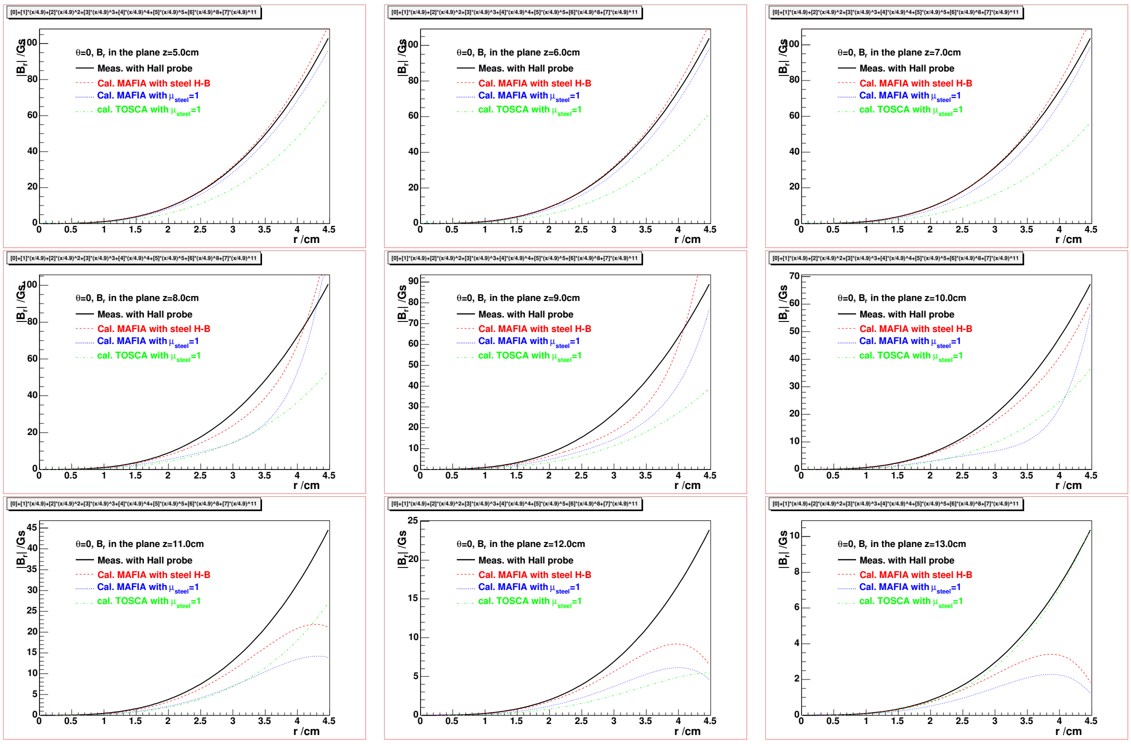

Figure 5.17: Plots of $\vec{B}_r$ calculated(measured) with the K_n results from different methods: MAFIA, TOSCA, Hall probe. The fitting function is $B_r = \sum_n K_n \left(\frac{r}{r_M}\right)^{n-1} \cos(n\theta)$, while keep $r_M = 4.9\,cm$, $\theta = 0$ and $n = 1, 2, 3, 4, 5, 6, 9$ and 12 . The plots in the first row from left to right come from the data in $z = -13\,cm$, $z = -12\,cm$ and $z = -11\,cm$ planes; The data in the second row are from planes $z = -10\,cm$, $z = -9\,cm$ and $z = -8\,cm$; $\ldots$; the last row for planes $z = 11\,cm$, $z = 12\,cm$ and $z = 13\,cm$. Black solid line for the measured results with Hall probe in CERN; Green dash-dot line for calculated results with TOSCA; Red dash-dash line for the MAFIA results using H-B curve describing the property of steel layers and red dash-dot line for the MAFIA results using $\mu_{steel} = 1$ describing the property of steel layers. $(I = 1$ A)

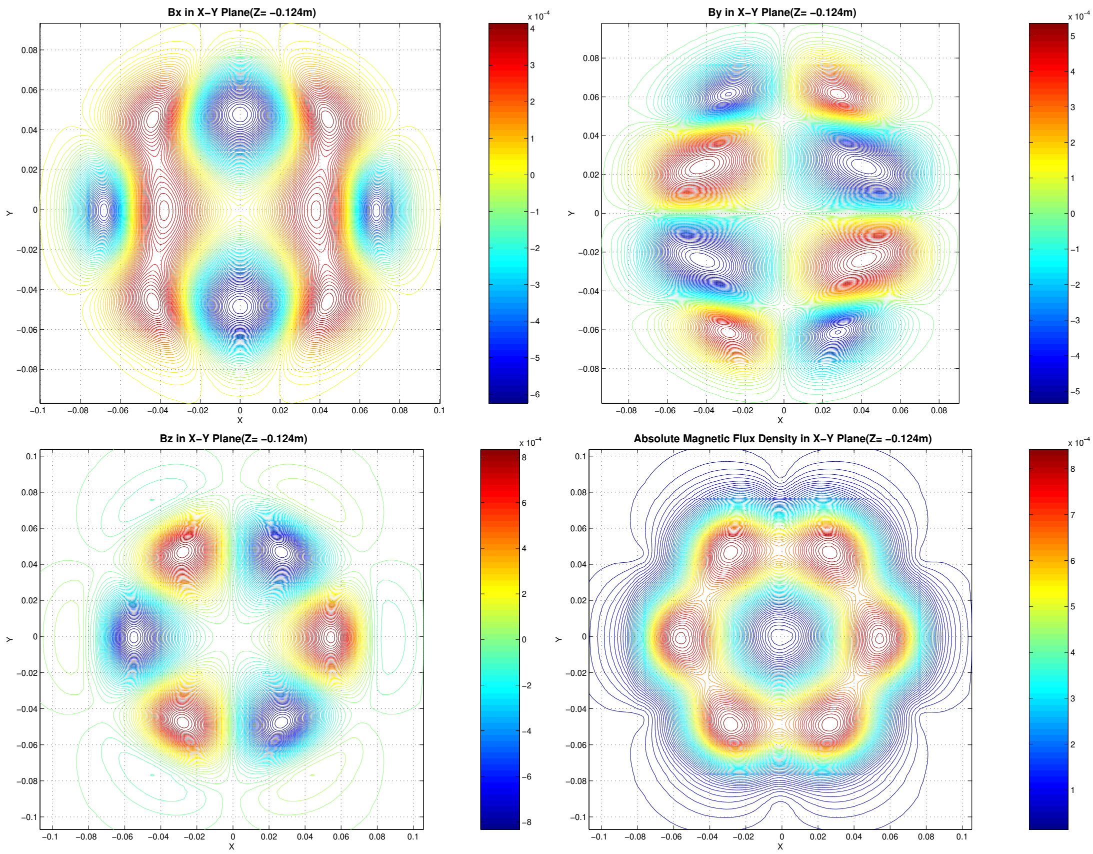

Figure 5.18: The distribution of $\vec{B}_x$(left up), $\vec{B}_y$(right up), $\vec{B}_z$(left down) and absolute magnetic flux density $\left|\vec{B}\right|$(right down) in X-Y plane where $z = -12.4\,cm$. $\left|\vec{B}\right| = \sqrt{\vec{B}_x^2 + \vec{B}_y^2 + \vec{B}_z^2}$. Using $\mu_{steel} = 1$ describing the property of steel layers.($I = 1$ A; Units of x-, y- axis: m; B: T)

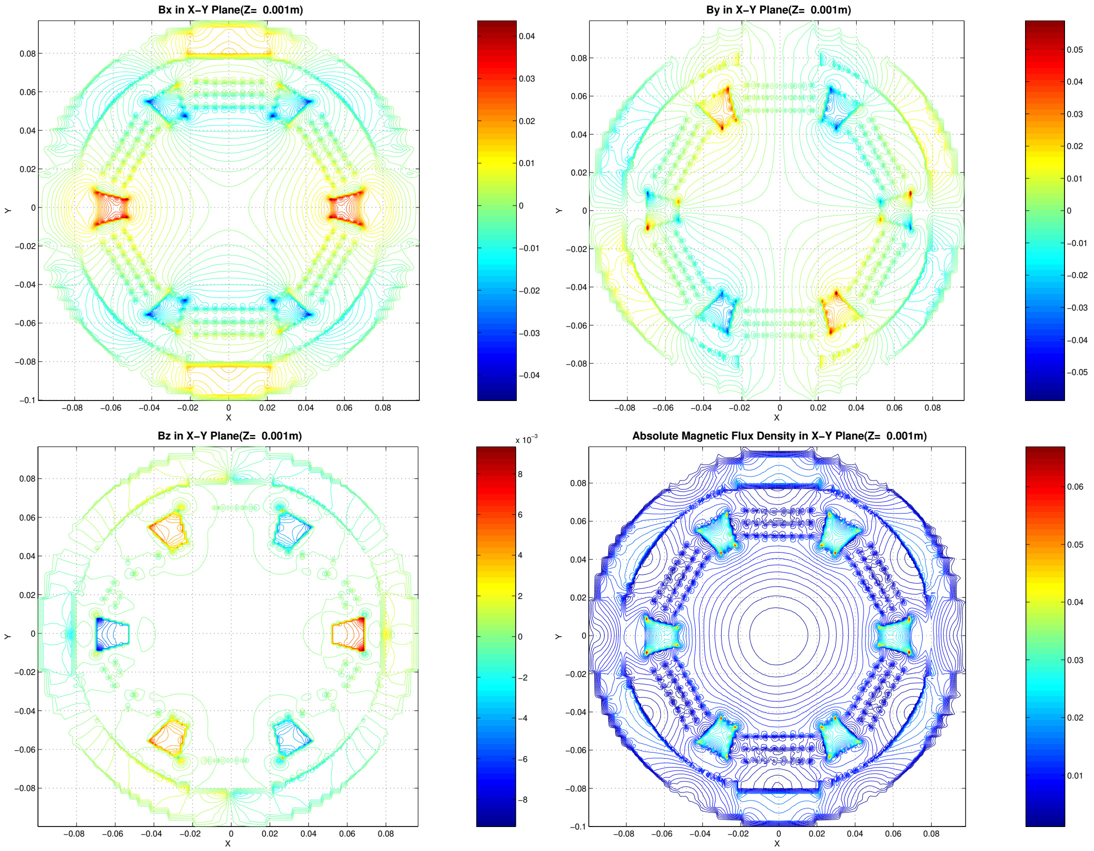

Figure 5.19: The distribution of $\vec{B}_x$(left up), $\vec{B}_y$(right up), $\vec{B}_z$(left down) and absolute magnetic flux density $\left|\vec{B}\right|$(right down) in X-Y plane where $z = 0.1\,cm$. $\left|\vec{B}\right| = \sqrt{\vec{B}_x^2 + \vec{B}_y^2 + \vec{B}_z^2}$. Using $\mu_{steel} = 1$ describing the property of steel layers. ($I = 1$ A; Units of x-, y- axis: m; B: T)

The reason for the disagreement between the measured results and calculated results maybe come from the different shapes in coils' circling in MAFIA and the actual shape at pole's end besides the systematic errors in measured results due to miss-alignment.

But the agreement between the calculated results with MAFIA and the measured results with Hall probe at center region, that is the most important place, gives us confidence about the geometry description. We will increase the current to 517A to calculate the magnetic flux density distribution to compare with the measured results with high currents.

5.8 Magnetic Flux Density with 517A in Coils

When the magnet was trained in HERMES group of FERRARA, a probe was placed near the inner surface of the pole, at $r = 5.20\,cm$. The coordinate (x,y,z) of the measured position corresponding to our model used in MAFIA calculation is (5.20, 0.00, 0.26) cm. When the

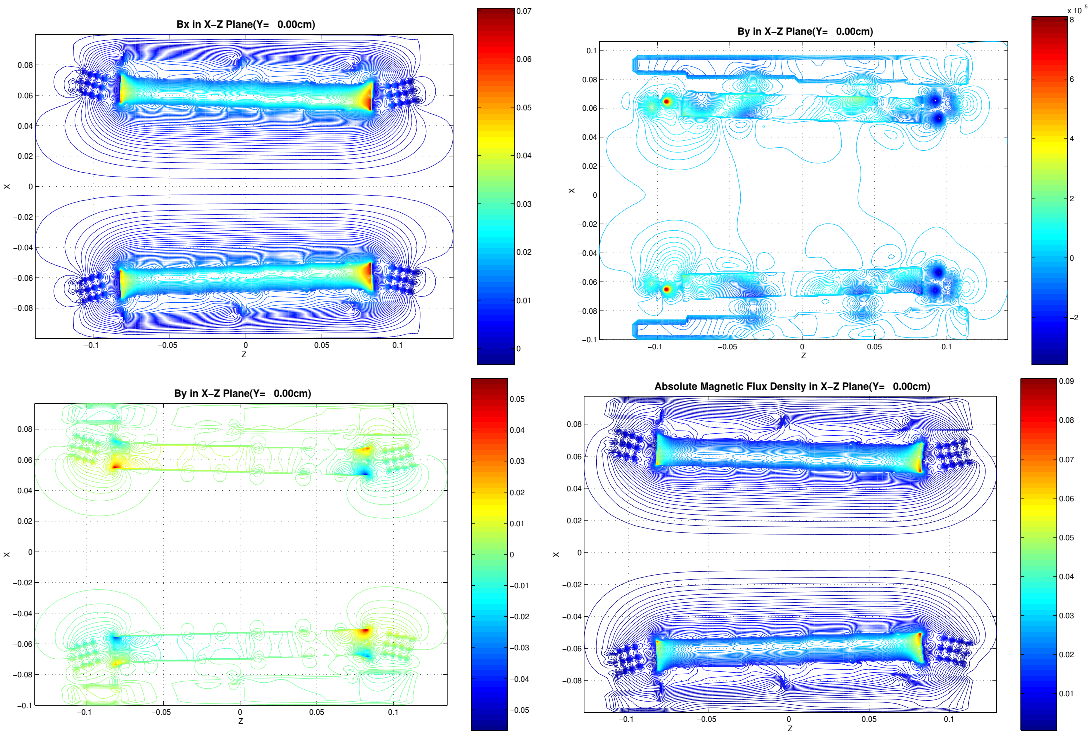

Figure 5.20: The distribution of $\vec{B}_x$(left up), $\vec{B}_y$(right up), $\vec{B}_z$(left down) and absolute magnetic flux density $\left|\vec{B}\right|$(right down) in X-Z plane, where $Y = 0.0\,cm$.$\left|\vec{B}\right| = \sqrt{\vec{B}_x^2 + \vec{B}_y^2 + \vec{B}_z^2}$. Using $\mu_{steel} = 1$ describing the property of steel layers.($I = 1$ A; Units of x-, z- axis: m; B: T)

current is increased and reaches $517A$, which is the maximum value during the training, the field measured by this probe is $4.8T$[Cap03]. This value is of the component $\vec{B}_x$.

For testing whether our model can work in such high current, we have performed two calculations with current equal to $517A$. One is to use the H-B curve shown in figure 5.15 describing the material property of the steel layer. The results are shown in figure 5.22 and the data are listed in table 5.11; The other is to use the relative permeability $\mu_{steel} = 1$ describing the steel layer, the results are shown figure 5.23 and the data selected from this plot are listed in table 5.12. Due to the size of the mesh can not be infinitely small, we only have the data in the planes which pass through $z = 0.07\,cm$ and $z = 0.37\,cm$ in the plots and tables.The data are selected by:

- $|z - 0.26| < 0.2\,cm$
- $|y| < 0.1\,cm$
- $1.0\,cm < x \leq 5.2\,cm$

Since $\left|\sqrt{\vec{B}_x^2 + \vec{B}_y^2}\right| \propto r^2$, for the measured result, the uncertainty in the radial position of the probe center is a significant factor. The position of the support with respect to the magnet

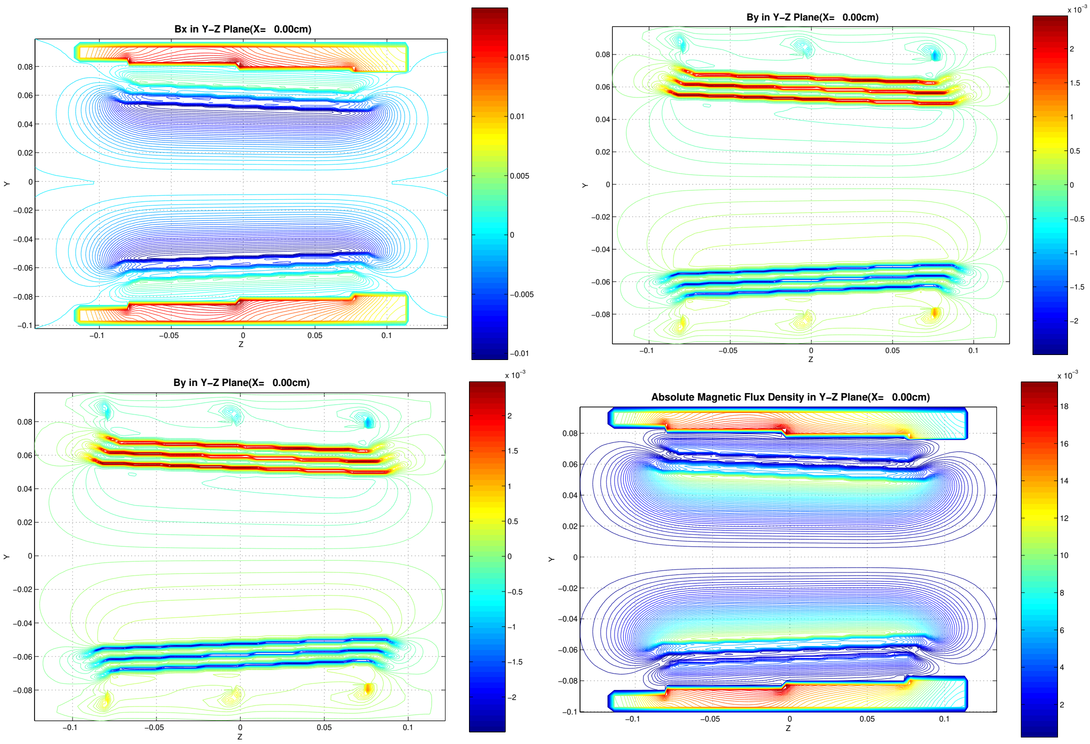

Figure 5.21: The distribution of $\vec{B}_x$(left up), $\vec{B}_y$(right up), $\vec{B}_z$(left down) and absolute magnetic flux density $\left|\vec{B}\right|$(right down) in Y-Z plane, where $X = 0.0\,cm$. $\left|\vec{B}\right| = \sqrt{\vec{B}_x^2 + \vec{B}_y^2 + \vec{B}_z^2}$. Using $\mu_{steel} = 1$ describing the property of steel layers.($I = 1$ A; Units of y-, z- axis: m; B: T)

axis is $\pm 1mm$. For the probe, the position error is $\pm\frac{1}{3}mm$[Giu02]. Considering the position errors, which will introduce an error around $\pm 0.2\,T$, we can have a conclusion by comparing the measured result as 4.8 ± 0.2 T at (5.20, 0.00, 0.26) cm with the MAFIA results listed in table 5.11 and table 5.12: **The results of MAFIA agree with the measured values very well within the experimental error ± 0.2 T!**

5.9 Magnetic Field Information with I=500A Provided for Simulation

Before simulating trajectories of atoms inside sextupole magnets, the magnetic flux density distribution must be provided. The relationship between the force on the atoms from the field and the filed distributions are presented here.

5.9.1 Formulations of Trajectories in Sextupole Magnets

Before this work, many simulation works have been performed on the trajectories of atoms passing through the sextupole magnet in HERMES ABS. The magnets are permanent magnets

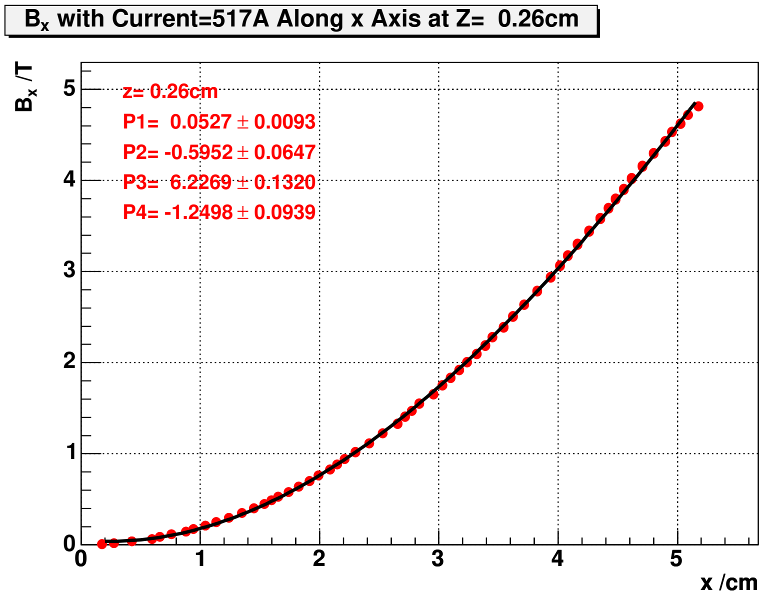

Figure 5.22: $\vec{B}_x$ changing with x along x-axis in $z = 0.26\,cm$ plane. The current in coils equals 517A. Using H-B curve in table 5.2 describing the magnetic property of the steel layer. The fitting function is $B_x\,(x) = \sum_{n=1}^{4} P_n\left(\frac{r}{4.9}\right)^{(n-1)}$. $(I = 517\text{ A})$

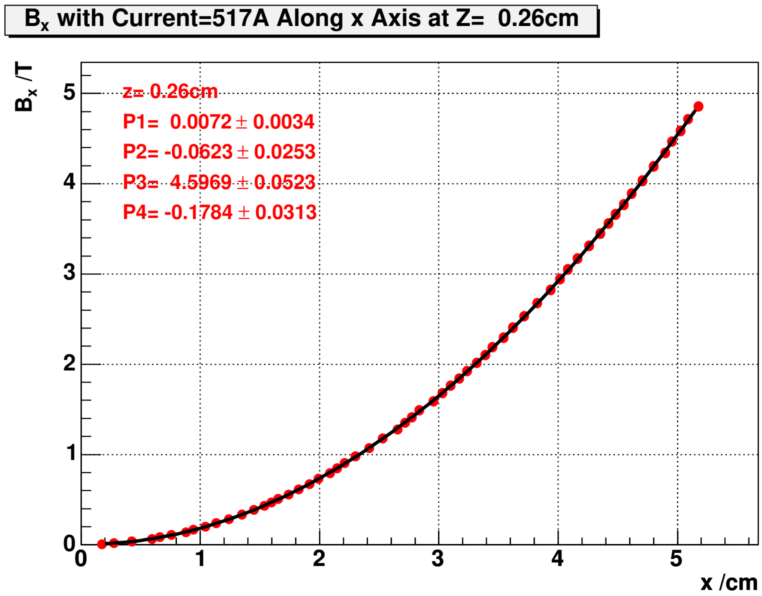

Figure 5.23: $\vec{B}_x$ changing with x along x-axis in $z = 0.26\,cm$ plane. The current in coils equals 517A. Using $\mu_{steel} = 1$ to describe the steel layer. The fitting function is $B_x\,(x) = \sum_{n=1}^{4} P_n\left(\frac{r}{4.9}\right)^{(n-1)}$. $(I = 517\text{ A})$

made from a NdFeB alloy. The field distribution within this sextupole magnet can be calculated

Table 5.11: MAFIA results about $\vec{B}_x$, $\vec{B}_y$ and $\vec{B}_z$ values at different points along x-axis when I=517A with H-B curve describing the steel layer

x(cm)	y(cm)	z(cm)	r(cm)	$\vec{B}_x$ (T)	$\vec{B}_y$(T)	$\vec{B}_z$(T)	x(cm)	y(cm)	z(cm)	r(cm)	$\vec{B}_x$ (T)	$\vec{B}_y$(T)	$\vec{B}_z$(T)
0.18	0.00	0.07	0.1800	0.0081	0.0000	-0.0001	0.18	0.00	0.37	0.1800	0.0079	0.0000	-0.0001
0.28	0.00	0.07	0.2800	0.0193	0.0000	-0.0002	0.28	0.00	0.37	0.2800	0.0192	0.0000	-0.0002
0.43	0.00	0.07	0.4300	0.0388	0.0000	-0.0002	0.43	0.00	0.37	0.4300	0.0387	0.0000	-0.0002
0.60	0.00	0.07	0.6000	0.0651	0.0000	-0.0002	0.60	0.00	0.37	0.6000	0.0652	0.0000	-0.0002
0.66	0.00	0.07	0.6600	0.0886	0.0000	-0.0001	0.66	0.00	0.37	0.6600	0.0888	0.0000	-0.0002
0.76	0.00	0.07	0.7600	0.1146	0.0000	0.0000	0.76	0.00	0.37	0.7600	0.1148	0.0000	0.0000
0.88	0.00	0.07	0.8800	0.1456	0.0000	0.0001	0.88	0.00	0.37	0.8800	0.1460	0.0000	0.0001
0.94	0.00	0.07	0.9400	0.1753	0.0000	0.0003	0.94	0.00	0.37	0.9400	0.1758	0.0000	0.0002
1.04	0.00	0.07	1.0400	0.2088	0.0000	0.0005	1.04	0.00	0.37	1.0400	0.2095	0.0000	0.0004
1.13	0.00	0.07	1.1300	0.2491	0.0000	0.0008	1.13	0.00	0.37	1.1300	0.2500	0.0000	0.0007
1.24	0.00	0.07	1.2400	0.2958	0.0000	0.0012	1.24	0.00	0.37	1.2400	0.2968	0.0000	0.0011
1.35	0.00	0.07	1.3500	0.3483	0.0000	0.0017	1.35	0.00	0.37	1.3500	0.3496	0.0000	0.0016
1.45	0.00	0.07	1.4500	0.4011	0.0000	0.0021	1.45	0.00	0.37	1.4500	0.4026	0.0000	0.0020
1.54	0.00	0.07	1.5400	0.4482	0.0000	0.0026	1.54	0.00	0.37	1.5400	0.4499	0.0000	0.0024
1.60	0.00	0.07	1.6000	0.4874	0.0000	0.0029	1.60	0.00	0.37	1.6000	0.4893	0.0000	0.0028
1.65	0.00	0.07	1.6500	0.5277	0.0000	0.0034	1.65	0.00	0.37	1.6500	0.5298	0.0000	0.0033
1.74	0.00	0.07	1.7400	0.5785	0.0000	0.0041	1.74	0.00	0.37	1.7400	0.5808	0.0000	0.0039
1.83	0.00	0.07	1.8300	0.6373	0.0000	0.0049	1.83	0.00	0.37	1.8300	0.6398	0.0000	0.0047
1.92	0.00	0.07	1.9200	0.6982	0.0000	0.0057	1.92	0.00	0.37	1.9200	0.7011	0.0000	0.0055
1.99	0.00	0.07	1.9900	0.7610	0.0000	0.0065	1.99	0.00	0.37	1.9900	0.7641	0.0000	0.0063
2.09	0.00	0.07	2.0900	0.8244	0.0000	0.0074	2.09	0.00	0.37	2.0900	0.8277	0.0000	0.0072
2.15	0.00	0.07	2.1500	0.8808	0.0000	0.0082	2.15	0.00	0.37	2.1500	0.8844	0.0000	0.0079
2.21	0.00	0.07	2.2100	0.9385	0.0000	0.0092	2.21	0.00	0.37	2.2100	0.9423	0.0000	0.0089
2.30	0.00	0.07	2.3000	1.0157	0.0000	0.0106	2.30	0.00	0.37	2.3000	1.0199	0.0000	0.0104
2.42	0.00	0.07	2.4200	1.1127	0.0000	0.0124	2.42	0.00	0.37	2.4200	1.1173	0.0000	0.0121
2.53	0.00	0.07	2.5300	1.2218	0.0000	0.0145	2.53	0.00	0.37	2.5300	1.2269	0.0000	0.0141
2.65	0.00	0.07	2.6500	1.3265	0.0000	0.0162	2.65	0.00	0.37	2.6500	1.3321	0.0000	0.0158
2.72	0.00	0.07	2.7200	1.4048	0.0000	0.0174	2.72	0.00	0.37	2.7200	1.4107	0.0000	0.0170
2.77	0.00	0.07	2.7700	1.4667	0.0000	0.0186	2.77	0.00	0.37	2.7700	1.4729	0.0000	0.0182
2.84	0.00	0.07	2.8400	1.5469	0.0000	0.0206	2.84	0.00	0.37	2.8400	1.5535	0.0000	0.0202
2.96	0.00	0.07	2.9600	1.6505	0.0000	0.0229	2.96	0.00	0.37	2.9600	1.6575	0.0001	0.0224
3.03	0.00	0.07	3.0300	1.7466	0.0000	0.0247	3.03	0.00	0.37	3.0300	1.7541	0.0001	0.0242
3.10	0.00	0.07	3.1000	1.8303	0.0000	0.0266	3.10	0.00	0.37	3.1000	1.8381	0.0001	0.0261
3.17	0.00	0.07	3.1700	1.9137	0.0001	0.0284	3.17	0.00	0.37	3.1700	1.9219	0.0001	0.0279
3.24	0.00	0.07	3.2400	1.9997	0.0001	0.0305	3.24	0.00	0.37	3.2400	2.0084	0.0001	0.0300
3.32	0.00	0.07	3.3200	2.0920	0.0001	0.0328	3.32	0.00	0.37	3.3200	2.1011	0.0001	0.0323
3.39	0.00	0.07	3.3900	2.1821	0.0001	0.0349	3.39	0.00	0.37	3.3900	2.1916	0.0001	0.0344
3.45	0.00	0.07	3.4500	2.2748	0.0001	0.0374	3.45	0.00	0.37	3.4500	2.2848	0.0001	0.0369
3.54	0.00	0.07	3.5400	2.3831	0.0001	0.0403	3.54	0.00	0.37	3.5400	2.3936	0.0001	0.0399
3.62	0.00	0.07	3.6200	2.5004	0.0001	0.0435	3.62	0.00	0.37	3.6200	2.5114	0.0001	0.0430
3.72	0.00	0.07	3.7200	2.6303	0.0001	0.0473	3.72	0.00	0.37	3.7200	2.6420	0.0001	0.0469
3.82	0.00	0.07	3.8200	2.7807	0.0001	0.0517	3.82	0.00	0.37	3.8200	2.7931	0.0002	0.0514
3.94	0.00	0.07	3.9400	2.9317	0.0001	0.0556	3.94	0.00	0.37	3.9400	2.9448	0.0002	0.0555
4.02	0.00	0.07	4.0200	3.0574	0.0001	0.0588	4.02	0.00	0.37	4.0200	3.0710	0.0002	0.0588
4.08	0.00	0.07	4.0800	3.1673	0.0002	0.0620	4.08	0.00	0.37	4.0800	3.1813	0.0002	0.0622
4.16	0.00	0.07	4.1600	3.2916	0.0002	0.0660	4.16	0.00	0.37	4.1600	3.3061	0.0002	0.0664
4.26	0.00	0.07	4.2600	3.4352	0.0002	0.0704	4.26	0.00	0.37	4.2600	3.4502	0.0002	0.0711
4.35	0.00	0.07	4.3500	3.5737	0.0002	0.0741	4.35	0.00	0.37	4.3500	3.5890	0.0002	0.0752
4.42	0.00	0.07	4.4200	3.6878	0.0002	0.0770	4.42	0.00	0.37	4.4200	3.7032	0.0003	0.0784
4.48	0.00	0.07	4.4800	3.7892	0.0002	0.0800	4.48	0.00	0.37	4.4800	3.8047	0.0003	0.0817
4.55	0.00	0.07	4.5500	3.8950	0.0002	0.0831	4.55	0.00	0.37	4.5500	3.9103	0.0003	0.0851
4.62	0.00	0.07	4.6200	4.0128	0.0002	0.0867	4.62	0.00	0.37	4.6200	4.0277	0.0003	0.0890
4.71	0.00	0.07	4.7100	4.1480	0.0002	0.0906	4.71	0.00	0.37	4.7100	4.1621	0.0003	0.0933
4.80	0.00	0.07	4.8000	4.2927	0.0002	0.0944	4.80	0.00	0.37	4.8000	4.3054	0.0003	0.0972
4.90	0.00	0.07	4.9000	4.4233	0.0002	0.0974	4.90	0.00	0.37	4.9000	4.4340	0.0003	0.1000
4.96	0.00	0.07	4.9600	4.5279	0.0002	0.0997	4.96	0.00	0.37	4.9600	4.5364	0.0004	0.1018
5.03	0.00	0.07	5.0300	4.6207	0.0003	0.1019	5.03	0.00	0.37	5.0300	4.6271	0.0004	0.1032
5.09	0.00	0.07	5.0900	4.7156	0.0003	0.1041	5.09	0.00	0.37	5.0900	4.7195	0.0004	0.1041
5.18	0.00	0.07	5.1800	**4.8120**	0.0002	0.1064	**5.18**	0.00	0.37	5.1800	**4.8138**	0.0004	0.1046

using [Hal80]:

$$B(r) \equiv \left|\vec{B}(r)\right| = \frac{3}{2}J\left(\frac{r}{r_{pt}}\right)^2\left[1-\left(\frac{r_{pt}}{r_a}\right)^2\right]\frac{\sin(4\pi\varepsilon/M)}{4\pi/M} \tag{5.1}$$

J describes the magnetization, that is to say, the remanent magnetic field, r_{pt} the internal radius, (also called the pole tip radius), r_a the external radius, M the number of segments which comprise the magnets. The filling factor ε, which accounts for slits between the segments required for gluing, is close to 1[Bra95, vas00].

For simplicity, assuming the value of the field rises quadratically with the distance r from the magnetic axis, the field gradient is proportional to r:

$$B(r) = B_{pt} \cdot \frac{r^2}{r_{pt}^2} \qquad \frac{\partial B(r)}{\partial r} = 2B_{pt} \cdot \frac{r}{r_{pt}^2} \tag{5.2}$$

Table 5.12: MAFIA results about $\vec{B}_x$, $\vec{B}_y$ and $\vec{B}_z$ values at different points along x-axis when I=517A with $\mu_{steel} = 1$ describing the steel layer

x(cm)	y(cm)	z(cm)	r(cm)	$\vec{B}_x$ (T)	$\vec{B}_y$(T)	$\vec{B}_z$(T)	x(cm)	y(cm)	z(cm)	r(cm)	$\vec{B}_x$ (T)	$\vec{B}_y$(T)	$\vec{B}_z$(T)
0.18	0.00	0.07	0.18	0.0076	0.0000	-0.0001	0.18	0.00	0.37	0.18	0.0074	0.0000	-0.0001
0.28	0.00	0.07	0.28	0.0183	0.0000	-0.0002	0.28	0.00	0.37	0.28	0.0182	0.0000	-0.0002
0.43	0.00	0.07	0.43	0.0370	0.0000	-0.0002	0.43	0.00	0.37	0.43	0.0370	0.0000	-0.0002
0.60	0.00	0.07	0.60	0.0623	0.0000	-0.0002	0.60	0.00	0.37	0.60	0.0624	0.0000	-0.0002
0.66	0.00	0.07	0.66	0.0850	0.0000	-0.0001	0.66	0.00	0.37	0.66	0.0851	0.0000	-0.0002
0.76	0.00	0.07	0.76	0.1099	0.0000	0.0000	0.76	0.00	0.37	0.76	0.1102	0.0000	-0.0001
0.88	0.00	0.07	0.88	0.1397	0.0000	0.0001	0.88	0.00	0.37	0.88	0.1401	0.0000	0.0000
0.94	0.00	0.07	0.94	0.1683	0.0000	0.0002	0.94	0.00	0.37	0.94	0.1688	0.0000	0.0002
1.04	0.00	0.07	1.04	0.2005	0.0000	0.0004	1.04	0.00	0.37	1.04	0.2011	0.0000	0.0004
1.13	0.00	0.07	1.13	0.2393	0.0000	0.0007	1.13	0.00	0.37	1.13	0.2401	0.0000	0.0006
1.24	0.00	0.07	1.24	0.2841	0.0000	0.0011	1.24	0.00	0.37	1.24	0.2851	0.0000	0.0010
1.35	0.00	0.07	1.35	0.3346	0.0000	0.0015	1.35	0.00	0.37	1.35	0.3358	0.0000	0.0014
1.45	0.00	0.07	1.45	0.3854	0.0000	0.0020	1.45	0.00	0.37	1.45	0.3868	0.0000	0.0018
1.54	0.00	0.07	1.54	0.4306	0.0000	0.0024	1.54	0.00	0.37	1.54	0.4322	0.0000	0.0022
1.60	0.00	0.07	1.60	0.4683	0.0000	0.0027	1.60	0.00	0.37	1.60	0.4701	0.0000	0.0026
1.65	0.00	0.07	1.65	0.5071	0.0000	0.0032	1.65	0.00	0.37	1.65	0.5090	0.0000	0.0030
1.74	0.00	0.07	1.74	0.5559	0.0000	0.0038	1.74	0.00	0.37	1.74	0.5580	0.0000	0.0036
1.83	0.00	0.07	1.83	0.6124	0.0000	0.0045	1.83	0.00	0.37	1.83	0.6148	0.0000	0.0043
1.92	0.00	0.07	1.92	0.6710	0.0000	0.0052	1.92	0.00	0.37	1.92	0.6736	0.0000	0.0050
1.99	0.00	0.07	1.99	0.7313	0.0000	0.0061	1.99	0.00	0.37	1.99	0.7342	0.0000	0.0058
2.09	0.00	0.07	2.09	0.7922	0.0000	0.0069	2.09	0.00	0.37	2.09	0.7954	0.0000	0.0066
2.15	0.00	0.07	2.15	0.8465	0.0000	0.0076	2.15	0.00	0.37	2.15	0.8498	0.0000	0.0073
2.21	0.00	0.07	2.21	0.9019	0.0000	0.0085	2.21	0.00	0.37	2.21	0.9055	0.0000	0.0082
2.30	0.00	0.07	2.30	0.9761	0.0000	0.0099	2.30	0.00	0.37	2.30	0.9800	0.0000	0.0096
2.42	0.00	0.07	2.42	1.0693	0.0000	0.0115	2.42	0.00	0.37	2.42	1.0736	0.0000	0.0112
2.53	0.00	0.07	2.53	1.1742	0.0000	0.0134	2.53	0.00	0.37	2.53	1.1789	0.0000	0.0131
2.65	0.00	0.07	2.65	1.2748	0.0000	0.0151	2.65	0.00	0.37	2.65	1.2800	0.0001	0.0147
2.72	0.00	0.07	2.72	1.3499	0.0000	0.0162	2.72	0.00	0.37	2.72	1.3555	0.0001	0.0157
2.77	0.00	0.07	2.77	1.4094	0.0000	0.0173	2.77	0.00	0.37	2.77	1.4152	0.0001	0.0169
2.84	0.00	0.07	2.84	1.4865	0.0001	0.0192	2.84	0.00	0.37	2.84	1.4926	0.0001	0.0187
2.96	0.00	0.07	2.96	1.5860	0.0001	0.0213	2.96	0.00	0.37	2.96	1.5925	0.0001	0.0208
3.03	0.00	0.07	3.03	1.6783	0.0001	0.0230	3.03	0.00	0.37	3.03	1.6853	0.0001	0.0225
3.10	0.00	0.07	3.10	1.7586	0.0001	0.0247	3.10	0.00	0.37	3.10	1.7659	0.0001	0.0242
3.17	0.00	0.07	3.17	1.8386	0.0001	0.0265	3.17	0.00	0.37	3.17	1.8463	0.0001	0.0259
3.24	0.00	0.07	3.24	1.9212	0.0001	0.0285	3.24	0.00	0.37	3.24	1.9293	0.0001	0.0278
3.32	0.00	0.07	3.32	2.0098	0.0001	0.0306	3.32	0.00	0.37	3.32	2.0183	0.0001	0.0299
3.39	0.00	0.07	3.39	2.0963	0.0001	0.0325	3.39	0.00	0.37	3.39	2.1051	0.0001	0.0319
3.45	0.00	0.07	3.45	2.1853	0.0001	0.0349	3.45	0.00	0.37	3.45	2.1946	0.0001	0.0342
3.54	0.00	0.07	3.54	2.2893	0.0001	0.0377	3.54	0.00	0.37	3.54	2.2990	0.0002	0.0370
3.62	0.00	0.07	3.62	2.4018	0.0001	0.0406	3.62	0.00	0.37	3.62	2.4121	0.0002	0.0399
3.72	0.00	0.07	3.72	2.5266	0.0001	0.0442	3.72	0.00	0.37	3.72	2.5374	0.0002	0.0435
3.82	0.00	0.07	3.82	2.6712	0.0002	0.0483	3.82	0.00	0.37	3.82	2.6826	0.0002	0.0477
3.94	0.00	0.07	3.94	2.8165	0.0002	0.0521	3.94	0.00	0.37	3.94	2.8286	0.0002	0.0515
4.02	0.00	0.07	4.02	2.9377	0.0002	0.0550	4.02	0.00	0.37	4.02	2.9504	0.0002	0.0545
4.08	0.00	0.07	4.08	3.0439	0.0002	0.0581	4.08	0.00	0.37	4.08	3.0570	0.0002	0.0577
4.16	0.00	0.07	4.16	3.1644	0.0002	0.0619	4.16	0.00	0.37	4.16	3.1780	0.0003	0.0617
4.26	0.00	0.07	4.26	3.3043	0.0002	0.0661	4.26	0.00	0.37	4.26	3.3184	0.0003	0.0661
4.35	0.00	0.07	4.35	3.4402	0.0002	0.0697	4.35	0.00	0.37	4.35	3.4548	0.0003	0.0700
4.42	0.00	0.07	4.42	3.5532	0.0002	0.0726	4.42	0.00	0.37	4.42	3.5680	0.0003	0.0730
4.48	0.00	0.07	4.48	3.6547	0.0002	0.0755	4.48	0.00	0.37	4.48	3.6697	0.0003	0.0762
4.55	0.00	0.07	4.55	3.7618	0.0003	0.0787	4.55	0.00	0.37	4.55	3.7768	0.0003	0.0796
4.62	0.00	0.07	4.62	3.8831	0.0003	0.0823	4.62	0.00	0.37	4.62	3.8981	0.0004	0.0835
4.71	0.00	0.07	4.71	4.0259	0.0003	0.0863	4.71	0.00	0.37	4.71	4.0406	0.0004	0.0880
4.80	0.00	0.07	4.80	4.1845	0.0003	0.0905	4.80	0.00	0.37	4.80	4.1985	0.0004	0.0923
4.90	0.00	0.07	4.90	4.3348	0.0003	0.0938	4.90	0.00	0.37	4.90	4.3477	0.0004	0.0956
4.96	0.00	0.07	4.96	4.4617	0.0003	0.0964	4.96	0.00	0.37	4.96	4.4733	0.0004	0.0981
5.03	0.00	0.07	5.03	4.5808	0.0003	0.0992	5.03	0.00	0.37	5.03	4.5912	0.0004	0.1004
5.09	0.00	0.07	5.09	4.7102	0.0003	0.1022	5.09	0.00	0.37	5.09	4.7191	0.0004	0.1026
5.18	0.00	0.07	5.18	**4.8509**	0.0003	0.1055	**5.18**	0.00	0.37	5.18	**4.8586**	0.0004	0.1047

B_{pt} is the pole tip field, the field at r_{pt}. Since the value of the field depends upon r, it is possible to describe the energy affecting an atom in the state $|i\rangle$ and with a magnetic momentum of $\mu_{|i\rangle}$ as follows[Bra95]:

$$\mathrm{F}_i = -grad_r U_i = -\frac{\partial U_i}{\partial r}\mathrm{e}_r = -\frac{\partial U_i}{\partial B}\cdot\frac{\partial B}{\partial r}\mathrm{e}_r = -\mu_{|i\rangle}\left(B\right)\frac{\partial B}{\partial r}\mathrm{e}_r \tag{5.3}$$

U is the potential in which an atom finds itself as a result of its magnetic momentum under the influence of a magnetic field. e_r is the unit vector.

According to the theory about hyperfine structure splitting in a magnetic field, the effective magnetic momentum $\mu_{|i\rangle}$ of hydrogen depends on the value of the external field:

$$\begin{array}{ll} \mu_{|1\rangle,|3\rangle} = \pm\frac{g_s\mu_B}{2} & \approx \pm\mu_B \\ \mu_{|2\rangle,|4\rangle} = \pm\frac{g_s\mu_B}{2}\cdot\frac{x}{\sqrt{1+x^2}} & \approx \pm\frac{\mu_B B}{\sqrt{B_C^2+B^2}} \end{array} \tag{5.4}$$

Where g_s is the g-factor of the electron and μ_B is the Bohr magneton. $B_C = 50.7mT$ is the critical field for hydrogen. and x is the ratio of the external field and the critical field. The sign is "+" for the $|1\rangle$, $|2\rangle$ states and "−" for the rest two states .

5.9.2 Methods to Describe the Field for Simulation

The MAFIA results are digital values. For our $x-y-z$ reference frame, they are in the forms $B_{x,y,z}(x,y,z)$. To provide the data for the simulation work, it is not a optimum way to directly use a 3-D matrix about $B(x,y,z)$. The index work will be the most time consuming task. So we decided to use fitted functions to describe the field in the r and z directions.

$B(r,z)$ and Its Differential Functions along r

For describing the $B(r,z)$ distributions, we use a series of functions along z-axis. Each function in X-Y plane passing through $z=z_i$ is fitted with $B(r,z_i)\sim r$. The data are selected with such cuts:

- $(z_i - 0.05)\,cm < z \le (z_i - 0.05)\,cm$
- $\sqrt{x^2+y^2} \le 5.0\,cm$

Once the data have been selected, we begin to fit the function $B(r,z_i)$ with average values $B_j(r_j,z_i)$ vs. r_j. The $B_j(r_j,z_i)$ are calculated with those data whose distances to the center $(0,0)$ point are around r_j. One of the fitted results is shown in figure 5.24. The reason that we use high order polynomial is that those $B(r,z_i)$ in high z regions($z > 7\,cm\ or\ z < -7\,cm$) are more complicated than that in the center region. The other reason for this is to consider the multi-pole components inside the field.

Since the function with which we perform fitting is polynomial function, it is very easy to calculate the differential coefficient from the fitted parameters:

$$\frac{\partial B(r,z_i)}{\partial r} = \sum_{2}^{12}\frac{(n-1)\,P_n}{4.9^{n-1}}r^{n-2} \tag{5.5}$$

Differential Functions of $B(r,z)$ along z

For calculating the differential functions along z, we must fit a series of functions describing $B(r_j,z)$ at different r_j. The r_j is the distance from z-axis. $B(r_j,z)$ is a polynomial function whose parameters are fitted from $B(r_j,z_i)\sim z$. The average values $B(r_j,z_i)$ are calculated from the data points whose distance to z-axis and coordinates along z-axis satisfy:

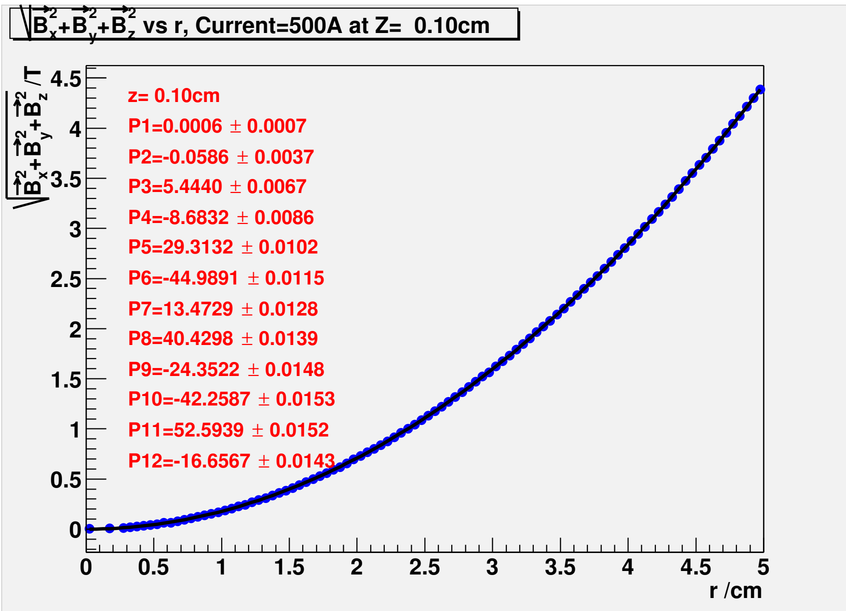

Figure 5.24: $B(r, z_i)$ changing with r, which is the distance from z-axis to the points where the magnetic field values are taken from. The current in coils equals 500A. $\mu_{steel} = 1$ is used to describe the steel layer. The fitting function is $B(r, z_i) = \sum_{n=1}^{12} P_n \left(\frac{r}{4.9}\right)^{(n-1)}$

- $(r_j - 0.05)\, cm < r < (r_j + 0.05)\, cm$
- $(z_i - 0.05)\, cm < z < (z_i + 0.05)\, cm$

One of our fitted results is presented in figure 5.25

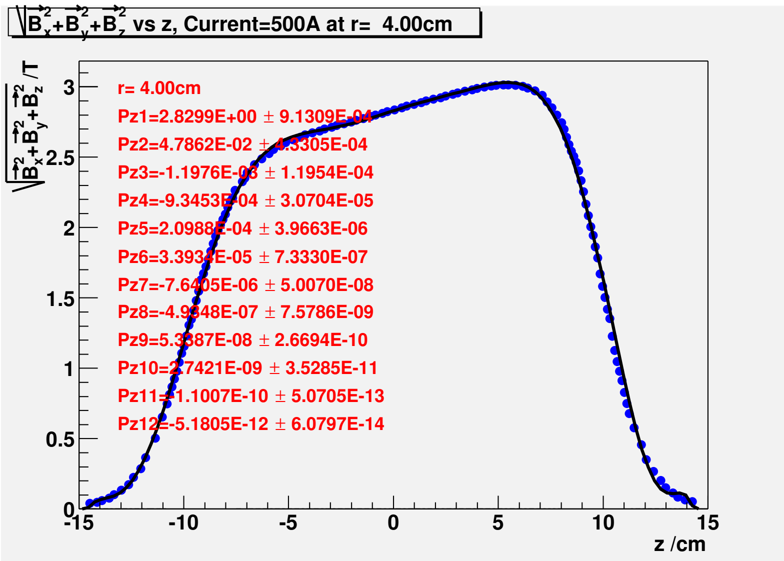

Figure 5.25: $\left|\vec{B}(r)\right|$ changing with z. The distance from z-axis to the points where the magnetic field values taken are from is in the range $3.95\,cm < r < 4.05\,cm$. The current in coils equals 500A. Using $\mu_{steel} = 1$ to describe the steel layer. The fitting function is $B_x\left(x\right) = \sum_{n=1}^{12} P_n \left(\frac{r}{4.9}\right)^{(n-1)}$

5.10 Role of the Inner Iron in Pole

Because the mechanical complication during constructing the current structure of poles with a piece of inner iron inside the steel layer. We ever had a proposal about whether we can use pure steel pole (without the inner iron in the core) instead of the current style. To answer this question, we have performed another calculation about the two modes with current equals 500A: One mode using $\mu_{steel} = 1$ describing the steel layer and with the H-B data in table 5.1 for the inner iron; The other mode using vacuum at the pole region by set the μ for both steel and iron as 1. For the yoke, we keep using H-B data listed in table 5.1. The calculated results are shown in figure 5.26.

Closely comparing the “circle” shapes inside the center regions on the top and bottom plots, we found the “circle” is not so round for the bottom one. For the ideal sextupole magnet, it should be a circle. So we get the idea about our current design is fine although it will take more energy to construct and the inner iron is necessary. About this conclusion, more confidence can be obtained after looking at the detailed plots in figure 5.27 focusing at the center zone with the distance to the center less than or equal to $4.9\,cm$.

Further analysis confirms the conclusion quantitatively. See the figure 5.28, the data for the plots are selected by a cut: the distance from data points to the center is in the range of $4.9\,cm$ to $5.0\,cm$. The plot in bottom, which represents the one without inner iron inside the poles, has two separated peaks, while the other plot in the top, for the mode with inner iron, only has one peak. At this narrow ring shape region, the smaller RMS means the more "ideal" sextupole magnet. So the inner iron cannot be omitted during constructing the second supper conducting sextupole magnet!

5.11 Nozzle Shape Optimization with the Sextupole Magnets

Due to the advantage that the magnetic field can be adjusted by changing the current through the supper conducting magnets, lots of work can be done to obtain the optimization of the nozzle shape cooperating with the new magnets for the best performance of atomic beam source.

The physical characters such as the pressure, velocity, density and temperature distribution of gas jetted out the nozzle can be simulated by a commercial software named ANSYS, which is a general purpose finite element modelling package for numerically solving a wide variety of mechanical problems. These problems include: static or dynamic structural analysis (both linear and non-linear), heat transfer and fluid problems, as well as acoustic and electromagnetic problems. I have ever with it simulated the physical characters of gas (with air instead of hydrogen atoms) at the region of the nozzle of the ABS in HERMES. The results are shown in figures 5.29 $\sim$ 5.31.

Those results can tell us where the recombination will happen heavily due to the high density; What kind of initial gas velocity distribution we should use when we simulate the atoms passing through sextupole magnets; Whether the current nozzle can cool down the gas completely when they pass through the nozzle.

If we transform current nozzle shape of the ABS in HERMES, as shown in the top plot of figure 5.32, to a new shape like that of bottom plot shown in the figure, the recombination should be decreased due to the inside surface area contacting with the atoms is less than that of the old shape. If the thickness of the vertical part increase, the time for atoms passing through the nozzle should be increased and the gas can be cooled down more completely than the current shape but the recombination will increase in proportion to the thickness of the vertical part. Those conclusions have to be justified with experiments to obtain the most optimized nozzle shape working with the new supper conducting sextupole magnets.

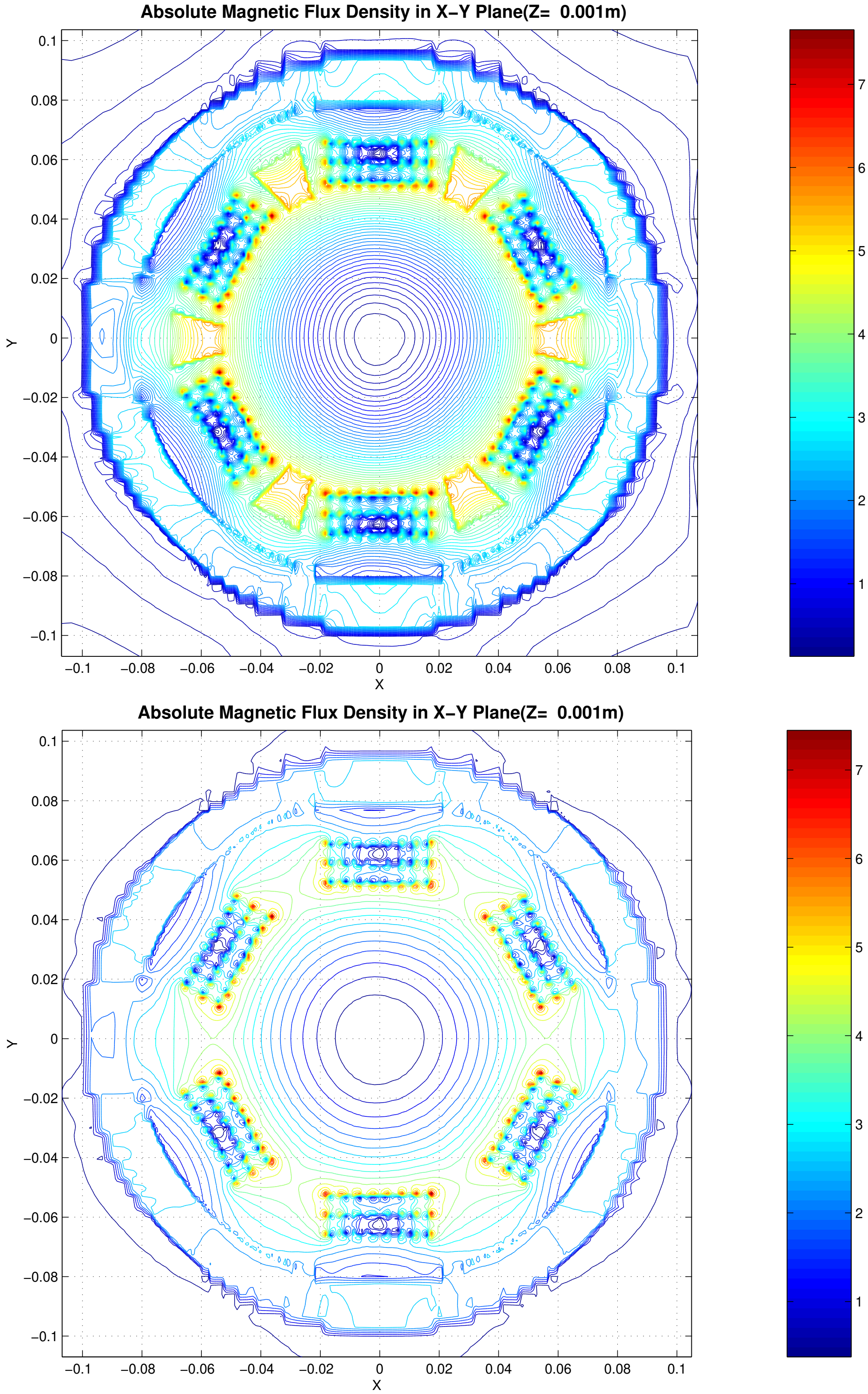

Figure 5.26: The distribution of absolute magnetic flux density $\left|\vec{B}\right|$ in X-Y plane where $z = 0.1\,cm$. $\left|\vec{B}\right| = \sqrt{\vec{B}_x^2 + \vec{B}_y^2 + \vec{B}_z^2}$. Using $\mu_{steel} = 1$ to describe the steel layer. The current in coils is 500A. The plot in top with the $H - B$ curve is for the inner iron inside poles while the one in bottom with $\mu_{iron} = 1$ as material character for the iron. ($I = 500$ A; x-, y-axis: m; B: T)

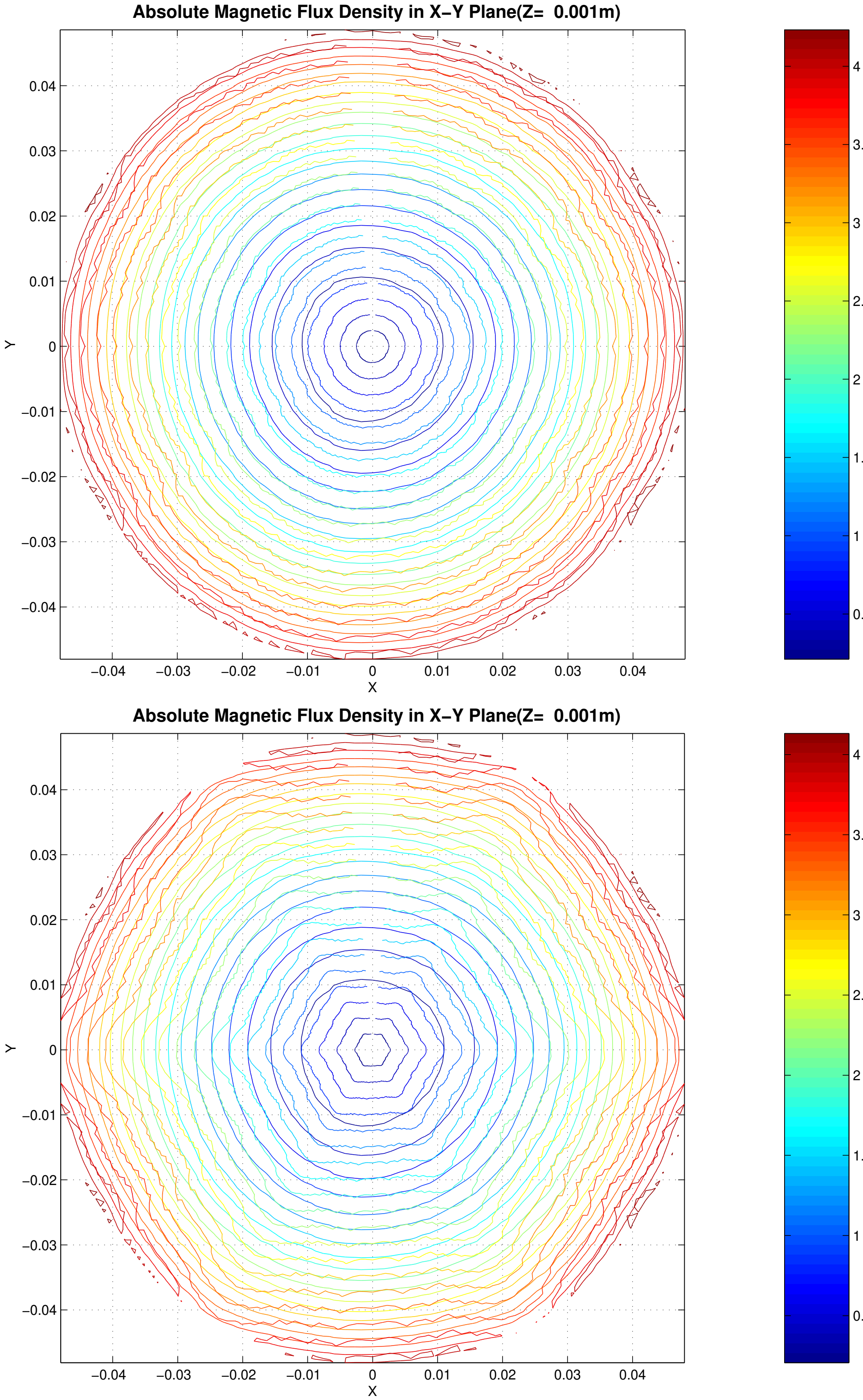

Figure 5.27: The distribution of absolute magnetic flux density $\left|\vec{B}\right|$ in X-Y plane at the center zone where $z = 0.1\,cm$ and $r \leq 4.9\,cm$. $\left|\vec{B}\right| = \sqrt{\vec{B}_x^2 + \vec{B}_y^2 + \vec{B}_z^2}$. Using $\mu_{steel} = 1$ to describe the steel layer. The current in coils is 500A. The plot in top with the $H - B$ curve is for the inner iron inside pole while the one in bottom with $\mu_{iron} = 1$ for the iron. ($I = 500$ A; x-, y-axis: m; B: T)

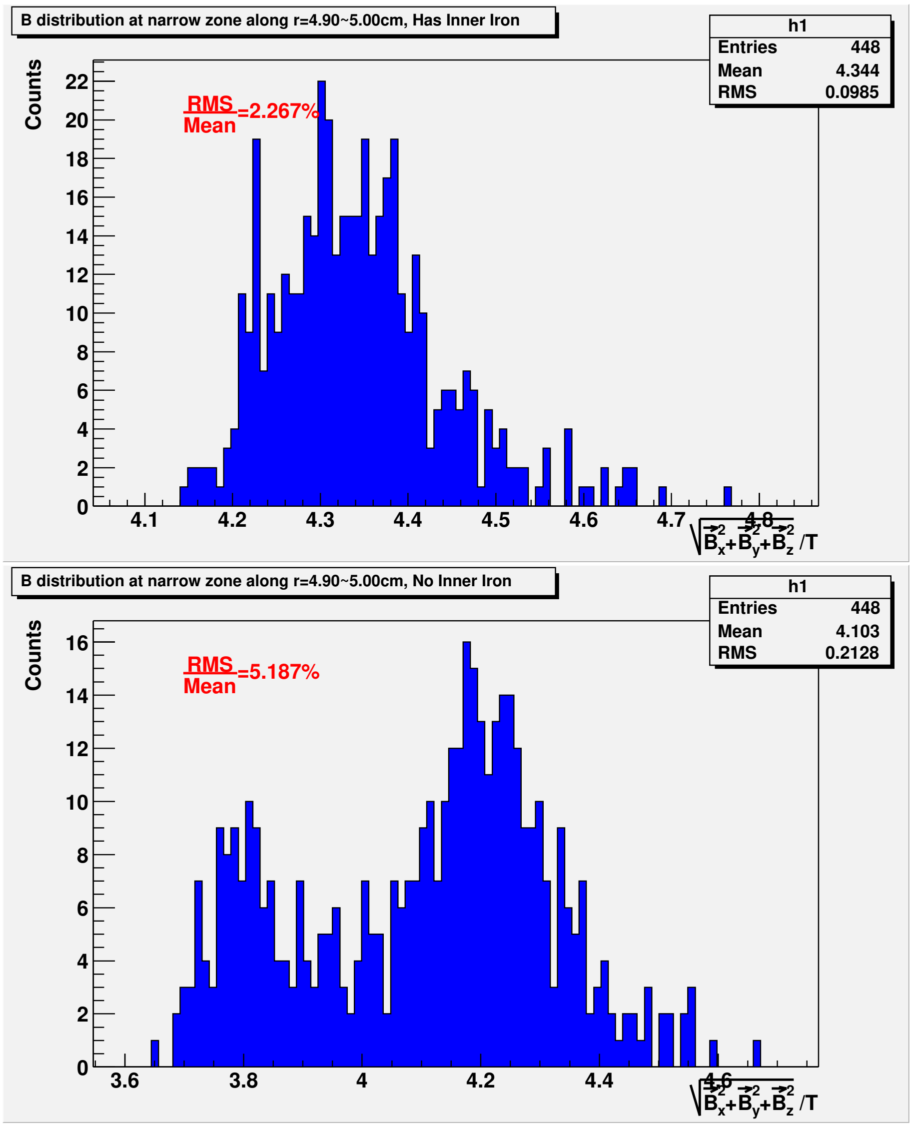

Figure 5.28: The Histogram of B distributed in the ring region with the distance to the center from 4.9 cm to 5.0 cm. The current is 500A for both plots. The top plot is for the mode with iron in the poles using H-B curve to describe the property while the bottom one without inner iron. ($I = 500$ A)

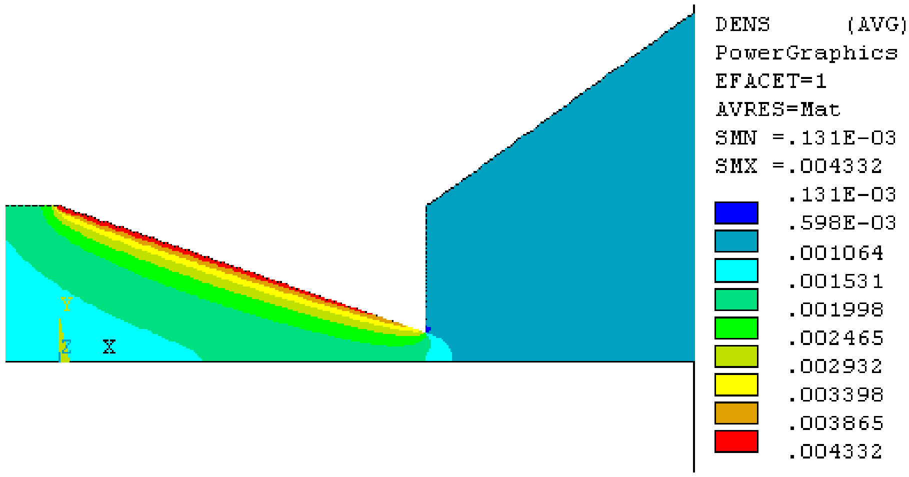

Figure 5.29: ANSYS results about the density distribution inside a nozzle with the same size as that in ABS of HERMES. The gas used here is air injected from left and jetting out in right side of the nozzle. The temperature of the wall is $100\,K$ except for the nozzle temperature of $100\,K$. The physical characters of the injecting air are, temperature $300\,K$, pressure $100\,Pa$, flux $80\,cm^3/s$.

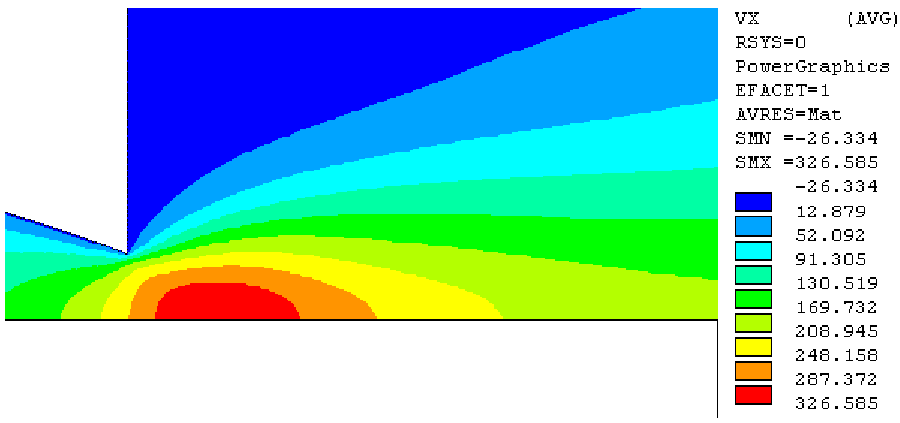

Figure 5.30: ANSYS results about average velocity distribution in the axis direction (from left to right in horizontal) of the air jetting out of the nozzle. Initial values for the gas and temperature of the wall are the same as that described in the label of figure 5.29.

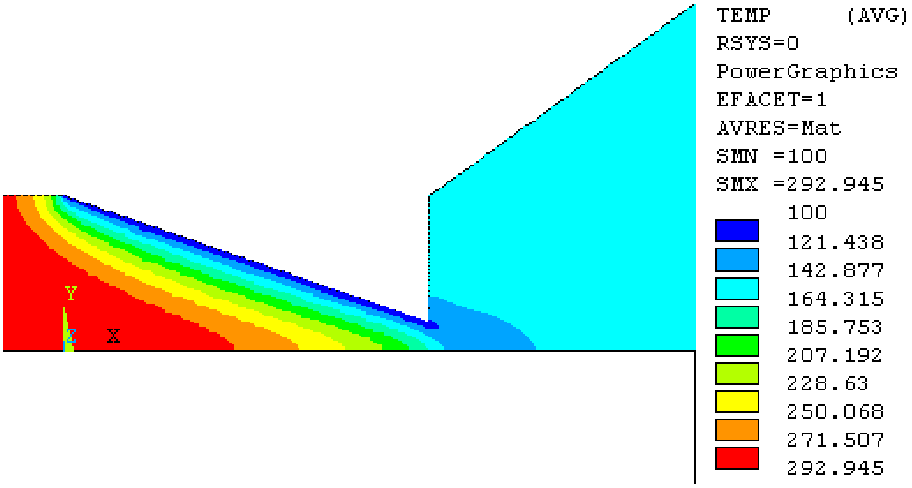

Figure 5.31: ANSYS results about the temperature distribution of air jetting out the nozzle. Initial values for the gas and temperature of wall are the same as that described in the label of figure 5.29.

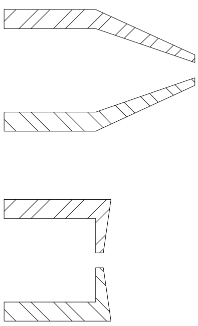

Figure 5.32: Schematic plots about nozzle shapes. Top plot: Current shape of ABS in HERMES; Bottom: A new proposed nozzle shape.

Summary

The polarized gas target system is an essential part in the HERMES experiment aimed at solving the "nucleon spin crisis".

During working on this thesis, my contributions to the HERMES experiment are the following:

The holding magnetic field of the transverse target decreasing with time was noticed. This instability of the field will cause σ transition whose amplitudes is around $2\% \sim 3\%$ for the normal e^+ beam intensity. To reduce the beam induce depolarization, an automatically control system is constructed to to improve the stability of the holding magnetic field at least 100 times. Thanks to the strength of the holding magnetic field can be accurately fixed at any value as we want, by scanning the strength of the field and measuring the polarization degree with the BRP, we can get the σ transition spectrum, which is the first experimental spectrum and can provide the optimization value of the holding field strength for the highest polarization degree. Besides the stabilization system, a pair of correction coils are installed near the storage cell of the target for the better uniformity of the holding field and the calculated result with MAFIA about the current that should be added is given in this thesis.

For the κ calibration, two methods for measuring $G(T)$ function, which describes the influence on the conductance of the tubes connected to the target cell from temperature, are proposed and tested. One of the methods is using ABS to inject gas into target cell and the other using UGFS while the temperature scan is performing. The experimental data shown this $G(T)$ correction is necessary and the experimental methods is valid. For other calibrations besides the κ, the calibration codes have been moved from PAW platform into ROOT platform for easier operation and maintenance.

For the design work of the future ABS using supper conducting sextupole magnets in HERMES group of Ferrara, more reliable results about the magnetic field flux density have been calculated with MAFIA comparing with the results calculated with TOSCA in Italy. For searching an optimized nozzle shape cooperating with the sextupole magnets, the physical properties such as temperature, velocity and density distributions of gas ejected from different nozzles with different shapes have been studied with ANSYS in the thesis.

The performance of the HERMES target has been really improved after equipped with the systems for holding field stability and uniformity. It is really my great honor that can make

some contributions to the famous international experiment group–HERMES group of DESY.

Bibliography

[Abe98] K. Abe *et al.* (E143 Collaboration), *Phys. Rev.*, **D58**, 112003 (1998).

[Abs02] A. Nass *et al.*; The HERMES Polarized Atomic Beam Source, to appear in *Nucl. Instrum. and Meth. A*.

[Ack98] K. Ackerstaff ; *First Results from the HERMES Experiment Using Unpolarized Targets*, Internal Report, HESY HERMES-96-01, May 1996

[Ade99] B. Adeva *et al.*; (SMC Collaboration), Phys. Rev. **D60**, 072004 (1999).

[Ala00] R. Alarcon *et al.*; *Nucl. Phys. A*, **663 (2000)**, 1111.

[Alg76] M. J. Alguard *et al.*, *Phys. Rev. Lett.* **37**. 1261 (1976).

[Alg78] M. J. Alguard *et al.*, *Phys. Rev. Lett.* **41**. 70 (1978).

[And01] A. Andreev *et al.*, *Nulc, Inst. and Meth.* A 465 (2001) 482

[Ant99] P. L. Antony *et al.* E155 Collaboration, *Phys. Lett.* **B463**, 339 (1999).

[Asc00] E. Aschenauer *et al.*, *Nulc, Inst. and Meth.* A 440(2000) 338

[Ash88] J. Ashman *et al.*; *Phys. Lett.*, **206**, 364 (1988)

[Ash89] J. Ashman *et al.*; *Nucl. Phys.*, **B328**, 1(1989)

[Ava96] H. Avakian *et al.*, *Nulc, Inst. and Meth.* A 378 (1996) 155

[Ava98] H. Avakian *et al.*, *Nulc, Inst. and Meth.* A 417 (1998) 69

[Bar01] S. Barsov *et al.*; *Nucl. Instrum. and Meth. A*, **462 (2001)**, 364.

[Bar92] M.Bartsch *et al.*; Solutions of Maxwell's Equations, Computer Physics Communications 72, 1992

[Bau96] C.Baumgarten;Diplomarbeit,Hamburg 1996

[Bau00] C. Baumgarten; Ph.D. Thesis, Ludwig-Maximilians Universitaet Muenchen, May 2000.

[Bau02d] C. Baumgarten *et al.*; *Nucl. Instrum. and Meth. A*, **496 (2002)**, 263.

[Ben94] T. Benisch; Diploma Thesis, Friedrich-Alexander-Universitaet Erlangen-Nuernberg, 1994.

[Ben98] T. Benisch; Ph.D. Thesis, Friedrich-Alexander-Universitaet Erlangen-Nuernberg, 1998.

[Bjo66] J.D. Bjorken, Phys. Rev. 148 (1966) 1467

[Blo99] J. Blouw, *et al.*, it Nucl. Inst. and Meth. A434(1999) 227

[Bra01] J. T. Brack *et al.*, *Nulc, Inst. and Meth.* A 469 (2001) 47

[Bra95] B. Braun; Ph.D. Thesis, Ludwig-Maximilians Universitaet Muenchen, 1995.

[Bro 79] I.N. Brnstein, K.A. Semendhajew: Moscow 1979.

[Bau02b] C. Baumgarten *et al.*; *Nucl. Instrum. and Meth. A*, **482 (2002)**, 606.

[Bur76] H. Burkhardt and W.N. Cottingham, Ann. Phys. (NY) 56, 453 (1976)

[Buu00] L.D. van Buuren *et al.*; *Nucl. Phys. A*, **663 (2000)**, 1049.

[Cam86] J.C. Camparo; *J. Chem. Phys. 86*, **3 (1987)**, 1533.

[Cap03] M. Capiluppi *et al.*; *Sextupole room temperature field measurement*, **August 4, (2003)**

[Cer94] CAS; Fifth General Accelerator Physics Course, CERN 94-01, Geneve (1994).

[Cer41] http://www.cerncourier.com/main/article/41/9/18

[Coh77] C. Cohen-Tannoudji, B. Diu, F.Laloe; Quantum Mechanics, Wiley-Interscience Publication (1977).

[Dav02] Davide Reggiani; *Precision Polarization Measurement of the HERMES H/D Gas Target*, Università degli Studi di Ferrara, 2000-2002.

[DES02] DESY, super microscope HERA, Oct. 2002

[Dez95] W.A. Dezarn *et al.*; *Nucl. Instr. Meth. A*, **362 (1995)**, 36.

[Due90] M. Dueren; A Luminosity Monitor for the HERMES Experiment, DESY-HERMES 5/90.

[Eld47] F.R. Elder *et. al.*; *Phys. Rev.* **71**, (1947) 829.

[Ell74] J. Ellis and R.L. Jaffe, Phys. Rev. D9 (1974) 1444

[Ema37] German Standard construction steel(St 37) from the email of Yorck Holler.

[Fir96] R. B. Firestone and V. S. Shirley (Edts.); Table of Isotopes, 8th Edi., Vol. 1; Wiley-Interscience, N. Y. 1996

[Gil93] R. Gilman *et al*; *Nucl. Instr. Meth. A*, **327 (1993)**, 277.

[Giu02] G. Giullo, M. Contalbrigo, P. F. Dalpiaz, R. Fabbri, M, Stancari, M, Statera, Field Measurements of Superconducting Sextupole Magnet, Internal Report, 2002.

[Grp3] DTM-130 and DTM-141 Digital teslameters with IEEE-488 GPIB interface, user's manual, Klaus schaefer gesellschaft für verfahrenstechnik mah, september 1992, p.1.

[Hae80] W. Haeberli; Contribution to the Proceedings of the 5th International Symposium on Polarization Phenomena in Nuclear Physics, no. 69 in AIP Conference Proceedings, (1980), 931.

[Hal80] K. Halbach; *Nucl. Instrum. and Meth.*, **169 (1980)**, 1.

[HER02] HERMES Collaboration; New Precision Results on teh Spin Structure Function g_1^d, ACTA Physica Polonica B, No 11, Vol. 33(2002). Presented at International Workshop on Deep Inelastic Scattering (DIS2002) Cracow, Poland, 30 April-4 May, 2002

[HER99] HERMES, Phys.Lett. B464 (1999) 123

[HmsWb] http://www-hermes.desy.de/index.html

[Hoo89] P. Hoodbhoy, R.L. Jaffe and A. Manohar, Nucl. Phys. B312 (1989) 571.

[Jaf89a] R.L. Jaffe and A. Manohar, Nucl. Phys. B321 (1989) 343

[Jaf89b] R.L. Jaffe and Aneesh Manohar, Nucl. Lett., B223 (1989) 218

[Koc99] N. Koch, E. Steffens, Rev. Sci. Instr. 70(3) (1999) 1631

[Kod79] J. Kodaira et al, Nucl. Phys. B159 (1979) 99

[Kod80] J. Kodaira et al, Nucl. Phys. B165 (1980) 129

[Kol98] H. Kolster; Ph.D. Thesis, Ludwig-Maximilians Universitaet Muenchen, February 1998.

[Kor90] W. Korsch, Proc. High Energy Spin Physics, Bonn 1990 (1990) 168

[Kut83] J. Kuti and V.W. Hughes; Ann. Rev. of Nucl. and Part. Science 33 (1983) 611

[MAF00] CST, MAFIA manual, version 4.024, 2000

[MAF3x] The MAFIA Collaboration; User Guide MAFIA, Version 3.x., CST GmbH, Lauteschlaegerstr. 38, D64289 Darmstadt

[Mar02] Michaela Marx., A simulation with MAFIA for the HERMES Transverse Target Magnet, reprot, 2002

[Mec03] Michelle Stancari, given through email, Feb. 8, 2003

[Mes61] A. Messiah; Quantum Mechanics volume II, North-Holland Publishing Company, Amsterdam, 1961.

[PAWSite] http://wwwasd.web.cern.ch/wwwasd/paw/

[PRD02] Physical Review D, particles and fields, July 2002. or http://pdg.lbl.gov/2002/consrpp.pdf

[Rea95] Annibale Reali. Realizzazione di un magnete sextupolare superconduttore da inserirsi nel sistema ottico di un bersaglio di portoni polarizzati ad alta intensità. Master's thesis, University of Ferrara, Italy, 1994-1995

[Rit01] K. Rith; Spin Asymmetries in Deep-Inelastic Electron-Nucleon Scattering - Selected HERMES Results, *Physikalisches Institut, Universität Erlangen-Nürnberg, Germany, FAU-PI2-03/01*

[ROOTSite] http://root.cern.ch/

[Sha87] M. B. Shah, D.S. Elliott and H.B. Gilbody, J. Phys. B 20 (1987), 3501.

[Shu82] E. V. Shuriak and A. F. Vainshtein, Nucl. Phys. B201 (1982) 142

[Sok64] A.A. Sokolov and I.M. Ternov; *Sov. Phys.*, Doklady **8 (1964)**, 1203.

[Ste94] M. Stephens, R. Rhodes and C. Wieman; *J. Appl. Phys. 76*, **86 (1994)**, 3479.

[Ste95] J. Stenger; Dissertation, Universität Erlangen Nürnberg 1995

[Tan82] Xiaowei TANG, *Experimental Methods in Particles Physics*, China, 1982

[Tec93] The HERMES Collabroration, *Technical design report*, July 1993

[vas00] A. Vassiliev *et al.*; *Rev. Sci. Instrum.*, Vol. 71, No. 9, September 2000

[Wan77] W. Wandzura and F. Wilczek, Phys. Lett. B172 (1977) 195

[Wei98] C. Weiskopf; Diploma Thesis, Friedrich-Alexander-Universitaet Erlangen-Nuernberg, 1998.

[Ye03] Z. Y. Ye; Diploma Thesis, University of Science and Technology of China, 2003.

[Zap96] K. Zapfe; *Nucl. Instr. Meth. A*, **368 (1996)**, 293.

Appendix A

Specification of Hardware about ABS

Table A.1: Geometrical parameters of the HERMES ABS (z - axial position relative to the nozzle exit ($z = 0$), d - inner diameter)[Abs02].

	z (mm)	d (mm)
nozzle	-13 $\rightarrow$ 0	11.0 $\rightarrow$ 2.0
skimmer	15 $\rightarrow$ 35	5.0 $\rightarrow$ 35.0
collimator	55	8.5
1st magnet	58 $\rightarrow$ 88	8.6 $\rightarrow$ 10.4
2nd magnet	108 $\rightarrow$ 163	12.0 $\rightarrow$ 16.0
3rd magnet	183 $\rightarrow$ 258	16.7 $\rightarrow$ 26.0
4th magnet	608 $\rightarrow$ 683	26.6
5th magnet	723 $\rightarrow$ 808	26.6 $\rightarrow$ 22.0
cell entrance	1159	10.0

Table A.2: The specification of HERMES ABS vacuum system. S_{nom}-nominal pumping speed; p_{op}-pressure at normal operation (dissociator throughput $1.5\, mbar \cdot l/s$)[Abs02].

Stage	Pumps	S_{nom}(l/s)	p_{op} (mbar)
I	2×turbo	2×2200	$1.2 \cdot 10^{-4}$
II	2×turbo	2×1000	$2.0 \cdot 10^{-5}$
III	1×turbo	2200	$1.8 \cdot 10^{-6}$
	+ 1×cryo	3500	
IV	1×turbo	360	$1.5 \cdot 10^{-7}$
	+ 2×cryo	2×1500	

Appendix B

Physical Constants

Table B.1: The list of constants for used in simulation work[PRD02].

Quantity	Symbols	Value
speed of light in vacuum	c	$299792458 ms^{-1}$
plank constant	h	$6.62606876(52) \times 10^{-34} Js$
plank constant, reduced	$\hbar \equiv h/2\pi$	$1.054571596(82) \times 10^{-34} Js$
electron charge magnitude	e	$1.602176462(63) \times 10^{-19} C$
conversion constant	$\hbar c$	$197.3269602(77) MeV fm$
electron mess	m_e	$9.10938188(72) \times 10^{-34} Kg$
		$= 0.510998902(21) MeV/c^2$
proton mass	m_p	$1.67262158(13) \times 10^{-27} Kg$
		$= 938.271998(38) MeV/c^2$
		$= 1.00727646688(13) u$
		$= 1836.1526675(39) m_e$
deuteron mass	m_d	$1875.612762(75) MeV/c^2$
atomic mass unit	u	$1.66053873(13) \times 10^{-27} Kg$
		$= 931.494013(37) MeV/c^2$
permittivity of free space	$\varepsilon_0 = 1/\mu_0 c^2$	$8.854187817 \cdots \times 10^{-12} Fm^{-1}$
permeability of free space	μ_0	$4\pi \times 10^{-7} NA^{-2}$
		$12.566370614 \cdots \times 10^{-7} NA^{-2}$
fine structure constant	$\alpha = e^2/4\pi\varepsilon_0 \hbar c$	$1/137.03599976(50)$
Bohr magneton	$\mu_B = e\hbar/2m_e$	$5.788381749(43) \times 10^{-5} eVT^{-1}$
nuclear magneton	$\mu_N = e\hbar/2m_p$	$3.152451238(24) \times 10^{-8} eVT^{-1}$
Boltzmann constant	k	$1.3806503(24) \times 10^{-23} JK^{-1}$
		$8.617342(15) \times 10^{5} eVK^{-1}$
Avogadro constant	N_A	$6.02214199(47) \times 10^{23} mol^{-1}$
magnetic moment of electron	$\frac{1}{2} g_s \mu_B$	$1.001159652187(4) \mu_B$
magnetic moment of proton	$\frac{1}{2} g_p \mu_N$	$2.792847337(29) \mu_N$
gyro-magnetic factor of deuteron	g_d	0.857438230(24)[Fir96]

Acknowledgements

I could not have completed this thesis without the help of many people.

First of all, please let me say a sentence to my mother: “I understand why and how hard for you to keep the secret from me that your leg has been broken during my staying in Hamburg for this thesis.”

Gratefully acknowledge my three advisors: Prof. Shuhua ZHOU, Prof. Yunxiu YE and Dr. Paolo Lenisa. They have tried their best to provide me the opportunity deploying the interesting work. I have been greatly benefited from them in the past years. I know I owned them too much! I hope I have chance to return one tenth in the future .

Thanks to Prof. Yaojun MAO and Prof. Boqiang MA for recommending me to HERMES. Thanks to Zhenyu YE, Haijiang LU and Tao CHEN for their help in DESY.

Thanks to my previous advisors during my graduate studying: Prof. Ze LI and Prof. Peijia TANG. Although I have been got the diploma since 1997, they still help me at anytime when I need. I am appreciated very much!

Thank to Zhiyi LIU, Qiuying MENG, Jin ZHOU, Chengbo Li, Shaojun LU, Dr. Xiaomei LI and Prof. Jian YUAN for their enthusiastic and in time help form China.

Thank to Prof. Zixiang ZHAO, Prof. Weiping LIU, Prof. Zuying ZHOU for their support, and to Yi XIE, Xiaolan WANG, Zhanqin YU, Congmin FAN, Pu ZHANG for they help in CIAE.

In DESY, I have met many experts and friends. Many helps, suggestions and cooperations from them are the fundamental part of this thesis. They are: Dr. Dirk Ryckbosch, Dr. Elke-Caroline Aschenauer, Dr. Maurice Bouwhuis, Dr. Yorck Holler, Dr. Larry Felawka. Dr. Pasquale Di Nezza, Soerne Moeller and Sabine Krohn. Thanks to Dr. Susan Wipf, Dr. Paola Ferretti Dalpiaz, Dr.Michelle Stancari and Marco Statera for their help in magnetic field calculation work.

For our target group of HERMES, the friendship among us will be lasted in all my rest life. Phil Tait, Dr. Davide Reggiani, Marco Capiluppi, Hrachya Marukyan and I have been worked side by side for one and a half years under the leading of Paolo Lenisa. Thanks to Alexander Nass for his useful suggestions about the ABS to our target family. I have many wonderful moments. I like the best gift from HERMES to me on the Christmas of 2003: The card for “The Most Enthusiastic Shift Crew”.

Finally, I would like very formally to say thanks to my wife, Xiaorui YANG. While my staying in Germany, only she and my four years old son take care each other in China. Without her courage taking the whole responsible for my family, I have no chance to finish the thesis.

There are so many people beside those previous mentioned have directly or indirectly helped me in the past years. It is really hard for me to enumerate completely what and how they have dedicated their time and energy in the past three years to me with one or two pieces of pages. Here, I will express my deepest appreciation to them. I am very happy that I am living in such a beautiful world formed by so many warm hearted people.

THANKS!

Papers During PhD Period (2001.9-2004.8)

Published

1. 王思广，徐翠华，任天山，γ射线谱中符合相加修正系数的Monte-Carlo模拟，*原子能科学技术*, P. 297-301, 第37卷第4期, 2003年7月。
2. 王思广，柯国土，吕征，辛锋，接口软件CITA-TOOL在中国先进研究堆堆物理分析中的应用，*原子能科学技术*, P. 121-124, 第36卷第2期, 2002年3月
3. S. G. Wang, M. Bouwhuis, Y. Holler, P. Lenisa, D. Reggiani, H. Marukyan, P. Tait, Z. Y. YE, Y. X. YE, Active Stabilization of the Transverse Holding Field of the HERMES Polarized Gas Target, Internal Report: HERMES03-033
4. 徐翠华，王思广，周强等，蒙特卡罗方法调节探测器死层厚度和冷指尺寸的研究，*中国辐射卫生*，P203-204,第12卷第4期, 2003年12月。
5. LIU Zhi-yi, LI Cheng-bo, WANG Si-guang, ZHOU Jing, MENG Qiu-ying, LU Shao-jun, ZHOU Shu-hua, Measurement of Change of ^{7}Be Decay Rate in Be and Au, *Chinese Physics Letters*, Vol.20, N0.6(2003)829-831
6. 刘志毅，李成波，王思广，周静，孟秋英，卢绍军，周书华，等，^{7}Be半衰期的精确测量，*原子核物理评论*，P. 235-238, 第20卷第4期
7. 吕征，孙志勇，王思广，低浓化微堆拓展应用可行性研究，*原子能科学技术*, P. 106-110, 第37卷第2期, 2003年3月。
8. 吕征, 孙志勇, 王思广, 肖诗刚, 沈峰, 柯国土, BNCT在低浓化微堆上应用的可行性研究, *中国原子能科学研究院年报*, P.99, 2002年

To be Published

1. 王思广, M. Bouwhuis, Y. Holler, P. Lenisa, D. Reggiani, H. Marukyan, P. Tait, 叶震宇, 叶云秀, 一种稳定磁场的方法, *核技术*, 2004年4月完成修改稿
2. 李成波，刘志毅，王思广，周静，孟秋英，周书华,在Be和Au中^{7}Be半衰期差别的测量,*原子能科学技术*, 已接受.
3. Z. YE, et. al., S. WANG, (Target Group of HERMES), Direct Measurement of Intra-Beam Scattering in Atomic Beam Sources, Submitted, 2004
4. A.Airapetian, et. al., S. WANG, (HERMES Collaboration), The HERMES Polarized Hydrogen and Deuterium Internal Gas Target, Submitted, 2004